Increasing the sensitivity to low mass dark matter in CRESST-III with a new DAQ and signal processing

Nahuel Ferreiro Iachellini

München 2018

Increasing the sensitivity to low mass dark matter in CRESST-III with a new DAQ and signal processing

Nahuel Ferreiro Iachellini

Dissertation
an der Physik
der Ludwig–Maximilians–Universität
München

vorgelegt von
Nahuel Ferreiro Iachellini
aus Buenos Aires

München, den 18.12.2018

The work presented in this thesis was carried out in the CRESST group at the
Max Planck Institut für Physik
(Werner-Heisenberg-Institut)

Erstgutachter: Prof. Dr. Otmar Biebel
Zweitgutachter: Prof. Dr. Wolfgang Dünnweber
Tag der Mündlichen Prüfung: 25.02.2019

Contents

Zusammenfassung

Das vorherrschende ΛCDM-Modell der Kosmologie sagt einen großen Beitrag nicht leuchtender, vornehmlich über Schwerkraft wechselwirkender Materie zum Gesamtenergiegehalt des Universums voraus. Diese so genannte dunkle Materie stellt Experimentalphysiker durch ihre schwer fassbare Natur seit fast einem Jahrhundert vor große Herausforderungen. Zum Zeitpukt der Veröffentlichung dieser Arbeit liegt nach wie vor kein unstrittiger experimenteller Nachweis von dunkle-Materie-Teilchen vor.

Das favorisierte Paradigma geht davon aus, dass dunkle-Materie-Teilchen ein thermisches Relikt aus einer früheren Epoche des Universums sind. Diese Teilchen, sogenannte WIMPs, sind schwach wechselwirkend, massiv und stabil. Diese WIMPs befinden sich in der dichten und heissen Anfangsphase des Universums im thermischen Gleichgewicht mit allen anderen Teilchen. Durch die Expansion des Universums reduzierten sich Energie- und WIMP-Dichte soweit, dass Produktion und Vernichtung zum Erliegen kamen und die zu diesem Zeitpunkt vorherrschende WIMP-Dichte eingefroren wurde.

Im weiteren Verlauf sind WIMPs vor allem als die dominierende gravitative Komponente für die Entwicklung des Universums relevant.

Unter der Annahme einer nur aus WIMP bestehenden Zusammensetzung der dunklen Materie werden Teilchenmassen wenigstens von $\sim$GeV/c^2 erwartet. Leichtere WIMPs würden in zu großer Menge entstehen.

Das Fehlen positiver Signale aus den verschiedenen Versuchen, dunkle-Materie-Teilchen zu detektieren, lenkte die Aufmerksamtkeit auf einer Reihe von nicht-Standard Szenarien, die nicht an den genannten Massenbereich gebunden sind.

Das CRESST-Experiment ist eine der erfolgreichsten experimentellen Bemühungen, die versuchen, dieses Mysterium der Natur zu lösen. Ziel ist es, in der Milchstraße vorhandene dunkle Materie mit einem empfindlichen Teilchenetektor direkt nachzuweisen. Eine exzellente Energieauflösung und die Möglichkeit, zwischen verschiedenen Teilchenarten zu unterscheiden, sind zwei entscheidende Punkte, die CRESST zu einem wettbewerbsfähigen Experiment im Bereich der Suche nach dunkler Materie machen.

Die zweite Stufe des Experiments erreichte eine weltweit führende Empfindlichkeit für dunkle-Materieteilchen mit einer Masse unter 1,7 GeV/c^2. Der Energieschwelle, die eng mit der Energieauflösung verbunden ist, kommt hierbei eine Schlüsselrolle zu. Die neue Stufe des Experiments, CRESST-III, wurde speziell optimiert, um diesen Parameter weiter zu verbessern und eine bisher unerreichte Empfindlichkeit gegenüber Wechselwirkungen mit

Energien $\leq$ 100eV zu erreichen.

Das erste Kapitel dieser Doktorarbeit widmet sich der Darstellung des kosmologischen Standardszenarios und der wichtigsten Beweise für das Vorhandensein dunkler Materie. Das zweite Kapitel konzentriert sich auf die wichtigsten experimentellen Techniken, die zur Identifizierung der dunklen-Materie-Teilchen eingesetzt werden. Die gesuchte Signatur bei der direkten Suche wird mit Fokus auf das CRESST Experiment diskutiert. Das dritte Kapitel konzentriert sich auf kryogene Detektoren, den CRESST-Aufbau im *Laboratori Nazionali del Gran Sasso* und die neu eingesetzten CRESST-III-Detektormodule. Das vierte Kapitel ist ganz der Optimierung des entscheidenden Parameters gewidmet: der Energieschwelle. Eine neue Datenerfassung und eine neuartige auf der *Optimum Filter*-Technik basierende Analyse werden beschrieben und mit der herkömmlichen Erfassung und Datenverarbeitung verglichen. Die Verbesserung der Empfindlichkeit und die Erweiterung der Nachweisgrenze zu geringeren Massen werden quantifiziert.

Das fünfte und letzte Kapitel führt eine neue Betriebskonfiguration für die von CRESST hergestellten Temperatursensoren ein. Ein erster *Proof Of Principle* durch einen erfolgreich betriebenen Detektor wird präsentiert. Die notwendigen weiteren Verbesserungen für eine dauerhafte Verwendung der neuen Konfiguration werden diskutiert.

Abstract

Dark matter is a fundamental brick of modern day cosmology. The great success of the ΛCDM model convinced the scientific community of the existence of a large fraction of non-luminescent matter in the Universe. Its elusive nature is challenging experimental physicists since almost a century and, at the time of this thesis work, no uncontroversial signal is measured.

The most favoured paradigm assumes dark matter particles being a thermal relic of an earlier epoch of the Universe. These particles, the WIMPs, are weakly interacting, very massive and stable. Their creation and annihilation, at the time of a hot and dense Universe, was analogous to all other particles. The expansion of the Universe reduced their density to the point that the annihilation ceased to occur and the population of WIMPs froze out.

In the subsequent evolution of the Universe the main effect due to the WIMPs is the gravitational attraction, dominant compared to the one of all other particles.

Under the assumption of a WIMP-only dark matter composition, these particles are expected to have a mass of at least a few GeV/c^2. Lighter WIMPs would "overclose" the Universe.

The lack of a positive signals from the various attempts to study dark matter particles, opened the door to a number of non-standard scenarios that are not bound to the mentioned mass range.

The CRESST experiment is one of the most successful experimental efforts that are trying to shed light on this mystery of Nature. The goal is to detect dark matter particles present in the Milky Way by means of sensitive detectors. Great energy resolution and an event-by-event particle identification are two crucial points that make CRESST a competitive dark matter search.

The second stage of the experiment achieved an outstanding sensitivity to dark matter particles with mass below 1.7GeV/c^2 which set a new world-leading benchmark on this region of the parameter space. The energy threshold, intimately connected to the energy resolution, was the key parameter that contributed to the results. The new stage of the experiment, CRESST-III, was specifically optimised to further improve this parameter in order to achieve an unprecedented sensitivity to interaction with energies $\leq$ 100eV.

In this thesis the first chapter is dedicated to the presentation of the standard cosmological scenario and the main evidence for the existence of dark matter. The second chapter focuses on the main experimental techniques deployed to detect a fingerprint of

dark matter particles. The sought-for signature in direct searches is discussed to set the ground for the specific case of the CRESST experiment. The third chapter is centred around cryogenic detectors, the CRESST installation in the *Laboratori Nazionali del Gran Sasso* and the newly deployed CRESST-III detector modules. The fourth chapter is fully dedicated to the optimisation of the crucial parameter: the threshold. A new data-acquisition and a novel Optimum Filter-based analysis are described and compared to the conventional acquisition and data-processing. The improvement in sensitivity and the extension of the sensitivity reach at low masses are quantified.

The fifth and last chapter introduces a new operational configuration for the temperature sensors produced by CRESST. A first proof-of-principle is given, presenting a successfully operated detector. The necessary further improvements for an actual use of the new configuration are discussed.

Chapter 1

Dark Matter - A long standing puzzle

Dark matter is amongst the most intriguing puzzles of Nature that still elude modern day physics. Introduced for the first time in 1933, almost a century ago, by astronomer F. Zwicky, dark matter explained the velocity distribution of galaxies in the Coma cluster[1]. This required approximately 400 times the mass of the observed luminescent matter in order to fit the laws of kinematics.

The number of astronomical observations grew over the decades, and so did their accuracy and reliability. Ranging from the galactic scale up to the whole observable Universe, there is always a large amount of "missing matter", without which the scientific community is unable to explain the observations. Labelled as *dark* because it does not interact via electromagnetic force and therefore eludes telescopes, this type of matter plays a crucial role in the origin, evolution and current appearance of the Universe.

In our modern understanding of the Universe's composition, so-called dark energy accounts for 68.89% of the total energy density, while matter accounts for the remaining 31.11%. The latter percentage is determined mainly by the sum of the contributions of baryonic matter (4.9%) and cold dark matter (26%)[2].

This chapter will focus on the main evidence for the existence of dark matter and provide an overview of candidates coming from particle physics.

1.1 The Standard Cosmological Model

The description of the evolution of the Universe, in modern cosmology, is given in the framework of General Relativity. The starting point are **Einstein's Field Equations**, which connect the geometry of space-time to the energy distribution in space and time:

$$G_{\mu\nu} + \Lambda g_{\mu\nu} = \frac{8\pi G}{c^4} T_{\mu\nu} \tag{1.1}$$

where $G_{\mu\nu}$ is the tensor describing the curvature of space-time (Einstein tensor), Λ is a constant usually named the **cosmological constant**, $g_{\mu\nu}$ is the metric tensor, G is the Newton gravitational constant, and $T_{\mu\nu}$ is the stress-energy tensor which carries the information of flux and density of energy and momenta in space-time.

1.1.1 The expanding Universe

The observation of the redshift of spectral lines of the galaxies at various distances was made by Edwin Hubble[3] in 1929. The phenomenon is indeed a consequence of the Doppler effect. As the radiation source moves *towards* the observer, the measured wavelength appears shorter than the one measured by an observer in the reference frame of the source. Likewise, if the source moves *away* from the observer, the detected wavelength appears longer. Hubble observed that all galaxies[1] are moving away from the Milky Way, i.e. all observed radiation lines shift to longer wavelengths (redshift) and this shift depends on the relative distance to the Milky Way.

The law relating the distance d of a galaxy from the Milky Way and the galaxy velocity v is the Hubble's law:

$$v = H_0 d \tag{1.2}$$

With H_0 being the present day Hubble constant.

The idea of an expanding Universe was not new at the time. In 1927, G. Lemaître published a work based on General Relativity[4] in which he provided a first observational estimation of the Hubble constant. In his work he introduced a time-dependent scaling factor $a(t)$ to describe the expansion of the Universe:

$$v = \frac{\dot{a}(t)}{a(t)} d \tag{1.3}$$

Equation 1.3 is nothing but the Hubble's law, if we set $H(t) \equiv \frac{\dot{a}(t)}{a(t)}$. The Hubble constant H_0 is then the present day evaluation of $H(t)$, $(70.1 \pm 1.3)\text{kms}^{-1}\text{Mpc}^{-1}$[5]. The idea of an expanding Universe means that $a(t)$ is increasing over time.

1.1.2 The Friedman equation

The basic postulate that we assume now to describe the Universe is called the **cosmological principle**. It states that the Universe looks the same at any point in space. In particular, the Universe is considered homogeneous and isotropic at very large scales ($l \gg 100\text{Mpc}$). Under such assumption the generic distance between two points, in comoving coordinates (r, θ, ϕ), reads:

$$ds^2 = c^2 dt^2 - a^2(t) \left(\frac{dr^2}{1 - kr^2} + r^2 d\theta^2 + r^2 \sin^2 \theta d\phi^2 \right) \tag{1.4}$$

where $a(t)$ is the scaling factor introduced in Equation 1.3, and $\text{k} = (\pm 1, 0)$ is the curvature of the Universe. Equation 1.4 sets the metric to measure distances in space-time and is known as the **Friedman-Lemaître-Robertson-Walker metric**. From experimental

[1] There are a few exceptions related to galaxies near the Milky Way.

evidence[6], the Universe is spatially flat[2], which allows us to set $k = 0$. Equation 1.4 takes the easier form:

$$\begin{aligned} ds^2 &= c^2dt^2 - a^2(t)(dr^2 + r^2d\theta^2 + r^2\sin^2\theta d\phi^2) \\ &= c^2dt^2 - a^2(t) \underbrace{(dx^2 + dy^2 + dz^2)}_{\text{cartesian coordinates}} \end{aligned} \tag{1.5}$$

Equation 1.5, apart from the scaling factor $a(t)$ on the spacial side of the metric, looks the same as the usual Minkowsky metric. The convenient aspect of Equation 1.5 is that it is diagonal, so when it is plugged into the Einstein Field Equations 1.1, they decouple and we can solve the time component setting $\mu = \nu = 0$:

$$\left(\frac{\dot{a}(t)}{a(t)}\right)^2 = \frac{8\pi G}{3c^2}\rho + \frac{c^2\Lambda}{3} - \frac{c^2k}{a^2(t)} \tag{1.6}$$

Equation 1.6 is the notorious first **Friedman equation**. Despite its simplicity, it describes the evolution of the expansion of the Universe. In this equation, k is the curvature parameter (that we set to 0) and $\rho \equiv T_{00}$ is the energy density of the Universe. It is convenient to define a **critical density** ρ_c:

$$\rho_c = \frac{3c^2H^2(t)}{8\pi G} \tag{1.7}$$

The present day value of ρ_c is $\sim$ 5 keV/cm^3, or roughly 5 protons/m^3. Thanks to the definition of Equation 1.7 we can express any density ρ_i as a fraction of the critical density:

$$\Omega_i = \frac{\rho_i}{\rho_c} \tag{1.8}$$

The Friedman equation can be then written in the very compact form:

$$\Omega_{radiation} + \Omega_{matter} + \Omega_\Lambda - \Omega_{curvature} = 1 \tag{1.9}$$

The term $\Omega_{curvature}$ vanishes as we set $k = 0$ and it is reported in Equation 1.9 for the purpose of completeness. Ω_Λ is the contribution of the dark energy to the Universe's total energy density. Little to nothing is known about dark energy, other than it is needed to drive the expansion of the Universe against the attraction of the dominating force, Gravity. $\Omega_{radiation}$ and Ω_{matter} are the contributions to the energy density of radiation and matter. The latter can be decomposed into all the several species of massive particles contributing to the total amount of matter in the Universe (i.e. dark matter, heavy particles, neutrinos...):

$$\Omega_{matter} = \Omega_\chi + \Omega_{baryons} + \Omega_{neutrinos} + \dots \tag{1.10}$$

Ω_χ is the term due to the (as yet unknown) dark matter and, as it will be shown in the following sections, it is by far the largest contribution to the Ω_{matter} term in Equation 1.9.

[2]The claimed flatness refers to the Universe at its largest scale. Massive bodies, such as galaxies, warp the Universe locally.

1.2 Evidence for Dark Matter

This section provides an (incomplete) review of the main cosmological observations suggesting the existence of a large amount of matter, which does not take part in electromagnetic interaction and which has not (as yet) been directly observed. It is fascinating that all cosmological observations substantially agree on the magnitude of the missing matter. In Figure 1.1 the independent fits of the relevant cosmological parameters of the base ΛCDM model[3] from the latest Planck results are shown.

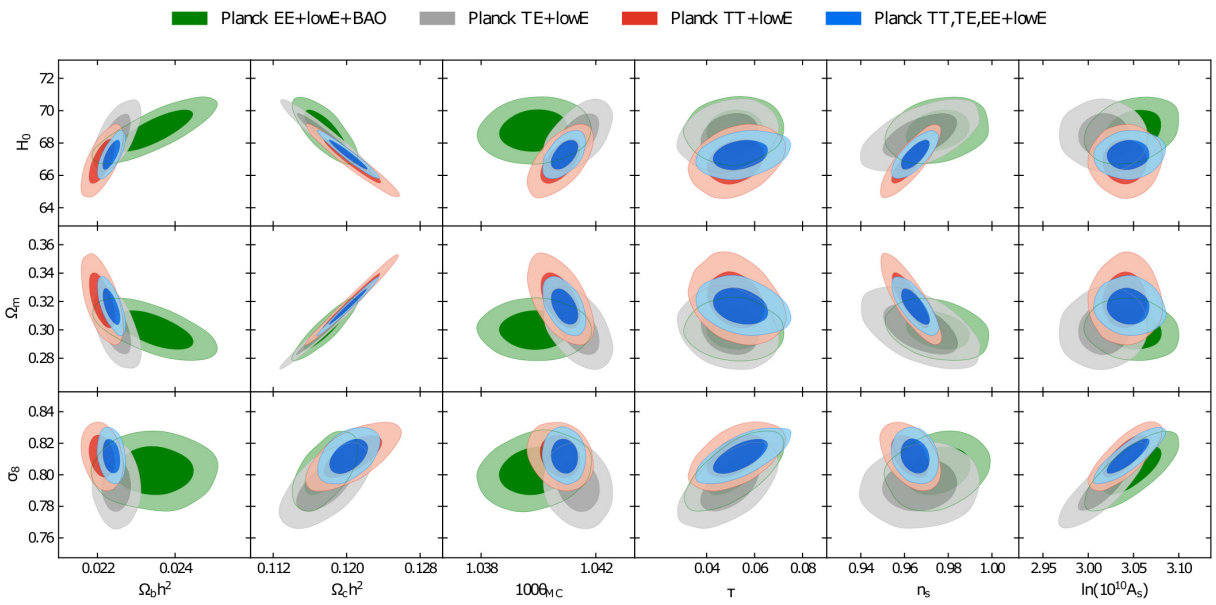

Figure 1.1: Constraints on cosmological parameters of the base ΛCDM model. Colour-coded are the 68% and 95% confidence levels for different datasets. The $\Omega_c h^2$ parameter (second column) is the one accounting for Cold Dark Matter. Plot from [2].

1.2.1 The Cosmic Microwave Background

The **CMB** (Cosmic Microwave Background) was discovered in 1964[7] and promptly interpreted as an echo of the Big Bang[8]. In the early stage of the Universe, charged matter and electromagnetic radiation were strongly coupled in a primordial plasma, so that hydrogen atom production and disintegration were in thermal equilibrium:

$$p^+ + e^- \Leftrightarrow H + \gamma \tag{1.11}$$

As the Universe (adiabatically) expanded, its temperature decreased and once it reached the value of $\approx 0.3\text{eV}/k_B$ (around 380,000 years after the Big Bang), stable neutral hydrogen

[3]The ΛCDM model is a parametrisation of the Universe described in section 1.1. It accounts for dark energy (Λ) and structure formation due to Cold Dark Matter (CDM).

could be formed. As the Universe was too cold to split up hydrogen back into protons and electrons, electromagnetic radiation (the γ in Equation 1.11) was free to travel through matter (and the Universe became transparent to photons).

The photons that escaped the last p^+/e^- recombinations are those of the Cosmic Microwave Background (CMB). For this reason, the apparent background sphere of the CMB is often called the "surface of last scattering". The CMB is the most perfect

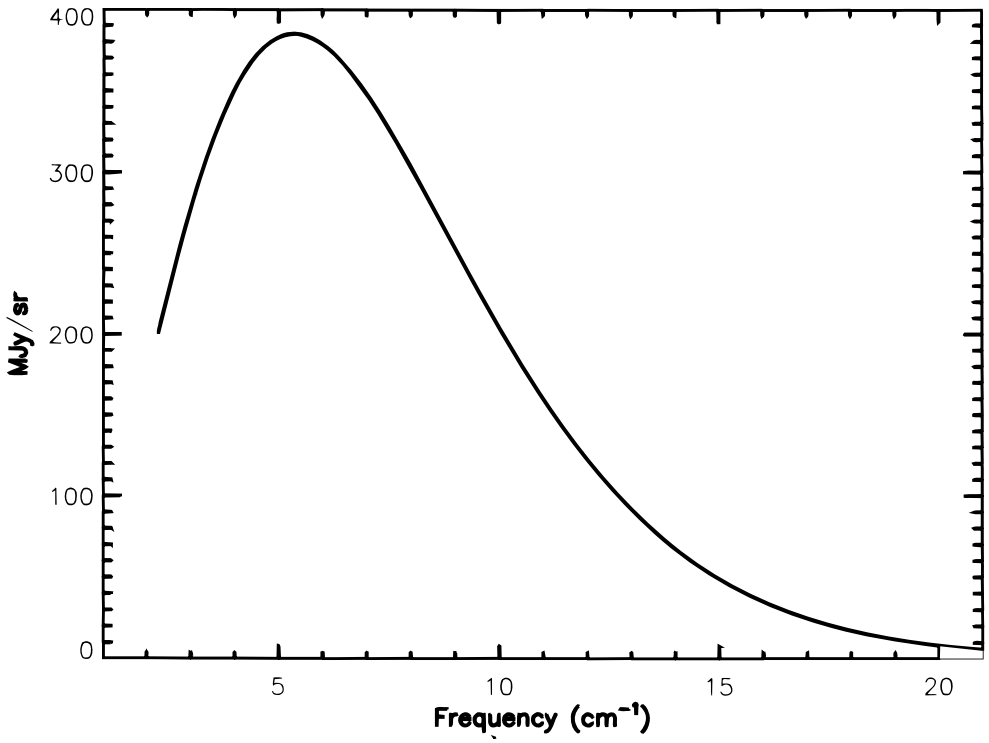

Figure 1.2: Spectrum of the CMB radiation. Error bars are just a fraction of the width of the line. The experimental data are nicely fitted to a black body spectrum with T = 2.728K. Plot from [9].

realisation of a black body that we know in Nature. Figure 1.2 shows the CMB spectrum measured by FIRAS[9], overlaid to the best fit of a black body radiation.

The most intriguing aspects of the CMB arise when looking at its distribution in the sky. While the temperature appears to be uniform down to the mK, below this magnitude anisotropies become apparent. Figure 1.3 shows a map of the CMB measured by Planck[2]. The fluctuations of the photons' energy are due to non-homogeneities of the medium as they decouple from matter. Because of this, the CMB is a powerful tool to probe the (baryonic) matter distribution at the time of the last scattering. When a photon left a region of the primordial plasma with a higher-than-average density, part of the energy was lost resulting in a redshifted photon (compared to the average photon energy). On the contrary, photons which escaped regions with a lower-than-average density appear blueshifted. This effect is known as the Sachs-Wolfe-Effect[11].

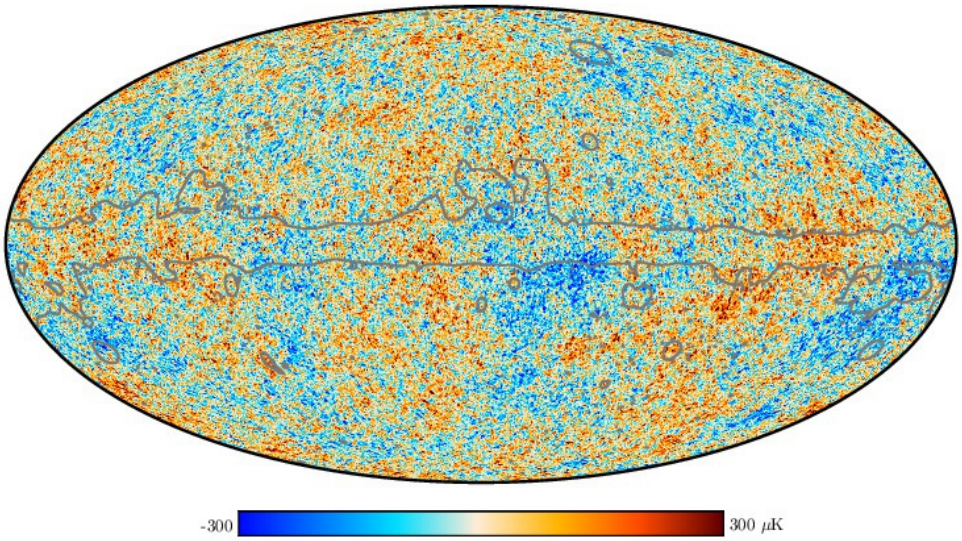

Figure 1.3: Temperature map of the CMB. The grey contour marks the region where the residuals from the foreground emission (mainly due to the galactic plane) are substantial. The color-coded temperature refers to the fluctuations around the mean value T = 2.728K. Picture from [10].

The mere presence of such anisotropies in the primordial plasma is already a strong hint for the existence of dark matter: random fluctuations in the matter density would be almost instantaneously washed out by the dominating electromagnetic force. Anisotropies can then be explained with the presence of matter not affected by the electromagnetic force, which is able to shape the baryonic matter distribution via gravitation.

The above-stated argument in its quantitative form led to extremely compelling constraints on cosmological parameters (as well as on dark matter abundance), see [12] and [13] for the results of WMAP's 5-year sky observation. Here we use the more recent results from the Planck space observatory[2]. Figure 1.4 shows the power spectrum of the Cosmic Background (Fig. 1.3) as a function of the multipole moment[4] l. The data points are fitted assuming the ΛCDM model, with three neutrino species (making the approximation that two states are massless and the third possesses the mass $m_\nu = 0.06$eV). From the (extremely good) fit of the ΛCDM model we can extract relevant cosmological parameters. In particular the age of the Universe (13.7971 Gyr), the dark energy abundance ($\Omega_\Lambda = 68.89\%$), the dark matter abundance (26%) and a constraint on the flatness of the Universe ($\Omega_{curvature} = 0.0007 \pm 0.0019$). All parameters are taken from the Planck data released in 2018[2].

[4]Since the CMB appears as a temperature distribution over a sphere, it is convenient to represent it in terms of spherical harmonics (multipole expansion) and use l as angular parameter.

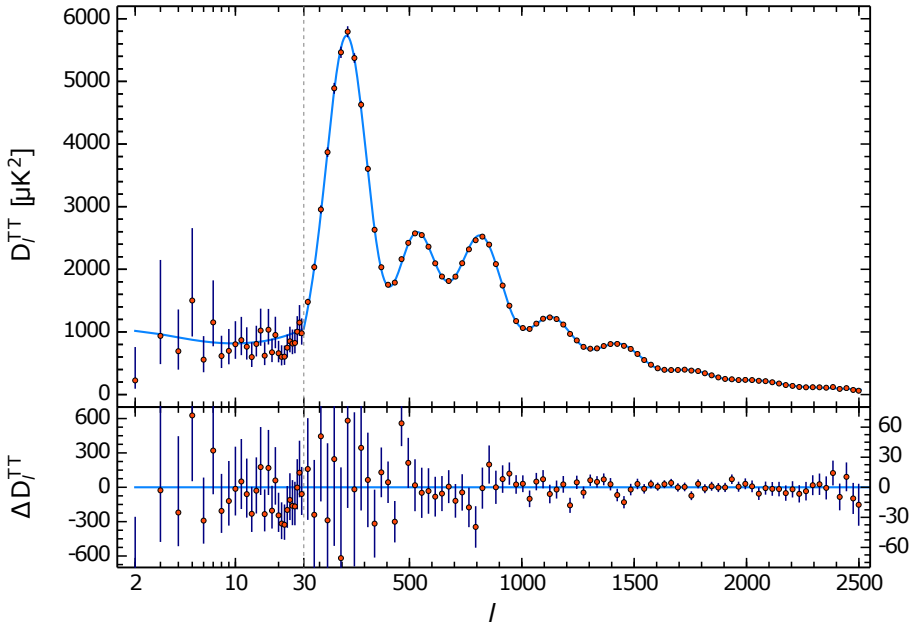

Figure 1.4: Temperature power spectrum as a function of the multipole l (angular variable). Foreground emissions were substracted from the data. Data points are frequency-averaged. The peaks of the temperature power spectrum contain most of the relevant information in the frame of the ΛCDM model. Picture from [2].

1.2.2 Big Bang Nucleosynthesis

Shortly after the Big Bang, baryons (protons and neutrons) were interacting to form deuteron, which disintegrated via photodissociation according to:

$$p + n \Leftrightarrow d + \gamma \tag{1.12}$$

The relative abundances of the four species in Equation 1.12 are determined by the thermal equilibrium (in a similar manner as Equation 1.11 does for the production and disintegration of hydrogen). As the Universe was cooling, after 4 minutes of expansion its temperature dropped below 80keV/k_B. The dissociation of deuteron stopped and the deuterons could keep fusing with the surrounding baryons forming light isotopes, up to ^{7}Li (Big Bang nucleosynthesis). Twenty-four minutes after the Big Bang the temperature was at approximately 30keV/k_B and almost all free neutrons disappeared (either they decayed or became part of light nuclei) and the Coulomb barrier could no longer be penetrated, setting in the end of the nucleosynthesis. A detailed description of standard (and non standard) scenarios can be found in [14]. ^{4}He is energetically the most favoured isotope to be created, so that almost all neutrons available end up forming it. The abundance of ^{4}He is then not really sensitive to baryon density, but instead to the n/p ratio at the beginning of the nucleosynthesis (see the red line in Fig. 1.5). Given that we expect 7

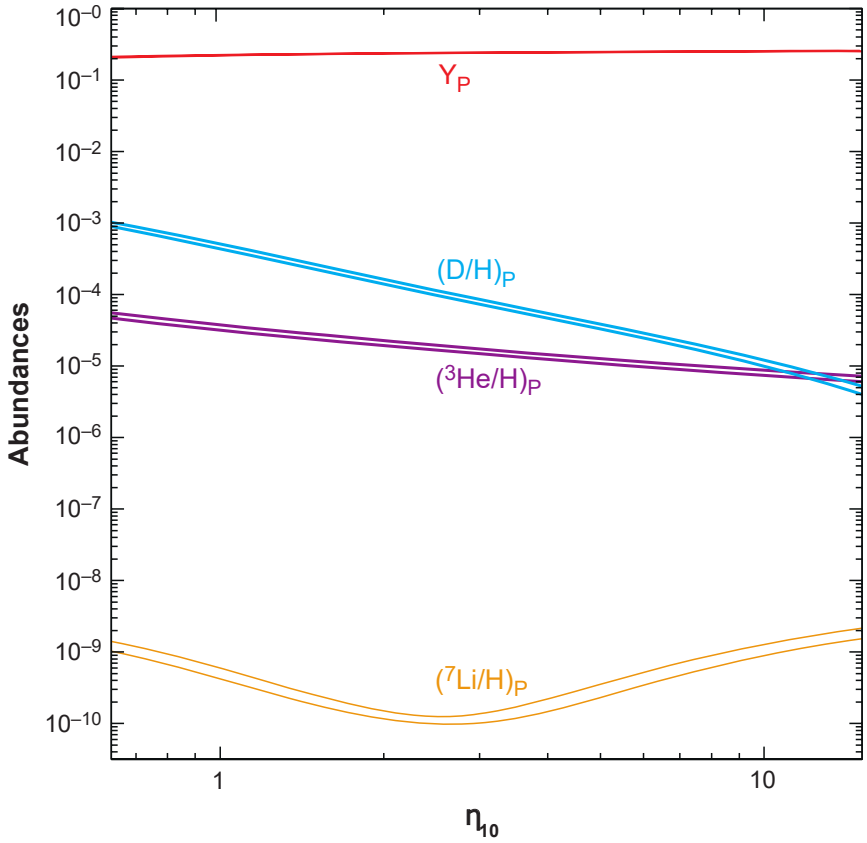

Figure 1.5: Abundance of several species as a function of the relative number density of baryons. η_{10} (x-axis) is defined as the ratio of the number density of baryons to the number density of CMB photons $\eta_{10} = 10^{10}(\frac{n_B}{n_\gamma})$. Y_P is the ^{4}He mass fraction. Y_P is relatively insensitive to the baryon density, so that the baryon density is better inferred from the other species. Plot from [14].

protons per neutron as initial state (from Boltzmann statistics and neutron decay rate), for each deuteron we expect 12 protons (assuming 100% efficiency of the reaction), so that at the end of the nucleosynthesis, 25% of the baryonic mass is in form of ^{4}He and the rest is hydrogen (red line in Fig. 1.5). We can see from the blue line in Fig. 1.5, that the deuteron-to-hydrogen ratio is the quantity with the greatest sensitivity to the baryon density. The reason is that the higher the baryon density, the faster the deuteron reacts to form heavier nuclei. At the end of the nucleosynthesis we are left with less deuteron as the baryon density increases. Depending on which species of nuclei one uses to derive the baryon density, the result may vary slightly. The results using deuteron and ^{3}He are in very good agreement ($\Omega_{baryons} = 0.047 \pm 0.003$ and $\Omega_{baryons} = 0.041^{+0.016}_{-0.010}$ respectively), while other species lead to lower values. The data and their discussion can be found in [14]. The important aspect is that the baryon density inferred from the Big Bang Nucleosynthesis can only account for up to 5% of the Universe energy density.

1.2.3 The Bullet cluster

As was highlighted in the introduction to this chapter, the historical development of the idea of dark matter started with the observation of galaxy clusters. An impressive example of how dark matter affects the dynamics of galaxies comes from the observation of two clusters, which somewhen in the past experienced a collision. Because of the peculiar shape, these clusters are often referred as the **Bullet Cluster**. This was first identified in 1995[15] and later became compelling evidence for the existence of dark matter[16]. The

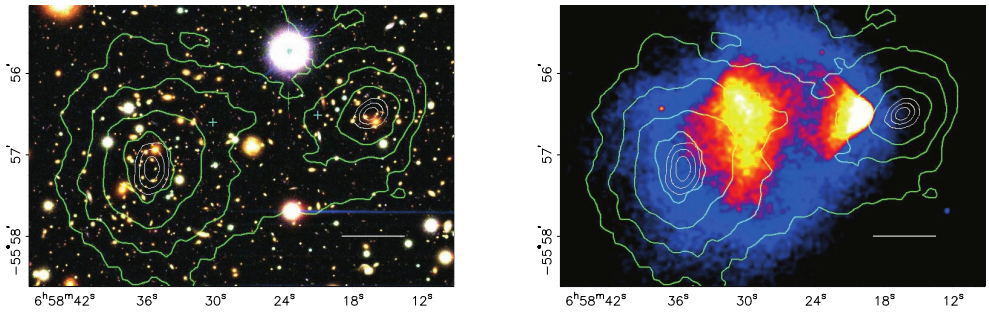

Figure 1.6: Optical picture of the bullet cluster (left) and X-ray emission (right). The green contours represent equipotential lines of gravity. From the X-ray emission the gas distribution can be inferred. The overlay of the equipotential lines and the gaseous components of the cluster shows that there is an undetected mass distribution which shifts the gravitational centres away from the two most dense regions of the gas.

baryonic matter composing the two clusters is mainly present in the form of intergalactic gas, while a smaller fraction makes up the stars of the galaxies. The gaseous component of the matter can be seen from Earth looking at the X-ray emission of the clusters (Fig. 1.6, right picture). The specific pattern of the gas is a consequence of the friction between the two clusters during their collision (friction mediated solely by the electromagnetic force). The optical picture (Fig. 1.6, left picture) is used to draw the equipotential gravity contours (green lines) making use of the optical distortion which the stars behind the two clusters undergo due to gravitational lensing. It becomes apparent, comparing the two pictures, that the two centres of gravity do not overlap with the two most dense regions of the visible gas. Assuming the existence of dark matter the phenomenon has a clear explanation: while the friction slew down the two gaseous components of the clusters, the largest fraction of the matter, which is in form of dark matter, went through with little to no interaction (other than gravity), resulting in two centres of gravity misplaced with respect to the two centres of mass of the (baryonic) gas.

1.2.4 Rotation of Galaxies

Convincing evidence at a (relatively) small scale, compared to what is discussed before, comes from the measurements of the rotation velocity of galaxies, including our Milky Way. The measurement of the rotation curve of a galaxy is rather simple; it relies on the

determination of the redshift of known spectral lines, usually the 21cm[17] coming from hydrogen, and the angle under which the galaxy is observed. Spiral galaxies are of great interest because they usually have a central bulge which contains most of the luminous matter, whose density decreases as its distance from the bulge r increases. Making use of classical mechanics we can predict the velocities of the stars v at a given distance from the galactic centre r. Making use of the virial theorem:

$$2\langle T\rangle + \langle V(r)\rangle = 0 \tag{1.13}$$

where T is the kinetic energy and V the potential (gravitational) energy generated by the mass enclosed in a sphere of radius r. Assuming that most of the mass is concentrated in the central bulge of radius r_{bulge}, we can deduce that the velocity of a star at a distance $r > r_{bulge}$ is:

$$\begin{aligned} mv^2 &= \frac{GMm}{r} \\ v &= \sqrt{\frac{GM}{r}} \end{aligned} \tag{1.14}$$

where G is the gravitational constant, m is the mass of the observed star, and M is the total mass in the galactic bulge. The relevant feature of v is its proportionality to $1/\sqrt{r}$. Experimental observations (such as the measurement of the velocities in the galaxy M33, see Fig. 1.7 and [18] for a detailed description of the data treatment and the extrapolation of the dark matter distribution) show a completely different dependence of the velocity distribution. v does not decrease as r gets larger, in fact it has the tendency to slightly increase. In order to account for the observed velocity distribution, it is necessary to consider an additional contribution to the mass profile of the galaxy (dashed-dotted line in Fig. 1.7). This additional mass perfectly fits the dark matter paradigm, as it eludes telescopes detection, but it also plays a crucial role in the dynamics of the galaxy due to its large abundance.

1.3 Dark Matter candidates

All the evidence discussed in the previous sections (and many others) convinced the scientific community that a large fraction of the matter in the Universe is not in the form of baryonic matter. The qualification of this type (or several types) of matter as *dark* is a direct consequence of our lack of knowledge of its nature. The great challenge of particle physics is the investigation of the elementary properties of dark matter particles. Dark matter is a fundamental brick of cosmological models but, at the time of writing, remains undetected in terms of particles. Therefore, its study is considered key to access a physics beyond the Standard Model and considerable efforts are being made to improve and develop experimental techniques to explore its nature. A short list of possible particle candidates to explain dark matter is given below.

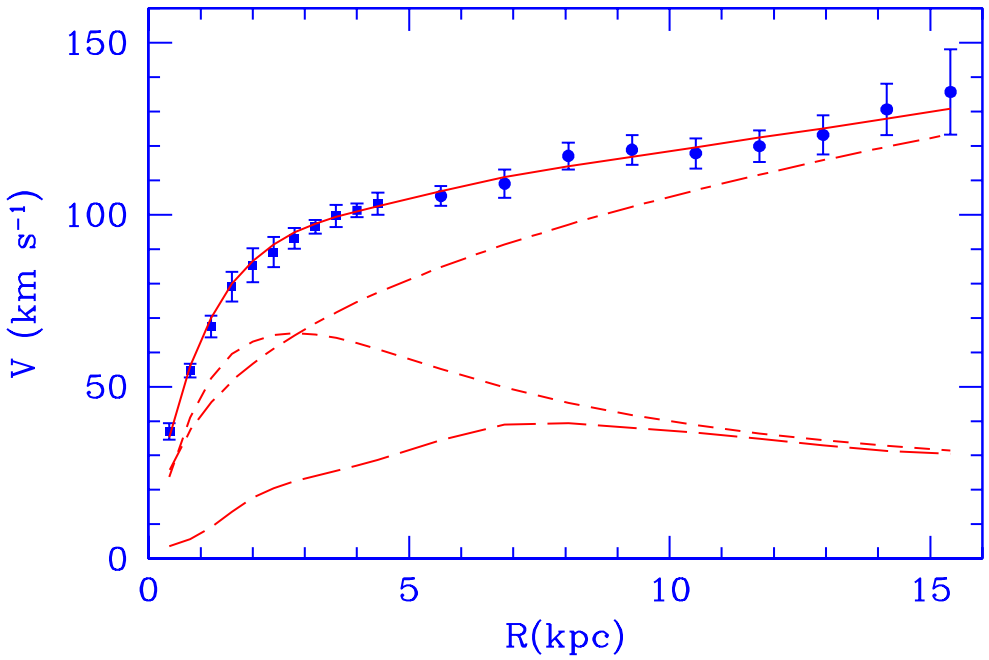

Figure 1.7: Measured rotation velocity of stars in the galaxy M33 (points). The long dashed line represents the contribution from the gaseous component of the galaxy, the short dashed line the contribution from stars. The dashed-dotted line is the "missing contribution" due to the dark matter Halo. The solid line is the model accounting for all contributions. Picture from [18].

1.3.1 Axions

Axions are hypothetical particles originally introduced to solve the so-called **strong CP-problem**. The weak interaction is known to violate the CP symmetry, while the strong interaction does not do so, even though QCD explicitly allows for a CP-violating term. This term is not predicted by the theory and must be inferred from experiments. CP violation in the strong force would show up as a non-vanishing electric dipole of the neutron, but strong limits are set on that quantity[19], so that strong CP violation has a very tiny effect.

A solution to explain the non-violation of the CP symmetry in the strong interaction is the Peccei-Quinn mechanism[20] which predicts the existence of a new type of particle, the axion. The idea of axions can be made more general than just the solution of the strong CP-problem and axion-like particles (**ALP**) appear in several extensions of the Standard Model[21].

Because of their properties, axions are a well motivated candidate to explain a large fraction of the dark matter in the Universe[22].

The experimental efforts addressed towards the detection of axions can be divided into two main categories: helioscopes and haloscopes. Helioscopes search for axions emitted by the Sun, while haloscopes detect relic axions. The **CAST**[23], an experiment located

at CERN and consisting of a detector which tracks the position of the Sun and is kept aligned to it, belongs to the former category. **ADMX**[24] is an experiment of the latter, where the detector consists of a cryogenic resonant microwave cavity optimised to detect relic (cold) axions.

Both experiments are searching for axion-to-photon conversion in a strong magnetic field (Primakoff effect).

1.3.2 WIMPs

The **W**eakly **I**nteracting **M**assive **P**articles are a general class of new particles with a somewhat loose definition. They are required to be massive, between a few GeV/c^2 up to the TeV/c^2 scale, stable (at least on the cosmological time scale), and to interact with Standard Model particles on the weak scale or below (in this framework, "weak" does not need to be the Weak force of the Standard Model). General assumptions about WIMPs are their creation in the early Universe and their thermal equilibrium with all the other particles present at that time. In the present-day Universe, WIMPs are thermal relics that supply the "missing mass" to account for the gravity which cannot be explained by the sole luminous matter. The lower and upper bounds on the WIMP mass are set to account for the present day Universe's appearance. Under the assumption of WIMPs being the dominant dark matter component, too light WIMPs would result in an excessively large Ω_χ. On the contrary, the upper bound to the WIMP mass is set by the interaction cross-section, which cannot be arbitrarily large. The lower bound is of particular interest for the CRESST experiment and this thesis work. Lee and Weinberg proved that a stable lepton, in their work a "heavy neutrino", has to be heavier than 2GeV/c^2[25], based on cosmological arguments. No lower bound is foreseen in the case of WIMPs being a subdominant component of the dark matter present in the Universe.

The thermal equilibrium of the WIMPs in the early Universe means that they were continuously produced and annihilated via interactions with standard model particles:

$$\chi\bar{\chi} \Leftrightarrow f\bar{f} \tag{1.15}$$

Following the cooling of the Universe, the creation rate of $\chi\bar{\chi}$ pairs dropped, leaving only the dark matter annihilation channel. Having a limited amount of $\chi\bar{\chi}$ particles, the effect of the expansion of the Universe is the dilution of these particles[5], so that their density does not allow for an efficient annihilation, therefore WIMPs are referred to as thermal relics. Their number density can be estimated using the Boltzmann statistics $e^{-\frac{m_\chi}{T}}$ when T falls below the value which allows the bi-directional process in Equation 1.15 (the so-called thermal freeze-out). In Figure 1.8 the evolution of the WIMP number density is plot over time. WIMPs are one of the most favoured candidates to explain dark matter because their mass and cross-section nicely fit the dark matter abundance expected from cosmological observations. In addition, several extensions of the Standard Model, such as SUSY, predict the existence of particles with the same properties as WIMPs[26].

[5]The dilution effect is stronger for the WIMPs than for the ordinary particles because of their large mass (given their known density).

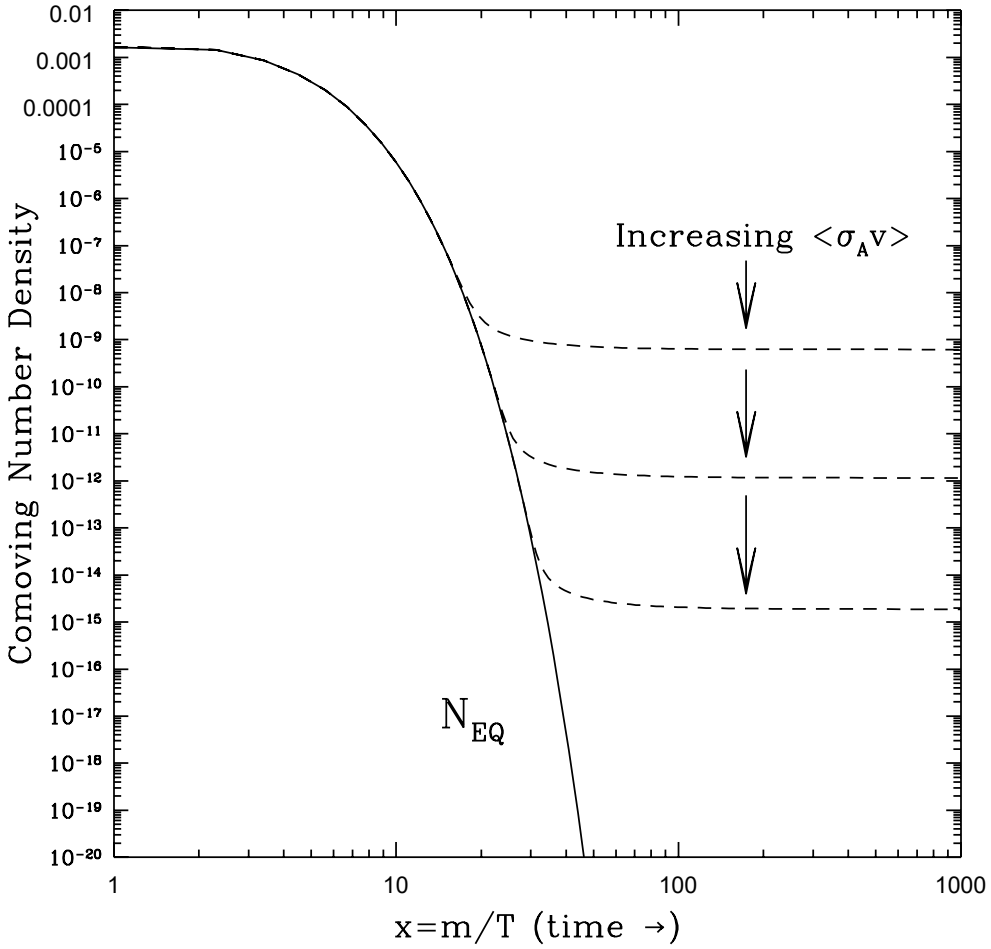

Figure 1.8: WIMPs number density as a function of time for different cross-sections. As the cross-section gets larger, the WIMPs stay in equilibrium longer, resulting in a lower abundance at present-day. Dashed lines refer to plausible cross-sections allowing for the observed dark matter density in the modern Universe. Plot from [26].

1.3.3 Asymmetric Dark Matter

The main motivation for asymmetric dark matter models comes from the consideration that $\Omega_\chi \simeq 5\Omega_{baryonic}$. The critical appeal of WIMPs comes from the right dark matter abundance, given a generic weak-scale annihilation cross-section which loosely depends on the WIMP mass (often called the "WIMPs miracle" because it connects results from astronomical observations to the ones from experimental particle physics in a rather simple way). However, the main drawback is to accept the similarity of the baryonic matter abundance and the one of dark matter as a mere coincidence. Assuming that this similarity between the two abundances originates from a common, strong connection between visible matter and dark matter is the starting point of Asymmetric models. For an in-depth review of these models refer to [27].

In the present-day Universe, the number density of baryons utterly prevails over the one of antibaryons. This fact is explained assuming that somewhen in the early Universe a tiny excess of baryons over antibaryons was present and resulted in the current observable ratio of baryons/antibaryons. This tiny excess is parametrised and quantified:

$$\eta(B) \equiv \frac{n_B - n_{\bar{B}}}{s} \simeq 10^{-10} \tag{1.16}$$

where n_B and $n_{\bar{B}}$ are the baryon and antibaryon number density respectively, and s is the entropy density. All the baryons making up the present Universe are a fraction of the total baryons which survived the baryon-antibaryon annihilation (Equation 1.16, see [28] for details about matter-antimatter asymmetry).

Asymmetric dark matter models assume that the relic dark matter particles are the result of an excess over dark matter anti-particles in the early Universe and that there is a connection between the baryon-antibaryon asymmetry and the one of dark matter particles-antiparticles. This connection is then assumed to have decoupled after an early cosmological epoch[27].

From an experimental point of view, indirect detection of asymmetric dark matter is not possible since there is no dark matter antiparticle left and testing of the models can be done via collider and direct detection experiments. It is interesting to note that asymmetric dark matter in direct detection experiments has the same signature as the WIMPs, but is not bound to the Lee-Weinberg limit, so it offers a set of well-motivated models predicting dark matter particles with masses in the range [0.1-10]GeV/c^2[29].

Chapter 2

Experimental searches

Despite the strong astronomical evidences discussed in the previous chapter, at the time of writing there is no uncontroversial claim for a signal of dark matter particles. All experimental approaches to detect such particles have a common assumption: there has to be some form of coupling (other than gravity) between dark matter particles and ordinary, Standard Model particles. Depending on the way we look at this coupling, we can group experimental searches into three families.

Collider searches aim to create dark matter particles as a product of high energy reactions with Standard Model particles in the initial state.

Indirect searches are looking for the signature of dark matter particles annihilating into Standard Model particles. Such a signature is being hunted for by scanning particles and radiation of cosmic origin.

Direct searches are Earth-based experiments targeted to detect dark matter particles present in the local halo interacting with ordinary matter in particle detectors.

The three approaches are competing to find the first positive signature for the existence of dark matter particles, but in the long term they play a complementary role, as they are all necessary to characterise the possible new particles and prove them to be the dark matter shaping the Universe in the way we know it.

A brief overview of collider and indirect searches will be given at the beginning of this chapter. The main focus, however, is on direct searches to lay the groundwork for discussing the CRESST experiment, within which this thesis work was developed.

2.1 Dark Matter production in colliders

Colliders are one of the most powerful tools which allow physicists to investigate elementary properties of particles. The high energies at which these devices operate are such that it is possible to have a glimpse of what the early, hot and dense Universe looked like. Collider experiments also traditionally discover new particles that cannot exist under normal conditions.

Dark matter candidates investigated with colliders must satisfy the general dark matter

properties known from the cosmological observations (see Chapter 1), i.e. candidate particles have to carry no electromagnetic or colour charge, and need to be stable.

Despite the discovery potential for new particles, colliders cannot prove that a possible dark matter candidate is the one making up the dark matter present in nature and that its lifetime is infinite or at least in the order of the age of the Universe.

2.1.1 Effective Field Theories

Effective Field Theories simplify the physics of particle interaction, assuming that the energy at which the new physics stands out is much larger than what is experimentally accessible. Using Q_{tr} to signify the momentum transferred and m_{med} to signify the mass of the mediator, we can expand the propagator as follows[30]:

$$\frac{1}{Q_{tr}^2 - m_{med}^2} = -\frac{1}{m_{med}^2}\left(1 + \frac{Q_{tr}^2}{m_{med}^2} + \mathcal{O}\left(\frac{Q_{tr}^4}{m_{med}^4}\right)\right) \tag{2.1}$$

Effective field operators correspond to the leading order expansion in Equation 2.1. The approximation holds as long as $Q_{tr}^2 \ll m_{med}^2$ so that the mediator cannot be created. The parameters of the UV-complete theory are connected to the low energy effective operators via[31]:

$$\frac{1}{\Lambda^2} = \frac{g_q g_{DM}}{m_{med}} \tag{2.2}$$

In Equation 2.2, Λ is the energy scale of the new physics, g_q and g_{DM} are the couplings of the mediator to the Standard Model particles q and to the dark matter particles respectively, and m_{med} is the mass of the mediator. A visual depiction of such coupling is given in Figure 2.1. This simplification is intended to directly assess the energy scale Λ and results

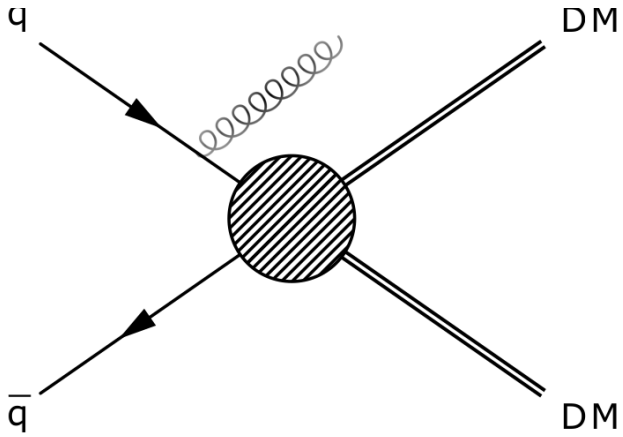

Figure 2.1: Example of effective coupling of Standard Model particles $q\bar{q}$ and dark matter particles. The bubble "hides" the structure of the interaction. Picture from [32].

in a finite set of effective operators to be constrained[33], neglecting the details of the interaction (the mediator is integrated out). The initial states may radiate photons or

gluons (or even heavy SM particles at LHC) with momentum X, used to tag the event, while the dark matter particles of energy E_T escape the detector with no energy deposition within the detector. E_T is determined as the missing transverse energy of the event and the sought-for signature of dark matter particle production is $E_T + X$, often called "mono-X".

The validity of this approach is limited to the case of a momentum transfer much smaller than the mediator mass.

2.1.2 Simplified models

The high energies at which particles collide at LHC make the assumption of a low momentum transfer weak, since the mediator mass is unknown. A complete description of the physics of dark matter involves two new particles, namely the dark matter particle itself and the mediator which provides the coupling to the Standard Model. Simplified models, which make use of renormalizable operators, are designed to include the mediator in the interaction and reflect the relevant kinematics and final states with the introduction of a minimal set of new parameters[30].

2.2 Indirect search: dark matter signature in cosmic rays

The majority of matter in the Universe comes in the form of dark matter, so a fingerprint of dark matter particles annihilating into Standard Model particles could be present in cosmic rays. Indirect detection experiments aim to find such fingerprints by studying particles in cosmic rays of different origins.

The self-annihilation of dark matter, that played a central role in the freeze-out process (see Chapter 1), can lead to a significant flux of various particles such as γ-rays, neutrinos, positrons, or antiprotons[34]. Depending on the nature of the investigated particles, different signatures of dark matter annihilation are expected:

- γ-s may be produced directly by the annihilation of dark matter particles. In this case, they should show up as a gamma-ray monochromatic line in the energy spectrum which can easily be discerned from the astrophysical background, and this is generally considered as a "smoking gun" signature. Another "sharp spectral feature" can come from an internal bremsstrahlung[35], where three bodies are present in the final state, one of which is an irradiated photon whose energy is close to the mass of the annihilating dark matter particle. γ-s can also be produced by subsequent processes, leading to a continuous spectrum where relevant features are less prominent.

- Antiparticles such as positrons or antiprotons, being charged, are diffused by the galactic magnetic field, so that their origin cannot be tracked down. However, dark matter annihilation is expected to leave a signature, typically a bump in the energy spectrum, with a cut-off at the mass of dark matter.

- Neutrinos can also be present as final products of dark matter annihilation. Similarly to γ-s, they propagate unabsorbed in a straight line through the Galaxy. The detection of neutrinos is much harder than for the other particles. Their observation relies on huge underground Cerenkov detectors, such as SuperKamiokande[36] and IceCube[37], where showers of secondary charged particles created by the primary interaction are used to reconstruct the energy and direction of the incident neutrino.

2.3 Direct Search

In contrast to indirect and collider searches, which use Standard Model particles to infer about their origin as products of some kind of dark matter interaction, direct searches are addressed to detect dark matter particle interactions within the sensitive volume of a detector. As seen in Chapter 1, dark matter is distributed in the Universe together with luminous matter and, thus, in the solar system as well. In this picture it is possible for the existing dark matter particles to interact with ordinary matter, opening up the possibility for dark matter detection in Earth-bound experiments.

The main challenge for direct detection is the development of technologies sensitive to very low count-rates, being the cross-section for dark matter interacting with ordinary particles of the weak scale (or below). Because of this, direct searches are low-background experiments usually located in deep, underground facilities, where extremely sensitive detectors can be operated without being blinded by radiation from environmental radioactivity or of cosmic origin.

2.3.1 The elastic scattering

In order to profile the experimental signature for dark matter particles interacting in detectors, a certain number of assumptions is required. The most common scenario assumes a halo of dark matter particles interacting mainly via coherent, elastic scattering off nuclei in matter.

The interaction of a dark matter particle with a nucleus is a two-body problem and its (non-relativistic) energy transfer E_R reads:

$$E_R = \frac{q^2}{2m_N} = \frac{\mu^2 v^2}{m_N}(1 - \cos\theta) \tag{2.3}$$

In Equation 2.3 q is the momentum transferred to the nucleus, m_N is the nuclear mass, μ the reduced mass of the system dark matter particle + nucleus, v the relative velocity of the incident particle, and θ the scattering angle in the center-of-mass frame.

A first estimate of the maximum expected transferred energy E_R^{max} can be obtained assuming a dark matter particle mass m_χ of 100GeV/c^2 and a relative velocity v of 200km/s[38],[34]:

$$E_R^{max} \simeq 90 \left(\frac{m_\chi}{100\text{GeV}}\right)^2 \left(\frac{100\text{GeV}}{m_N}\right)^2 \left(\frac{v}{200\text{km} \cdot s^{-1}}\right)^2 \text{keV} \tag{2.4}$$

From the expression in Equation 2.4 the recoiling energy of a nucleus is $\mathcal{O}(100)$keV, while in case of a recoiling electron the energy would be in 1-10eV range. The detection of dark matter particles scattering off electrons is beyond the scope of this thesis.

The energy transferred to a recoiling nucleus shows that the dark matter particles scattering off nuclei is a low-energy process and the interaction is certainly of the type which can be described in the framework of effective field theories. The low energies involved are such that a dark matter particle cannot resolve the nuclear structure of the target nucleus and, therefore, the whole nucleus recoils resulting in a coherent scattering. This can be seen evaluating the de Broglie wavelength for a dark matter particle of 100GeV/c^2 of mass:

$$\lambda = \frac{h}{p} = \frac{hc}{mc^2\frac{v}{c}} = \frac{1240\text{MeV}\cdot\text{fm}}{100\text{GeV}\cdot 10^{-3}} \simeq 12\text{fm} \tag{2.5}$$

The wavelength in Equation 2.5 is such that the incident dark matter particle does not "see" the internal structure of the nucleus and a coherent interaction is favoured.

The scattering process might in principle lead to an excited state for the recoiling nucleus, meaning that the scattering is inelastic and the kinetic energy is not conserved. In what follows, only the elastic scattering is considered. The interested reader can find a study of dark matter inelastically scattering off Xenon target nuclei in [39].

2.3.2 The interaction rate

The event rate for dark matter particles interacting in particle detectors is the main challenge that direct detection experiments are faced with. At first we can estimate the count rate Γ for dark matter particles scattering off nuclei with the formula:

$$\Gamma = n\Phi\sigma \tag{2.6}$$

where n is the number of target nuclei, Φ is the flux of dark matter particles crossing the volume enclosing the target nuclei, and σ is the cross-section for the scattering process. Equation 2.6 can be expressed in terms of the target mass M_{target}, the nuclear mass m_N, the dark matter particle mass m_χ, the local density of dark matter ρ_χ, and the average incident velocity of dark matter particles $\langle v\rangle$:

$$\Gamma = \frac{M_{target}}{m_N}\frac{\rho_\chi}{m_\chi}\langle v\rangle\sigma \tag{2.7}$$

We can estimate Γ plugging some typical value into Equation 2.7:

$$\Gamma \simeq 0.0324\frac{\frac{M_{target}}{1\text{kg}}}{\frac{A}{100\text{amu}}}\frac{\frac{\rho_\chi}{0.3\text{GeV/c}^2/\text{cm}^3}}{\frac{m_\chi}{100\text{GeV/c}^2}}\frac{\langle v\rangle}{200\text{kms}^{-1}}\frac{\sigma}{1\text{pb}}\ \text{counts/day} \tag{2.8}$$

Being able to detect such count rate is an ambitious task and indeed a very low background is mandatory to be sensitive to such a weak signal. In the following sections, the actual sought-for energy spectrum is derived and an outline of the current experimental approaches is given.

2.3.3 The experimental signature

The relevant quantity which is measured by direct detection experiments is the differential event rate $\frac{d\Gamma}{dE_R}$. In order to have an expression for it, we must first re-write Equation 2.7 in its differential form, making the dependence on the dark matter particle incident velocity and the recoiling energy explicit, and introducing the dark matter particle velocity distribution $f(\overline{v})$:

$$\frac{d\Gamma}{dE_R} = \frac{\rho_\chi}{m_N m_\chi} \int_{v_{min}}^{\infty} d^3\overline{v} f(\overline{v}) v \frac{d\sigma(v, E_R)}{dE_R} \tag{2.9}$$

where v_{min} is the lowest velocity that can transfer E_R energy to the recoiling nucleus (meaning $\cos\theta = -1$ in Equation 2.3):

$$v_{min} = \sqrt{\frac{E_R m_N}{2\mu^2}} \tag{2.10}$$

The differential cross-section $\sigma(\overline{v}, E_R)$ embodies the physics of the dark matter particle-nucleus interaction and it consists in general of scalar and vector couplings. The latter describes the interaction of the dark matter particle with the net spin of the target nucleus. Sensitivity to the spin-dependent interaction requires target nuclei with a non-vanishing net spin, but the relevant target in this thesis work ($CaWO_4$) does not have a significant nuclear spin. Therefore, we will neglect spin-dependent interactions in the following sections.

Differential cross-section

The differential cross-section for spin-independent dark matter particle-nucleus scattering reads[40]:

$$\left(\frac{d\sigma}{dE_R}\right)_{SI} = \frac{m_N \sigma_0}{2\mu^2 v^2} F^2(E_R) \tag{2.11}$$

In Equation 2.11 σ_0 is the point-like, zero-momentum cross-section for the scattering process, while $F(E_R)$ is the form factor. σ_0 has the form:

$$\sigma_0 = \frac{4}{\pi} A^2 f^2 \mu^2 \tag{2.12}$$

where f is the strength of the coupling and it is generally considered to be equal for protons and neutrons. The term A^2 represents the enhancement of the interaction due to coherence. It is of course the case that, in general, heavy targets are specially considered for direct detection of dark matter because of the quadratic dependence on the atomic mass number A. At zero-momentum transfer, the nucleus can be thought of as a point-like particle since the spin-independent interaction is coherent, but at higher momenta transfer, it is necessary to account for loss of coherence in the interaction.

The form factor

The form factors used in direct searches are usually computed with the Helm parametrisation[41]. The idea is to consider the nucleus spatially as a sphere with constant density and take its convolution with a gaussian to have a smoothly decreasing density at the edge of the nucleus. The form factor is then the Fourier transform of such distribution and it can be written as:

$$F(q) = 3\frac{j_1(qR_0)}{qR_0}\exp\left(-\frac{1}{2}q^2s^2\right) \tag{2.13}$$

where j_1 is the first spherical Bessel function, R_0 is the radius of the sphere with constant density ($\simeq$ the nuclear radius), $q = \sqrt{2m_N E_R}$ the transferred momentum, and s the width of the gaussian used to smoothen the density distribution ($\simeq$1fm). The main focus of this thesis work concentrates on light dark matter particles where the transferred momenta are such that the form factor plays a negligible role.

Velocity distribution

The last quantities needed in Equation 2.9 are the dark matter density ρ_χ and the dark matter particle velocity distribution $f(\overline{v})$. The former is known from the cosmological observations discussed in Chapter 1, while the latter depends on the specific type of dark matter. In the common WIMP scenario, dark matter particles are thermalized in the early Universe, so their expected velocity distribution is the Maxwell-Boltzmann for an isothermal sphere in the rest frame of the Milky Way. The velocity distribution has an upper truncation limit v_{esc} due to the fact that particles with a velocity greater than the escape velocity cannot be confined within the galactic volume. The expression for $f(\overline{v})d\overline{v}$ is [42]:

$$f(\overline{v})d\overline{v} = \frac{1}{\mathcal{N}}\left(\frac{3}{2\pi v_{rms}^2}\right)^{\frac{3}{2}}\exp\left(-\frac{3v^2}{2v_{rms}^2}\right)\theta(v - v_{esc})d\overline{v} \tag{2.14}$$

where the normalization constant $\mathcal{N}$ and the root mean square velocity v_{rms} are:

$$\begin{aligned}\mathcal{N} &= \mathrm{erf}(z) - \frac{2}{\sqrt{\pi}}\exp(-z^2)\\ z^2 &= \frac{3v_{esc}^2}{2v_{rms}^2}\\ v_{rms} &= \sqrt{\frac{3}{2}}v_s\end{aligned} \tag{2.15}$$

Here, v_s is the rotational velocity of the Sun in the galactic rest frame. Standard values used in direct detection experiments for the velocities in Eqs. 2.15 are $v_{esc} = 544$km/s[43] and $v_s = 220$km/s[38].

It is important to point out that even though we make use of the velocity distribution of a specific dark matter paradigm, the WIMPs, the crucial assumption of a spherical

isothermal dark matter distribution in the galaxy (i.e. the Maxwell-Boltzmann velocity distribution) holds regardless of the specific Cold Dark Matter model we rely on. This fact was proven by Lynden-Bell in a work explaining the observed light distribution in elliptical galaxies and it is related to the dynamics of newly formed galaxies[44].

The recoil spectrum

Having determined all the relevant inputs from nuclear physics and astrophysics required in Equation 2.9, it is possible to predict the shape of a dark matter particle-induced nuclear recoil signal in a direct detection experiment. m_χ and σ_0 are the two unknowns that all the experimental efforts try to measure. The evaluation of Equation 2.9 leads to the product of an exponential function dependent on the recoiling energy $\sim \exp(-E_R)$ and the nuclear form factor. Neglecting the latter for the moment, the interaction rate is described by a simple exponential rising towards the lowest energies with no other specific features. In particular, the magnitude of the exponential is proportional to σ_0, while the decay width is determined by the dark matter particle mass. Being the main interest of the rest of this thesis, an example of dark matter-induced nuclear recoil spectrum in $CaWO_4$, and its individual constituents, for the case of $m_\chi = 100\text{GeV/c}^2$ is shown in Figure 2.2. As $CaWO_4$ is a composite material, the event rate has to be computed for each nuclear species and the total rate is the sum of the single components.

The recoil spectrum can be written in a very easy form, under the approximation of $v_{min} = 0$ and $v_{esc} = \infty$[45]:

$$\frac{d\Gamma}{dE_R} = \left(\frac{d\Gamma}{dE_R}\right)_0 F^2(E_R) e^{-\frac{E_R}{E_C}} \tag{2.16}$$

where the constant in the front is the count-rate at zero-energy transfer and E_C the decay width of the exponential, determined by the kinematics of the nuclear recoil.

2.4 Experimental approaches

Dark matter is one of the biggest mysteries of modern physics and its detection would be an extraordinary breakthrough. Several experiments are searching for a (yet to be found) positive signal and, in doing so, many technologies are constantly developed. As already pointed out in this chapter, the signal we are hunting for is extremely weak. In the specific scenario outlined in the previous section, such a signal consists of around one nuclear recoil per kilo of target every month. The experimental challenge for the detection of very low-rates is posed to all direct detection experiments. Background suppression is indeed critical to improve sensitivity, and this is done in a number of ways. A common choice is to locate the experiment in a deep-underground laboratory, where the cosmic radiation is strongly reduced. Different types of shielding are deployed against environmental radioactivity and naturally all materials in contact with the detectors, and the detectors themselves, are carefully chosen for their cleanliness in terms of radiopurity.

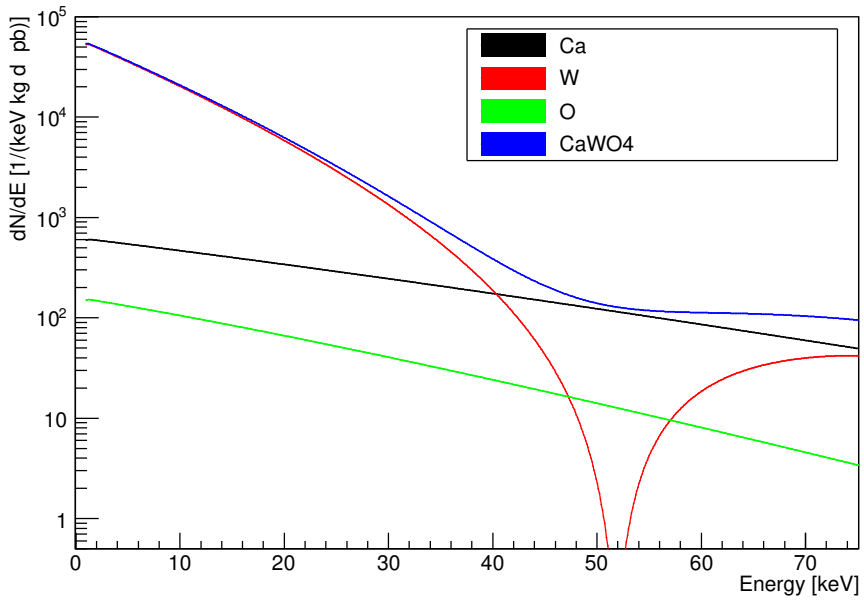

Figure 2.2: Differential energy spectrum of nuclear recoils in $CaWO_4$ for the case of a dark matter particle of mass 100GeV/c^2. The rates of the individual nuclear species present in $CaWO_4$ add up to the total differential event rate of the composite target. As pointed out in the main text, the effect of the form factor does not affect the lowest energy part of the spectrum. In the case of W, the form factor causes the recoiling spectrum to deviate from a pure exponential at around 40keV.

Additional background rejection is possible if the detector is capable of discriminating electron recoil - background only - from nuclear recoil events. A brief overview of different technologies currently employed in direct dark matter searches is given below.

Liquid Noble Gas

Liquid noble gas experiments are those in the field which achieve the largest exposure. In the simplest case, an array of PMTs is faced to the liquefied gas in order to measure the amount of scintillation light emitted as a consequence of a particle interaction, so-called single phase detector. The experiment XMASS[46] makes use of LXe as target material in a single phase detector. The vessel containing the liquefied Xe is placed inside a tank filled with water which serves as a passive shield against γs and fast neutrons and as an active muon veto as well. Another use of liquid noble gasses is in the so-called double phase time projection chambers (TPCs). The typical shape of a TPC is cylindrical and at the two ends an array of PMTs is placed. The scattering causes both the production of scintillation light (S1) and the creation of electron-hole pairs. An electric field applied across the volume of the liquid phase drifts the charge to the interface between the two

phases. In the gaseous phase a large electric field extracts the electrons from the liquid phase and accelerates them in the gas, causing a second scintillation (S2), see Figure 2.3. The arrangement of the PMTs allows for the reconstruction of two of the three coordinates of the interaction site[1]. The time difference between the two scintillation signals is used to reconstruct the third coordinate of the interaction site which is now fully determined. The position reconstruction is used to fiducialize the volume, i.e. reject all scatterings in the vicinity of the inner surface of the TPC. The ratio of the two signals is used to discriminate nuclear recoils from electron recoils, since the latter produce electron-hole pairs more efficiently. The largest operating liquid Xe experiment is Xenon1T[47], consisting of ∼3200kg of ultra-pure Xe. The use of liquid Ar opens the possibility of having an additional discriminating channel, because the duration of the scintillation signal induced by electron recoils is longer than the one induced by nuclear recoils. The difference in duration is apparent in the pulse shape of the scintillation signal and, therefore, electron recoils can be rejected. The pulse shape discrimination in LAr is used in the DarkSide experiment[48].

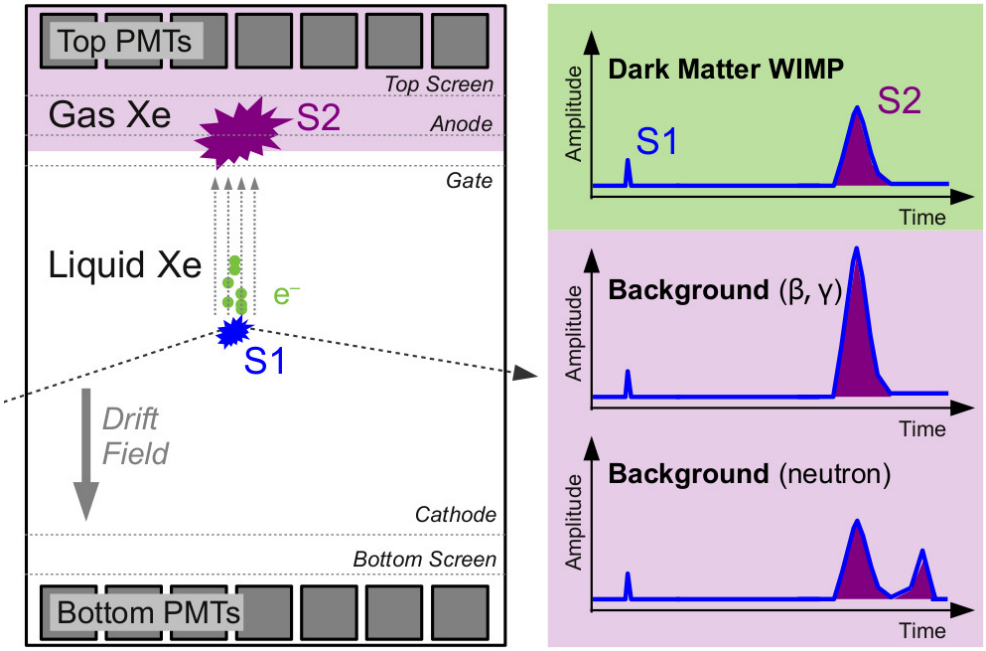

Figure 2.3: Dual phase TPC. A first scintillation is emitted as the incident particle interacts in the liquid Xe and it is read out by the two sets of PMTs. The electrons created as ionisation are drifted to the top part and cause proportional scintillation as they travel through the gaseous phase. This second signal is read out by the same PMTs. The ratio S2/S1 and the multiplicity of S2 are used to reject background events. Scheme from [49].

[1]Being the liquid very clean, electrons do not diffuse while drifting and the xy coordinates of S2 are the same of the interaction site.

Cryogenic Ionisation Experiments

In cryogenic detectors, particle interactions within the sensitive volume of the detector result in a small temperature rise. A thermometer measures such rise and the thermal signal gives a precise measurement of the deposited energy. The Edelweiss and SuperCDMS experiments use Ge crystals as target material. As Ge is a semiconductor, particles scattering in the target cause the creation of electron-hole pairs. The charge is collected by electrodes and measured (ionisation signal). In the Edelweiss experiment, the thermal signal is read with a neutron transmutation thermistor (NTD) while in SuperCDMS, transition edge sensors (TES) are used to accurately measure the heat signal. In both technologies the ratio between the ionisation signal and thermal signal is used to reject electron recoils, which produce more charge than nuclear recoils of the same energy. The design of the applied electric field allows for surface events rejection.

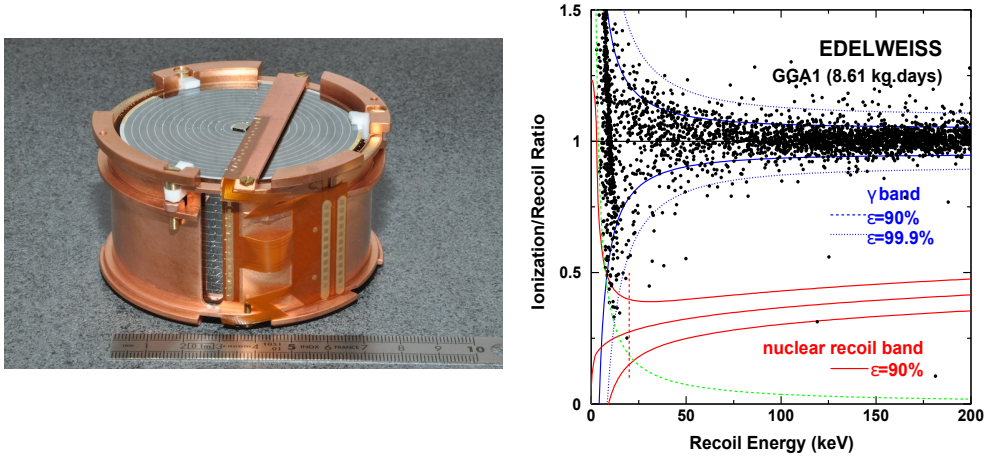

Figure 2.4: Picture of a Ge detector module used in the Edelweiss experiment (left, picture from [50]). On the right is given the ionisation yield vs. energy. The events populate the plane in a two bands structure. The events with low ionisation yield (red contour) are nuclear recoils. Plot from [51].

NaI scintillator

In the DAMA/Libra experiment, 25 ultra-pure crystals of NaI doped with Tl are equipped with two photomultipliers each. The deposition of energy by a particle in a crystal causes scintillation read by the PMTs. Since scattering due to dark matter is highly rare, only single crystal events are considered. The signal studied by DAMA/Libra is different from the one presented in section 2.3. Because of the relative motion of the Earth around the Sun, the flux of dark matter particles crossing the detectors experiences seasonal variation, being maximum on the 2nd of June. The detection of this periodic variation is, in general, out of the reach of most dark matter direct searches. The very large mass of the target (∼100kg) allows DAMA/Libra to investigate such a faint signal and over 13

years of data-taking show the presence of an impressive 9.2σ of significance modulation (see Figure 2.5). The interpretation of such a signal came at the time of writing to no conclusion. Under standard assumptions the signal of DAMA/Libra is firmly excluded by other experiments.

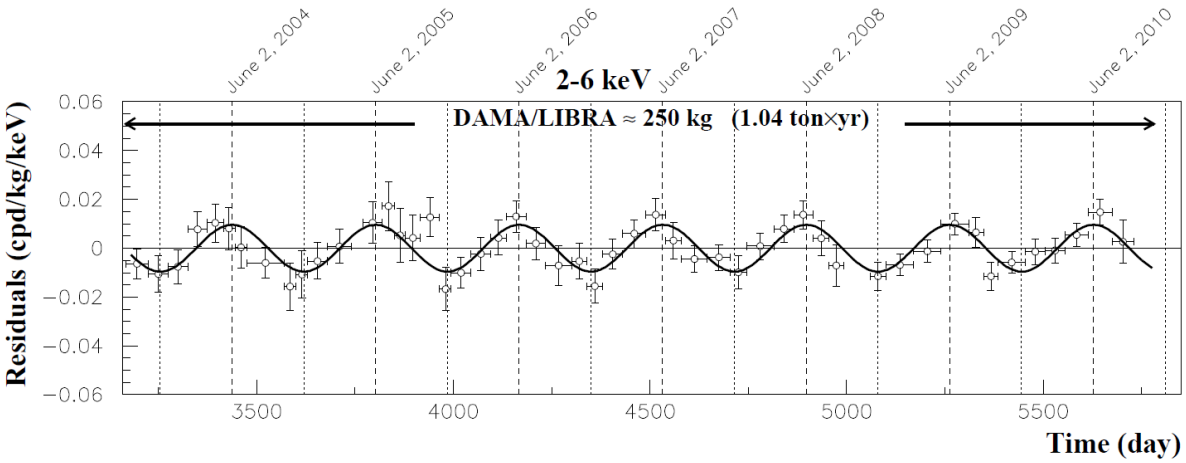

Figure 2.5: Residual rate of single crystal hits in the 2-6keV energy interval. Superimposed is a cosine with period of 1 year and the maxima aligned to the 2nd of June. The modulation of the signal is clearly present. Its interpretation is still under debate. Plot from [52].

Charged-coupled devices (CCDs)

CCDs are silicon detectors originally developed for high-quality, low-noise, digital cameras. The detection principle is the usual one of semiconductor-based detectors: particle interactions cause the creation of electron-hole pairs that are drifted by an electric field, collected, and measured. The amount of detected charge is then related to the deposited energy. Each CCD is made up by millions of pixels and several CCDs can be stacked together, offering accurate spatial information. The DAMIC experiment[53], currently running 40g of CCDs in SNOLAB, successfully demonstrated background rejection capabilities based on imaging techniques. Depending on the specific pattern of charge-clusters created by interacting particles, background discrimination is possible (see Figure 2.6). The next stage of the experiment, DAMIC-M, will operate 1kg of detector at the *Laboratoire Souterrain de Modane*. A novel read-out scheme, based on repetitive, non-destructive measurements of the pixel charge, will allow for a single-charge resolution and sub-eV noise levels. The good energy resolution (aka low threshold) and the relative lightness of the target material (Si) make the sensitivity of DAMIC competitive for dark matter particles with mass $\leq 10\text{GeV/c}^2$. Due to the high costs of realisation, CCDs are not a convenient technology for large-scale experiments.

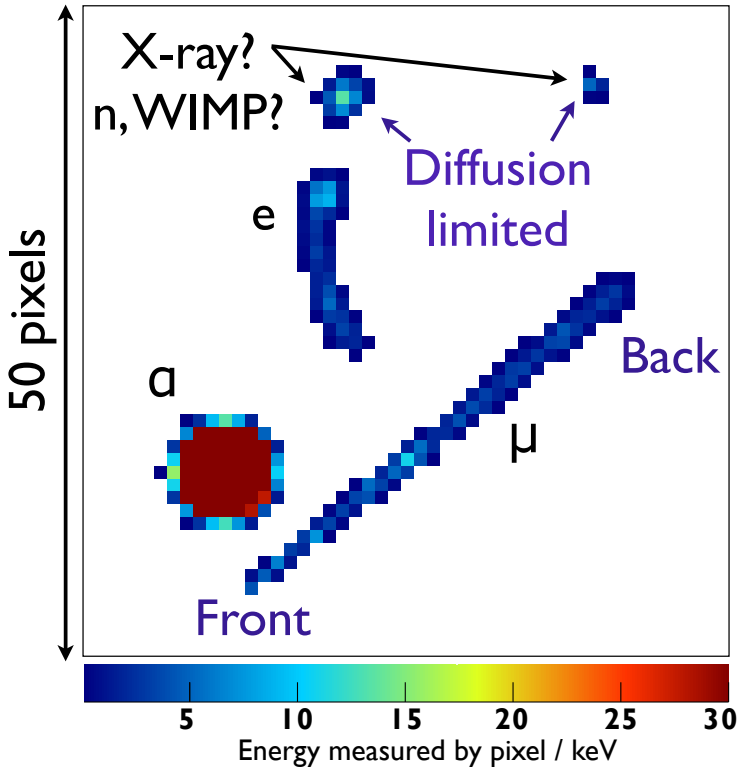

Figure 2.6: Portion of 50x50 pixel image from the DAMIC detector exposed to a ^{252}Cf source. Only pixels with a deposited energy greater than 0.1keV$_{ee}$ are coloured. Different types of interaction can be discriminated by the specific shape of each cluster. Plot from [53].

Spherical Proportional Counters (SPCs)

This kind of detector consists of a spherical vessel filled with a gas. The large outer vessel is electrically grounded and a high voltage is generated at its centre (Figure 2.7). As a particle interacts with the gas, the electrons from the primary ionisation are drifted by the electric field. Because of the spherical shape, the electric field is much higher in the innermost region than in the one close to the outer surface. Primary electrons drift towards the inside of the detector gaining kinetic energy, eventually creating secondary electron-ion pairs. The ions are collected in the grounded outer vessel, where their current is integrated and converted to a voltage, the actual output of the detector[54].

The NEWS-G experiment optimised the technology for light dark matter particle detection. A prototype made of ultra-pure (NOSV) copper with a 60cm-diameter was operated for 42.7 days[55]. The filling gas is a mixture of Neon and CH_4 (99.3% and 0.7% in pressure respectively).

SPCs are an attractive technology for the search of light dark matter particles because they feature a low energy threshold ($\sim$10eV$_{ee}$), a simple and scalable detector design, and the freedom to choose the filling gas allows optimisation of the energy transfer for low

mass particles. Finally, the technology offers the possibility to reject surface background by means of pulse shape discrimination.

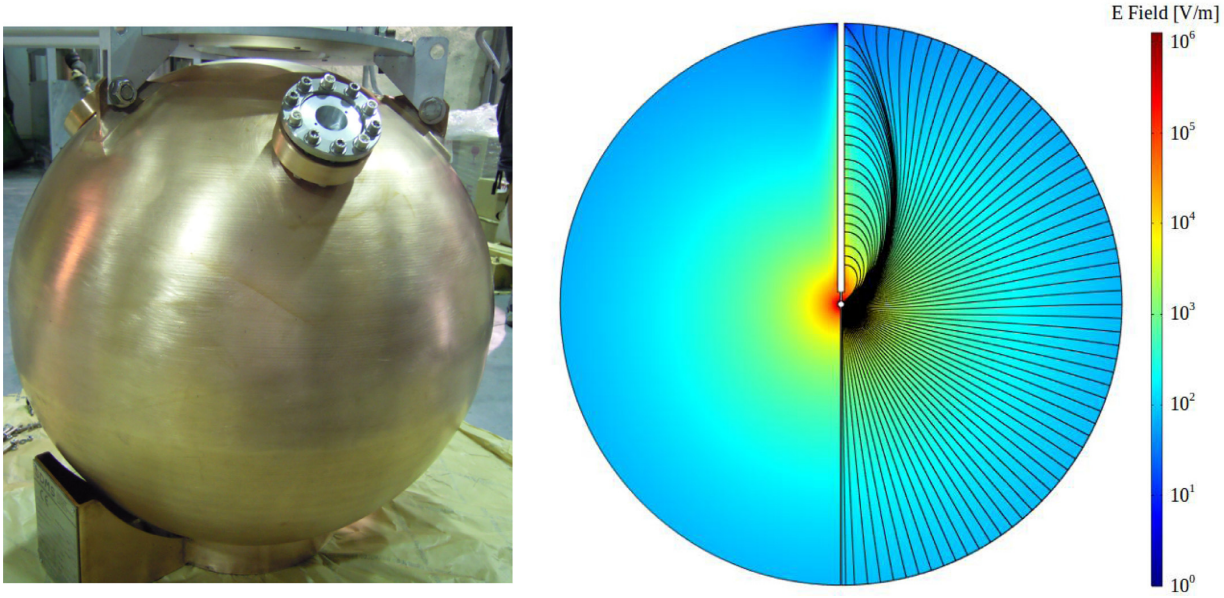

Figure 2.7: Photo of the prototype SPC of the sedine detector (left). Colour-coded on the right is the intesity of the applied electric field. Field lines are drawn for a half of the detector. Plot from [55].

CRESST-II

The CRESST experiment is among the most notorious of dark matter searches. Its second stage employed scintillating $CaWO_4$ crystals operated as cryogenic calorimeters, assembled in modules with a double-channel read-out (an open module is shown in Figure 2.8). One channel is used to precisely reconstruct the amount of energy released in the sensitive volume. The second channel measures the amount of scintillating light produced by the interaction. The two channels together allow us to discriminate different types of interaction, as they have a different scintillation efficiency. In particular, nuclear recoils have the highest light output suppression compared to other interactions of the same energy. The excellent energy resolution and a low energy threshold are prominent features of this dark matter search. The former is required for an accurate profiling of a possible positive signal. The latter is crucial for low mass dark matter sensitivity. Another salient advantage of the cryogenic technique is the true energy output for nuclear recoils, without the need for the electron-equivalent calibration, often critical in charge-based detectors.

In CRESST-II various benchmarks were set. A detector design that allows for surface background rejection was proved[56], which is a very tempting feature for a technology that does not permit volume fiducialisation. A few target crystals were grown within the collaboration, at the Technische Universität München. The control of the growth,

from the raw materials, the Czochralski furnace, and crystals manufacturing resulted in a background improvement compared to the one of commercially available $CaWO_4$ crystals[57]. The most important achievement is an energy threshold of 307eV which extended the sensitivity reach down to $0.5 GeV/c^2$ and a world-leading sensitivity below $1.7 GeV/c^2$[58].

The sensitivities of the main dark matter direct searches at the time of publishing of the CRESST-II results is shown in Figure 2.9. The strategy followed by the CRESST collaboration was to further improve the sensitivity in the low mass region. In doing so, the detector modules were re-designed targeting a threshold $\leq$100eV. Because of major changes in the detector concept, the new stage is named CRESST-III. In the next chapter a detailed description of the new experimental set-up will be given. The main point of this thesis is the improvement of the energy threshold by means of an optimised triggering algorithm and a dedicated data acquisition.

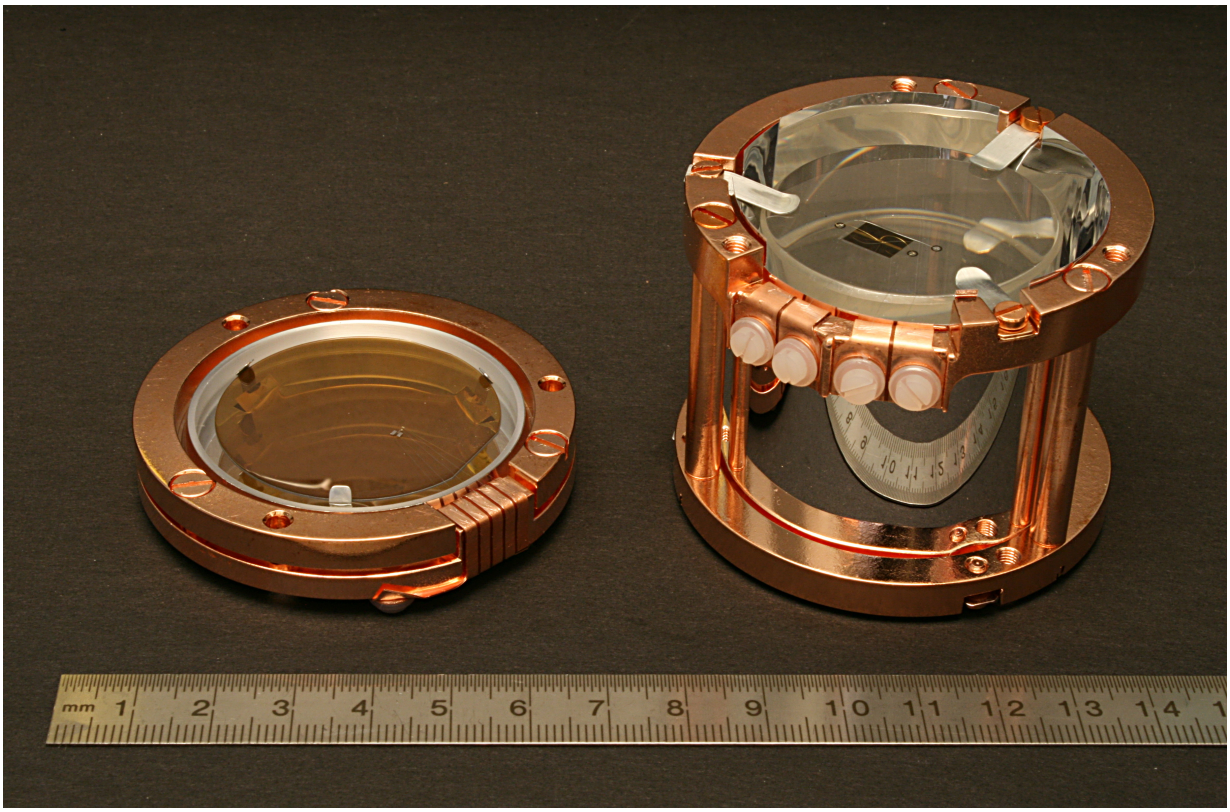

Figure 2.8: Photo of an open CRESST-II detector module. It consists of two independent detectors. The one on the right is the main absorber and its output is the precise energy deposited within its volume. The detector on the left is the light detector which serves the purpose of measuring the scintillation light emitted by the main absorber. The combination of the two signals allows for particle discrimination.

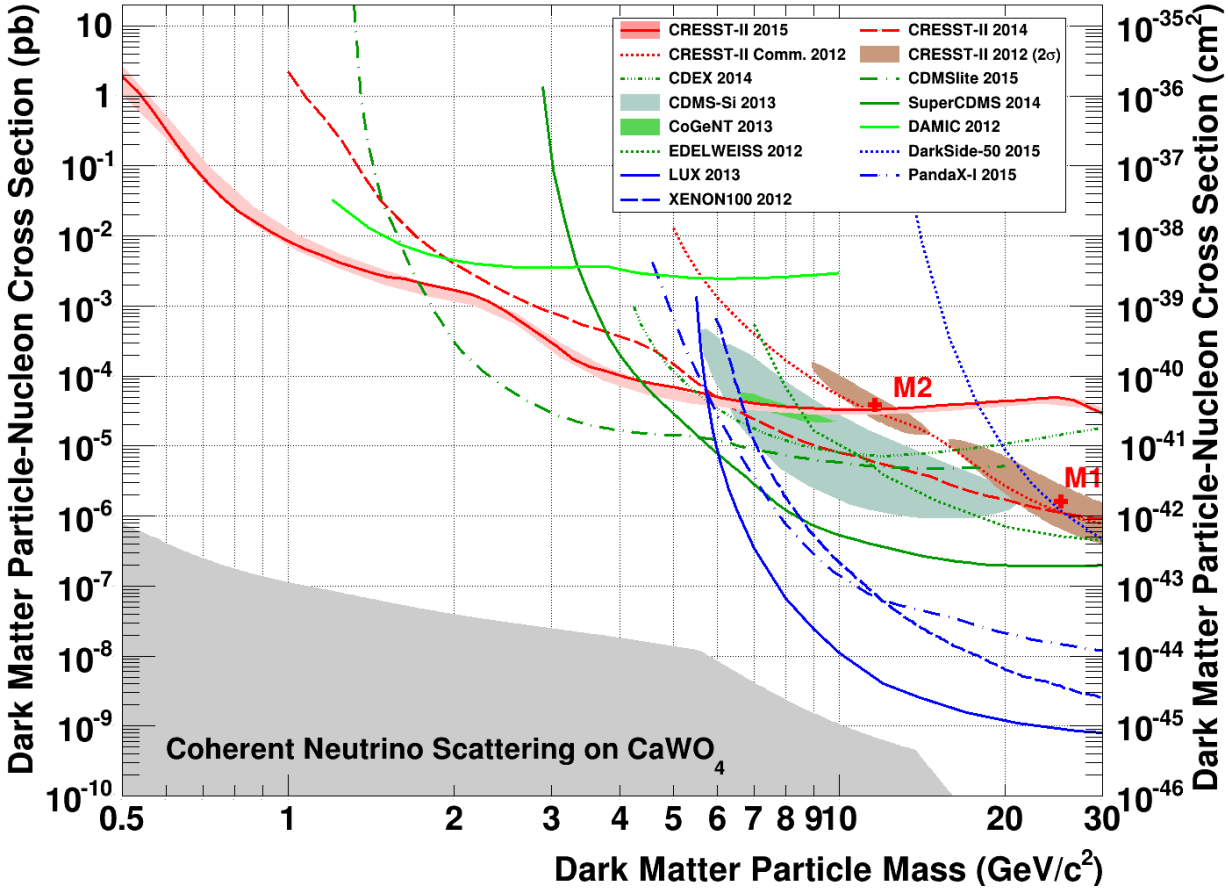

Figure 2.9: Direct dark matter searches landscape at the end of the last CRESST-II measuring campaign. The final CRESST-II result is drawn in solid red. The other two red lines correspond to the previous CRESST-II limits[59][60]. Shaded regions correspond to the favored parameter space reported by CRESST-II phase 1[61], CDMS-Si[62] and CoGeNT[63]. Liquid noble gas limits are depicted in blue (DarkSide-50[64], LUX[65] and Xenon100[66]). Germanium based experiments are drawn in green (CDMSlite[67], SuperCDMS[68], Edelweiss[69] and CDEX[70]) and the Silicon based DAMIC experiment in black[71]. Plot from [58].

Chapter 3

The CRESST-III experiment

The CRESST experiment is a long-established direct dark matter search located at *Laboratori Nazionali del Gran Sasso* in Italy. It makes use of $CaWO_4$ scintillating crystals operated as cryogenic detectors. At its first set-up, whose construction is dated back to 1995, it employed sapphire crystals with no scintillation channel, so that only the deposited energy could be measured. The experiment was upgraded and calcium tungstate scintillating crystals were used. Adding a second channel introduced the possibility to differentiate nuclear recoils from electron recoils induced by β/γ particles which were the main source of background and, thus, improved the sensitivity to dark matter-induced nuclear recoils.

CRESST is now at its third stage and it is optimised for an unprecedented sensitivity to low mass dark matter particles.

This chapter is dedicated to the description of the CRESST installation and the working principle of cryogenic detectors, the basics of the phonon-light technique to suppress the dominating backgrounds, and the current design of the CRESST-III detector modules. In conclusion, certain aspects of the analysis of CRESST data are outlined.

3.1 CRESST Installation in Gran Sasso Underground Laboratories

CRESST (**C**ryogenic **R**are **E**vent **S**earch with **S**uperconducting **T**hermometers) is a low background experiment whose primary goal is to detect Galactic Halo dark matter particles in sensitive detectors. The low background environment is key for direct dark matter searches and its realisation in CRESST consists of both shielding and careful choice of materials. The shielding in particular consists of several parts, each of which is designed against a specific type of radiation. In the following section, a list of the main background components and related shielding is given.

Cosmic rays

The strongest source of particles on the surface of Earth is cosmic radiation. Protons are the main constituent of the primary cosmic radiation interacting in the Earth's atmosphere. As interaction products, pions and kaons are the most abundant particles and their decay produces muons and neutrinos. Due to their relatively long lifetime and low interacting rate, muons make up most of the charged radiation reaching sea level. Their flux is around $1\text{cm}^{-2}\text{min}^{-1}$ at sea level and decreases as muons travel through the crust of the Earth. Deep underground facilities, such as *Laboratori Nazionali del Gran Sasso*, are the standard choice for low background experiments, since they offer a muon-suppressed environment (see Figure 3.1). The muon flux in LNGS, suppressed by 1400m of rock

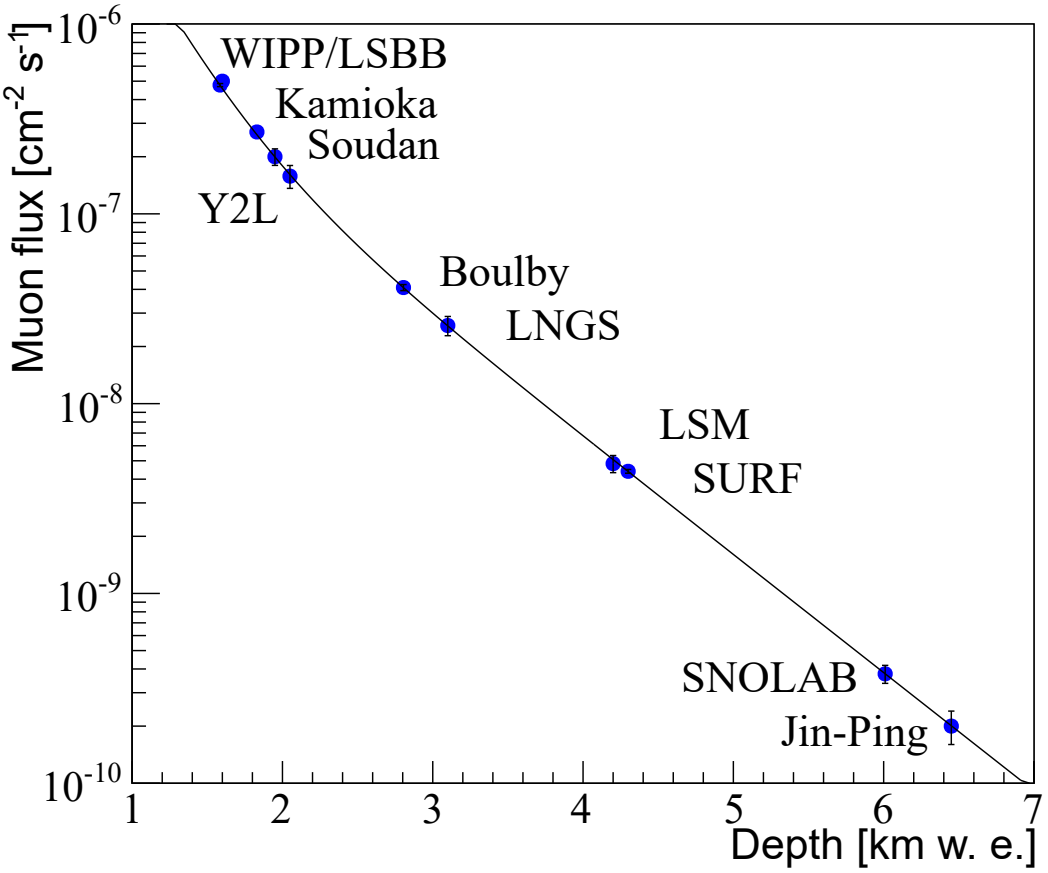

Figure 3.1: Muon flux in some underground laboratories. Picture from [45].

(3800m water-equivalent), was measured by the Borexino experiment over four years and the result is[72] $(3.41 \pm 0.01)\cdot 10^{-4}\text{m}^{-2}\text{s}^{-1}$, corresponding to a suppression of the order 10^{-5}-10^{-6}. Despite the suppression, remaining muons are still of concern. Although they are not directly a background for dark matter search, secondary particles, such as electrons, gammas and neutrons, can be produced in the shielding or in the materials surrounding

the detectors. In order to reject those events, CRESST is equipped with a muon veto (see Figure 3.3), consisting of 20 plastic scintillator panels, each coupled to a PMT. Events in the detectors can be rejected when they happen to be in coincidence with the veto. The coverage offered by the veto is 98.7% of the solid angle seen by the detectors.

Radon

^{222}Rn is an isotope which belongs to the ^{238}U decay chain and is, therefore, naturally present in the rocks of the Gran Sasso laboratories. Its half-life is 3.82 days, enough to be diffused or for the ground waters to wash it out into the environment. Hence, ^{222}Rn is a serious source of background and its decay chain (see Figure 3.2 for details) contains αs, βs, and γs. The γs are produced via bremsstrahlung or other nuclear reactions. The measured

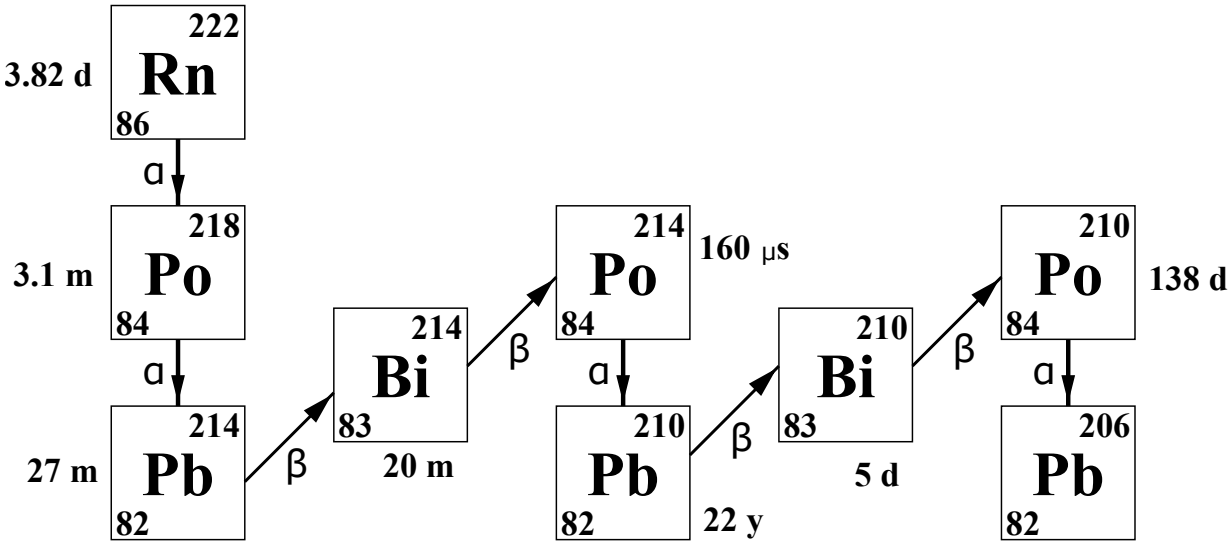

Figure 3.2: Decay chain of ^{222}Rn. The rare decay modes into ^{218}At and ^{210}Tl (branching ratios $\sim$0.02%) are not displayed. Picture from [73].

level of ^{222}Rn in the air of the laboratories is about 50Bq·m^{-3}[74]. To prevent ^{222}Rn from contaminating the experimental set-up, the lead and copper shielding are enclosed by an air-tight box, the **randon box** (Figure 3.3), which is constantly flushed with nitrogen and kept in overpressure. A subtle aspect of Radon is that it sticks to exposed surfaces and its decay products are implanted in radon-exposed surfaces. Hence, in addition to the radon box, all parts directly facing the detectors are etched and stored under nitrogen atmosphere before being installed in the CRESST set-up.

Gammas and electrons

Natural radioactivity is an ubiquitous source of background. Isotopes belonging to the ^{238}U and ^{232}Th decay chains as well as ^{40}K are the principal contaminants in the underground

rocks and in the material constituting the experiment. The α-decay channels, generally speaking, are not troubling as they consist typically of monoenergetic α particles in the MeV range and their penetration length is very short. On the contrary, γs and βs show up at all energies and may be highly penetrating. In [75] a measurement of the γ flux below 3MeV reports an integrated flux of 0.3-0.4 $s^{-1}cm^{-2}$. In order to shield against these particles, 20cm of lead surrounds the experimental volume of CRESST. Lead shielding is particularly effective at suppressing radiation because of its high density and atomic number. The drawback of lead is the presence of the radioisotope ^{210}Pb whose decay eventually ends with the stable ^{206}Pb emitting αs, βs, and γs in the process. An additional layer of 14cm of Cu shielding in placed within the lead to stop ^{210}Pb-originated radiation. The availability of high purity grade copper and its thermal properties make copper the material of choice for this, as well as for the innermost part of the experiment, i.e. the detectors' holding structures.

Neutrons

Neutrons are a dangerous source of background for all direct searches, since their primary interaction mode in matter is elastic scattering on nuclei, potentially mimicking a dark matter interaction. The fast[1] component of the neutron flux in LNGS is $(0.23\pm0.07)\cdot10^{-6}$ cm^{-2} s^{-1}[76]. Neutrons cannot be shielded like β/γ radiation, instead they are moderated so that they are thermalised and can no longer induce a detectable signal in the detectors. Because of kinematics, materials rich in hydrogen are very effective moderators. CRESST has a 40cm-thick polyethylene shield which encloses the lead shield and another, 3.5cm thick, placed in the **OVC** (Outer Vacuum Chamber) of the cryostat.

[1]Only neutrons with sufficient energy to be detected are of concern. Thermal and epithermal neutrons, whose measurements are also in[76], have energies below the eV scale and, therefore, do not pose any threat.

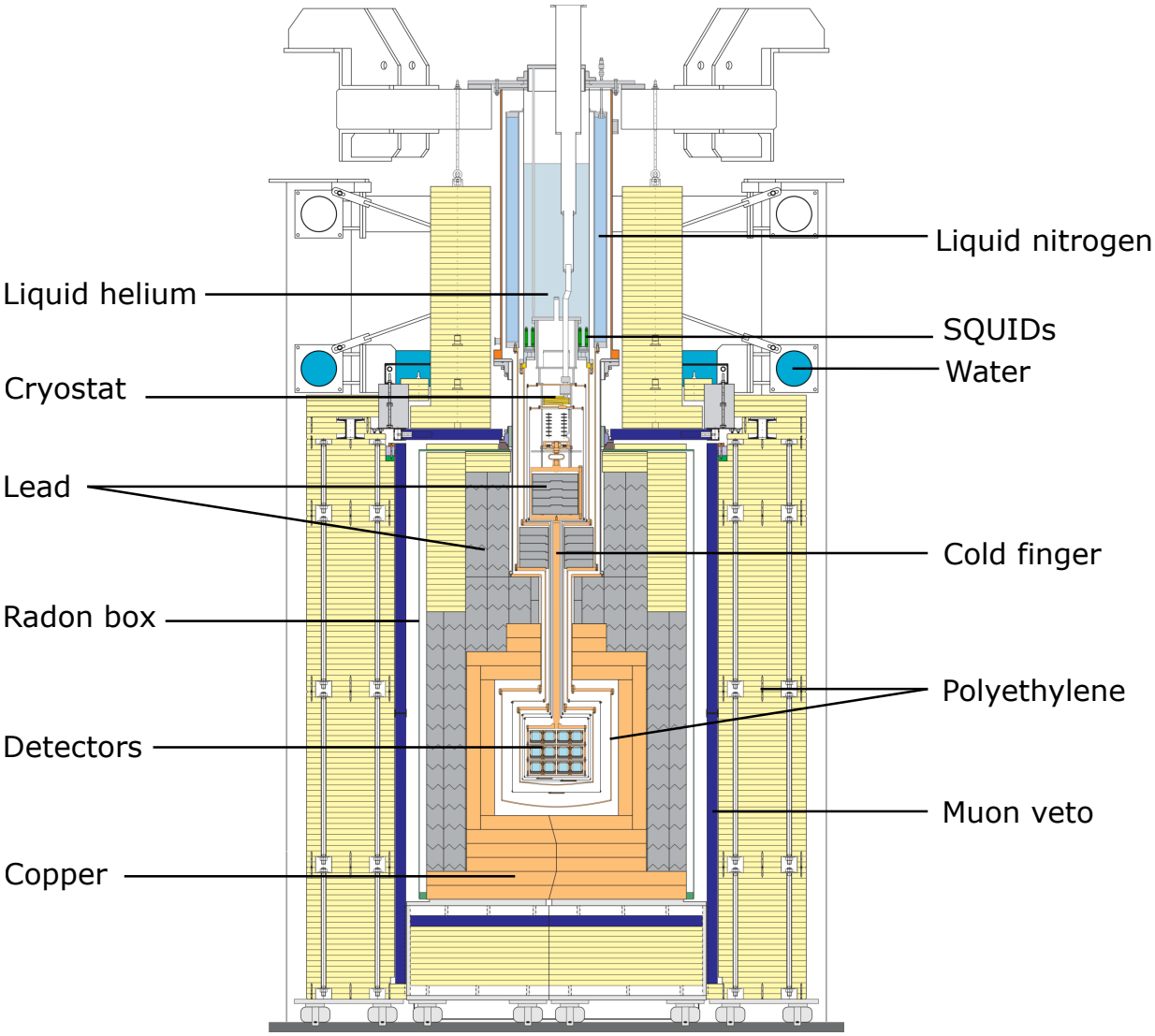

Figure 3.3: Schematics of the cryogenic facility of the CRESST experiment in Gran Sasso. The experimental set-up consists of a dilution refigerator, several shieldings and the detector modules themselves.

Material	Θ_D[K]	reference
$CaWO_4$	350	[77]
Sapphire	1042	[78]
Silicon	636	[79]

Table 3.1: Measured values of the Debye temperature Θ_D for materials used in CRESST as absorbers.

3.2 Cryogenic calorimeters

The heart of the CRESST experiment are the detector modules. They are hosted in the experimental volume of the low-background cryogenic facility presented in the previous section. The current section presents the general idea of cryogenic detectors. Details about TES temperature sensors are explained, as is the phonon-light technique to actively reject the β/γ background, a prominent feature of the CRESST technology.

3.2.1 Basic principles

Cryogenic detectors are, in their simplest form, made of an absorber, a thermometer, and a link to a heat bath. The energy deposited within the sensitive volume (the absorber) is converted into heat that results in temperature rise, which is measured by the thermometer.

Given a deposition of energy ΔE and if C is the heat capacity of the detector, then the temperature rise ΔT reads:

$$\Delta T = \frac{\Delta E}{C} \tag{3.1}$$

We can immediately see why "cryogenic detectors" and "cryogenic calorimeters" are often used interchangeably. From Equation 3.1, the energy ΔE is entirely degraded into heat so that the conversion efficiency from the interesting physical quantity (ΔE) to the observable one (ΔT) is 100%. Though such a statement is not fully verified, it is a very close approximation and we assume it for the moment to be true. A more accurate description will be given later in this chapter.

We observe in Equation 3.1 that C is the only detector-related quantity. In order to maximize the sensitivity of the device, C needs to be as small as possible. Let us consider only ideal crystals, either dielectric or semiconductor, as the absorber. The heat capacity C for the lattice of such materials obeys the Debye law:

$$C = 9Nk_B \left(\frac{T}{\Theta_D}\right)^3 \int_0^{T/\Theta_D} \frac{x^4 e^x}{(e^x - 1)^2} dx \tag{3.2}$$

The quantities in Equation 3.2 are: N as the number of nuclei, k_B as the Bolzmann's constant, and Θ_D as the Debye temperature. These last quantities in material-specific and measured values for some materials of interest in CRESST are given in Table 3.1.

In the limit for $T \ll \Theta_D$ the heat capacity follows the notorious law: $C \propto (T/\Theta_D)^3$.

The T^3 dependence of C is the main reason for the need for cryogenic temperature. CRESST detectors operate at around 15mK.

3.2.2 Transition Edge Sensor (TES)

The temperature rise ΔT needs to be translated into an electric signal in order to be acquired. This operation is performed by a thermometer applied onto the surface of the absorber. The technology developed by the CRESST collaboration makes use of a **TES** (Transition Edge Sensor) whose transition temperature needs to be as low as possible. The temperature of choice is around 15mK, which is convenient for cryogenic operations and offers good sensitivity. Thin W films match such requirements and, therefore, are used as the main constituent for thermometers in CRESST.

An example of the resistance of such a W film as a function of temperature is shown in Figure 3.4. Normal-conducting and super-conducting states are clearly visible and the transition between the two lies in the range [11-12]mK for this specific film. In this region the resistance of the film has a strong dependence on the temperature so that a small temperature rise, typically $\sim 10\mu$K for a 1keV energy deposition, results in a few tens mΩ resistance rise.

From Figure 3.4 it is also clear that the TES behaviour is highly non-linear and a slight variation of the working-point may result in a very different detector's response to the same energy input. Therefore, extremely accurate temperature stabilisation and constant monitoring are a must for reliable data-taking during operation.

3.2.3 Thermal model for pulse formation

Equation 3.2 gives an oversimplified picture of the detector response to energy deposition since it does not account for certain aspects, such as the heat capacity of the thermometer.

An in-depth discussion on signal formation in cryogenic detectors with TES sensors can be found in [80] and in the more recent [81], where the focus is on design optimisation. Here, salient aspects of the thermal model from [80] are discussed.

As a particle deposits energy into the absorber, very high-frequency optical phonons are created and promptly decay (within a few nanoseconds) into acoustical, non-thermal phonons ($\mathcal{O}$(THz)). These phonons have energies in the meV scale and are labelled "non-thermal" because at 10mK thermal phonons of $k_B T \approx 1\mu$eV are expected. The acoustical phonon population is rapidly down-converted into $\mathcal{O}$(100GHz) phonons due to anharmonic decay with a decay rate of $\Gamma_d \propto \nu^5$. The strong dependence on the phonon frequency makes the frequency distribution in the absorber rather constant during the relevant time scale of the detector response (ms). The energy of such phonons corresponds to a $\mathcal{O}$(1K) Planck radiation. Non-thermal phonons ballistically spread in the absorber and fill the volume homogeneously over a time $\sim \mu$s, assuming an absorber of linear dimension of $\mathcal{O}$(cm) and typical phonon velocity of 10^3m/s. At this point we make a simplification in order to characterise the response in the TES, namely we consider the phonon system made

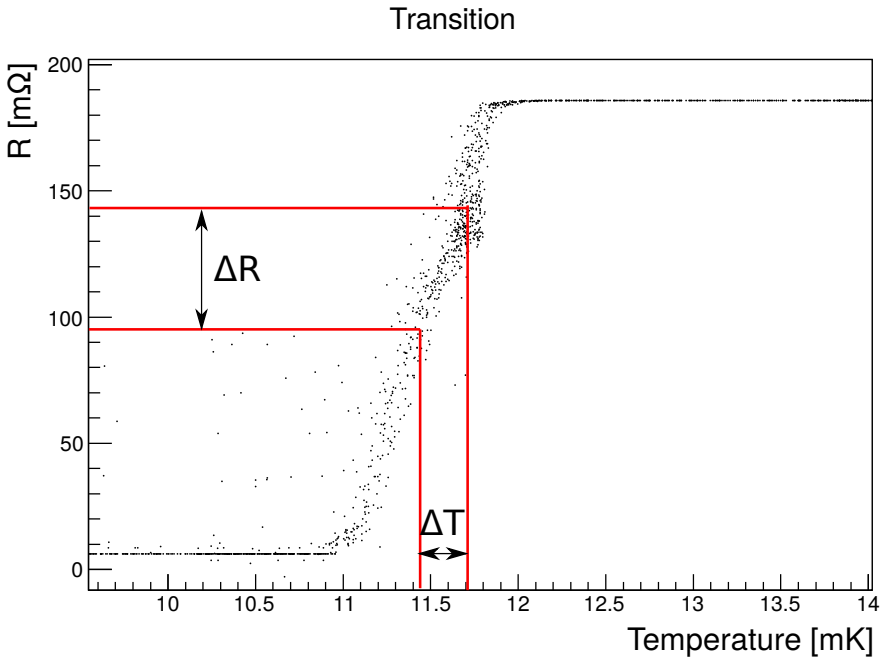

Figure 3.4: Measurement of the resistance value of a thin tungsten film as a function of the temperature. The resistance was measured applying a constant BIAS current through the W film while sweeping the temperature of the film. During operation as cryogenic detector, the film needs to be stabilised very precisely in between the normal-conducting and super-conducting state. The power input due to a particle causes the detector's temperature to rise by ΔT. The measured physical quantity is the corresponding increase ΔR of the W film.

up by two populations: non-thermal and thermal phonons. A schematic of the thermal model is depicted in Figure 3.5.

Non-thermal phonons

As non thermal phonons enter the thermometer, they are efficiently absorbed by the free electrons in the film. Due to the strong interaction among the electrons, the absorbed energy is quickly shared and thermalised. This time-dependent power input in the thermometer due to non-thermal phonons, $P_e(t)$, causes the heating of the electronic system and, as a result, the temperature (T_e in Figure 3.5) rises. Part of the energy escapes into the heat bath via the link G_{eb} and part is radiated back into the absorber under the form of thermal phonons.

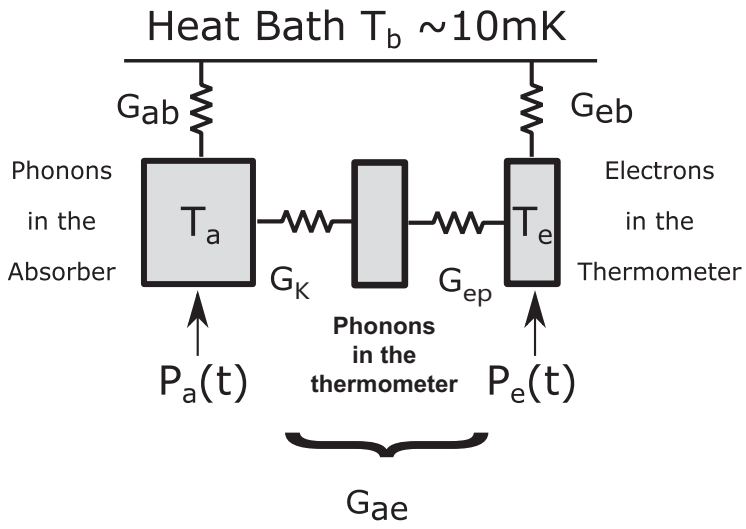

Figure 3.5: Depiction of the thermal model. Because of the efficient absorption, the energy transferred from the non-thermal phonons to the electrons in the TES is modelled as a direct power input in the electronic system. The link G_{eb} provides the heat sink to the bath. G_{ab} is the thermal link between the absorber and the heat bath due to the mechanical mounting. It is in general much weaker than G_{eb}. G_K is the Kapitza coupling between phonons in the absorber and phonons in the thermometer, and G_{ep} is the electron-phonon coupling in the thermometer. The effective coupling of the electrons in the thermometer to the phonons of the absorber is G_{ae}. The thermal phonons are modelled as a power input in the absorber.

Thermal phonons

In the same way as the non-thermal phonons enter the film, so do the thermal phonons. In the case of thermal phonons at very low temperature, the coupling to the electronic system G_{ep} reads:

$$G_{ep} \propto T^5 \tag{3.3}$$

Such dependence strongly suppresses the signal coming from the thermal-phonon power input. This effect, called electron-phonon decoupling, makes the sensor relatively insensitive to the thermal component of the signal generated in the absorber.

Thermal phonons are the final state to which non-thermal phonons decay. The power input due to the thermal component in the absorber, $P_a(t)$, raises the absorber temperature T_a. The coupling to the thermal bath due to mechanical mounting is G_{ab}. The effective coupling of phonons in the crystal and the electron system in the TES is G_{ae}. Being the temperature of the thermometer determined by the thermal phonon population only, ideally one would like the thermalisation process to occur entirely in the thermometer, so that no temperature rise is manifest in the main absorber. Because of real-world effects, mainly surface scattering in the crystal, a thermal phonon population is always present in the main absorber.

Pulse formation

The detector output is the resistance variation of the temperature sensor, which follows the temperature change of the electronic system. According to the model reported in Figure 3.5, we can write two coupled differential equations:

$$\begin{aligned} C_e\frac{dT_e}{dt} + (T_e - T_a)G_{ea} + (T_e - T_b)G_{eb} &= P_e(t) \\ C_a\frac{dT_a}{dt} + (T_a - T_e)G_{ea} + (T_a - T_b)G_{ab} &= P_a(t) \end{aligned} \tag{3.4}$$

where C_e and C_a are the electrons heat capacity and the absorber heat capacity respectively. In order to solve the paired equations 3.4 we need an expression for the two power inputs $P_e(t)$ and $P_a(t)$. Making use of the above assumptions, we model the interaction as a sudden energy release ΔE with uniform distribution of non-thermal phonons in the absorber and the power input $P_e(t)$ as the power of the non-thermal phonon population only:

$$\begin{aligned} P_e(t) &= \Theta(t)P_0 e^{-\frac{t}{\tau_n}} \\ P_a(t) &= \frac{1-\varepsilon}{\varepsilon}P_e(t) \\ P_0 &= \varepsilon\frac{\Delta E}{\tau_n} \end{aligned} \tag{3.5}$$

where ε is the fraction of non-thermal phonons thermalised in the thermometer, 1-ε is the one of those thermalised in the absorber, and τ_n is the thermalisation constant. The assumption of a uniform distribution of the non-thermal phonons in the volume of the absorber is here encoded by the step function $\Theta(t)$ (we neglect the initial randomisation).

We consider the thermalisation process as the effect of two competing processes: the thermalisation in the film and the one in the crystal. We can then write τ_n as:

$$\tau_n = \left(\frac{1}{\tau_{film}} + \frac{1}{\tau_{crystal}}\right)^{-1} \tag{3.6}$$

where τ_{film} and $\tau_{crystal}$ are the thermalisation time constants of the two individual processes. The former is determined by the geometry of the film and the phonon propagation properties across the interface with the crystal, the latter by the lattice properties and the geometry of the absorber. The ε term can now be expressed as:

$$\varepsilon = \frac{\tau_{crystal}}{\tau_{film} + \tau_{crystal}} \tag{3.7}$$

Thanks to Equation 3.7, the resulting $P_e(t)$ comes under the form of a simple exponential. The solution to the paired equations 3.4, $\Delta T_e(t) \equiv T_e(t) - T_b$, is:

$$\Delta T_e(t) = \Theta(t)\left[A_n(e^{-t/\tau_n} - e^{-t/\tau_{in}}) + A_t(e^{-t/\tau_t} - e^{-t/\tau_n})\right] \tag{3.8}$$

with the following definitions of the time constants:

$$\begin{aligned} \tau_{in} &= \frac{1}{s_{in}} = \frac{2}{a+\sqrt{a^2-4b}} & \tau_t &= \frac{1}{s_t} = \frac{2}{a-\sqrt{a^2-4b}} \\ a &= \frac{G_{ea}+G_{eb}}{C_e} + \frac{G_{ea}+G_{ab}}{C_a} & b &= \frac{G_{ea}G_{eb}+G_{ea}G_{ab}+G_{eb}G_{ab}}{C_eC_a} \end{aligned} \tag{3.9}$$

These quantities are the time constants of the homogeneous equations and have the following physical interpretation:

- τ_{in}: intrinsic thermal relaxation time of the film.
- τ_n: life-time of the non-thermal phonons.
- τ_t: thermal relaxation time of the crystal.

The amplitudes are:

$$\begin{aligned} A_n &= \frac{P_0(s_{in}-(G_{ab}/C_a))}{\varepsilon(s_{in}-s_t)(s_{in}-s_n)}\left(\frac{s_t-(G_{ab}/C_a)}{G_{eb}-(C_e/C_a)G_{ab}}-\frac{\varepsilon}{C_e}\right) \\ A_t &= \frac{P_0(s_t-(G_{ab}/C_a))}{\varepsilon(s_t-s_{in})(s_t-s_n)}\left(\frac{s_{in}-(G_{ab}/C_a)}{G_{eb}-(C_e/C_a)G_{ab}}-\frac{\varepsilon}{C_e}\right) \end{aligned} \tag{3.10}$$

The solution in Equation 3.8 comes as the sum of two signals with amplitudes A_n and A_t. These two signals correspond to the (slow) thermal and (fast) non-thermal power input in the thermometer. The former is due to the temperature rise of the absorber T_a, the latter is the signal from the thermalisation of non-thermal phonons in the electronic system of the TES.

The design of the temperature sensor is optimised in order to have the largest possible amplitude for the non-thermal signal A_n. Depending on the relative ratio of τ_n and τ_{in}, two operating modes are possible for the CRESST detectors, namely the bolometric and calorimetric modes.

Calorimetric mode

In the case of $\tau_{in} \gg \tau_n$, the thermometer collects the non-thermal phonons and integrates the signal over time τ_{in}. The resulting signal amplitude is:

$$A_n \approx -\varepsilon\frac{\Delta E}{C_e} \tag{3.11}$$

In this regime, A_n being negative, the rise-time of the signal is the life-time of the power input, i.e. τ_n, and the decay-time of the non-thermal component is τ_{in} (see Equation 3.8).

Bolometric mode

For a detector where $\tau_{in} \ll \tau_n$, the thermal relaxation of the film is much faster than the lifetime of the non-thermal phonons. The amplitude of the signal is then given by the energy flux through the thermometer, whose duration is given by τ_n. From Equation 3.10 we get:

$$A_n \approx \frac{P_0}{G_{eb}} = \varepsilon \frac{\Delta E}{\tau_n G_{eb}} \tag{3.12}$$

This time A_n is positive. Thanks to Equation 3.8 we can then identify the rise-time of the signal with τ_{in} and the decay-time of the non-thermal component with τ_n. The bolometric mode was not adopted[2] in CRESST-III and it is reported here for the sake of completeness.

3.3 CRESST-III Detectors

In the third stage of the CRESST experiment, ten detector modules with identical design, named A to J, were installed and operated in the installation in Gran Sasso. Based on the results of CRESST-II, the new modules were redesigned to achieve an energy threshold of the phonon channel of about 100eV. The main modification was the mass of the absorber. From the $\mathcal{O}$(200g) mass of the absorbers in CRESST-II, the new crystals are downsized to a mass of 24g.

3.3.1 Temperature sensor realisation

The structure of a thermometer of a CRESST detector consists of a thin W film that functions as described above. In addition to that, two Al films are deposited to allow for a proper bonding of the wires needed to apply a bias current through the W film. These Al films, the bondpads, serve an additional purpose: they can enhance the signal amplitude since they act as a phonon-collecting surface. In [82] a detailed study on the effect of such structure in the signal formation can be found.

The thermal link G_{eb} is realised with a thin Au stripe directly structured on the W film and thermally linked to the heat bath via an Au bond-wire. Depending on whether a bolometric or calorimetric TES is desired, different designs are possible. In Figure 3.6 the schematics of two thermometers for the two operations are shown. Figure 3.7 shows the surface scan of a calorimetric sensor, obtained with an alpha step profilometer.

[2]The calorimetric mode offers, in general, a higher sensitivity compared to the bolometric one. Since the threshold was set as the crucial parameter to improve, the calorimetric mode was the choice for the new stage. However, the calorimetric mode suffers from the disadvantage of slow signals. In the case of CRESST-II, phonon detectors of the calorimetric type would have posed operational issues due to the excessively slow signals.

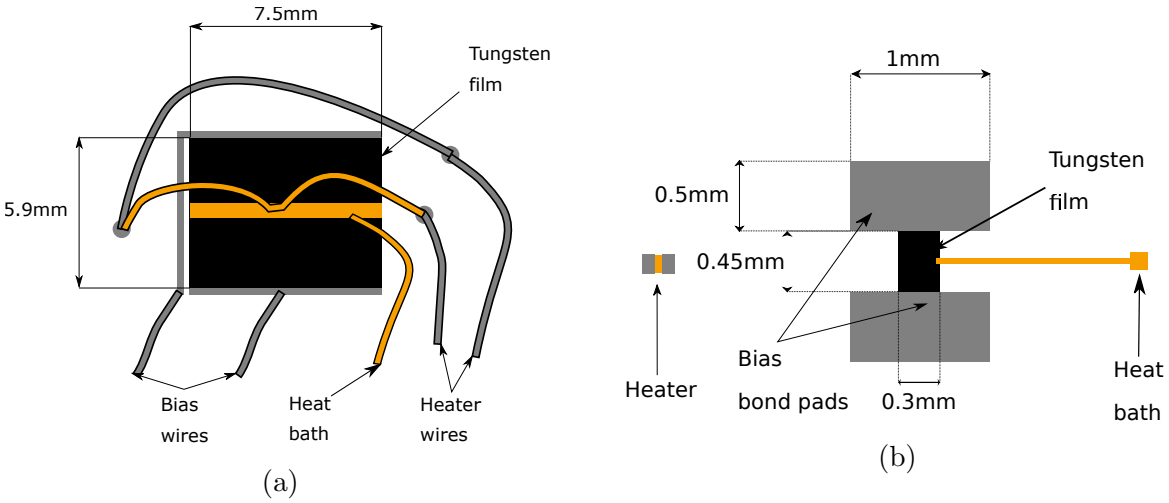

Figure 3.6: Two (out of many) TES designs used in the CRESST experiment. (a) The design is optimised for large crystals $CaWO_4$($\sim$ 200g) with cuboid or cylindrical shapes operated in bolometric regime. The relatively large surface of the tungsten film is meant to enhance the collection of the non-thermal phonons so they are efficiently thermalised in the film. The Au strip extending for the whole dimension of the thermometer realises $\tau_{in} \ll \tau_n$. (b) The design is optimised for detectors with a planar geometry (typically 40mm in diameter and 460μm in thickness) operated in calorimetric mode. The calorimetric condition $\tau_{in} \gg \tau_n$ is guaranteed by the weak thermal link provided by the small overlap of the W film with the Au stripe.

3.3.2 Phonon-Light Technique

The stringent requirements regarding the low background environment are addressed by the CRESST experiment with massive shielding as outlined in Section 3.1. Despite all efforts to suppress the external radioactivity, there is an irreducible background from contaminants in the detectors themselves and the materials directly facing them.

Active background discrimination is a powerful tool to suppress this unavoidable background. The solution developed in CRESST-III makes use of a three-channels read-out.

One channel is dedicated to the precise measurement of the deposited energy in the absorber. We call this channel **phonon channel** and the relative absorber the **main absorber**. The second channel serves to measure the scintillation light emitted by the particle interaction in the main absorber. This channel is called **light channel** and the combination of its absorber and thermometer is the **light detector**.

The third channel is somewhat special. It is meant to veto holder-induced events and it is referred to as the **iStick** channel.

A CRESST-III detector module consists of a scintillating $CaWO_4$ main absorber of cuboid shape. The main absorber is equipped with a TES designed to operate in the calorimetric regime, directly structured on the surface of the crystal. A light detector,

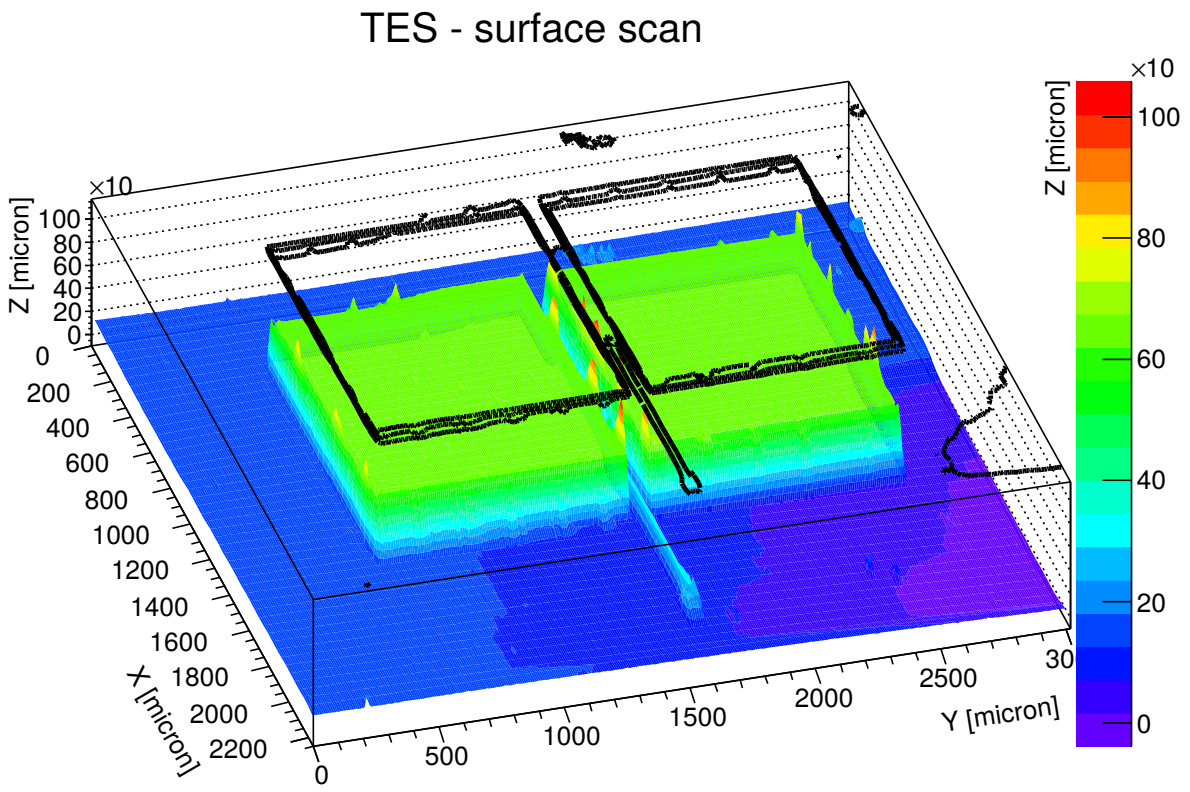

Figure 3.7: Surface scan of a TES of the type in Figure 3.6b obtained with an alpha step profilometer. The thickest parts are the two Al phonon collectors. The Au stripe is sticking out from the two phonon collectors, while the W film is hidden in-between them. The contours of the geometry are drawn on top.

also designed to operate in calorimetric mode, is placed facing the main absorber. These two detectors are kept in place by $CaWO_4$ scintillating sticks and hosted in a copper holder. The sticks holding the main absorber are instrumented with TES sensors. The instrumentation of the holding sticks allows to reject events not occurring in the main absorber but transmitted to it because of the mechanical mounting. The output of the instrumented sticks is the iStick channel. In Figure 3.8 a sketch of a CRESST-III module is shown, Figure 3.9 shows a photo of an (open) detector module and the scintillation of $CaWO_4$ exposed to UV light. We show the output of one detector module to a particle-induced event in Figure 3.10.

Quenching in the light channel

In a CRESST-III detector module, energy deposition due to particle interaction causes a temperature rise in the main absorber and the simultaneous emission of scintillation light. The emitted light induces a signal in the light channel which is then in time coincidence

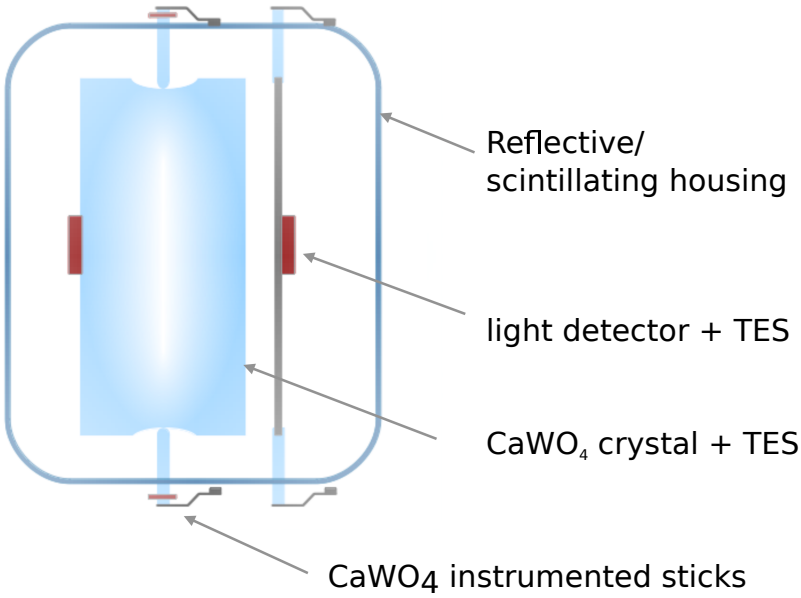

Figure 3.8: Drawing of a CRESST-III detector module. The main absorber is held in position by instrumented $CaWO_4$ sticks, pressed from the outside of the housing. A light detector is faced to the main absorber and clamped by (non-instrumented) sticks. Everything is enclosed in a reflective and scintillating housing. The design is such that every surface exposed to the main absorber is scintillating. Thanks to the instrumented sticks, the holding parts in contact with the crystal can be operated as a veto.

with the signal in the phonon channel. The two signals, together with the iStick output, are recorded as one event. For a defined amount of deposited energy in the main absorber, the amount of emitted scintillation light depends on the type of interaction occurring in the crystal. This is the basic principle upon which the active background rejection in CRESST-III is based.

Figure 3.11 shows light channel vs. phonon channel scatter plots for events recorded by a CRESST detector module exposed to two different radioactive sources. The plot in Figure 3.11a refers to the exposure to a ^{57}Co γ source, the one in Figure 3.11b to an AmBe neutron source. Two distinct classes of events emerge from the plots. In the case of Figure 3.11a mainly γ-induced events populate the plot. Figure 3.11b shows two different populations. The one in the upper part has a light output identical to the one in Figure 3.11a and a second one is present in the lower part with a lower light output. This second class of events is induced by nuclear recoils caused by neutron scattering in the target crystal.

The different light outputs are due to the different interactions in the main absorber. Little ionising radiation, such as electrons or γs, can travel through the target crystal for a relatively long path before their energy is completely released, recoiling mainly on

(a)

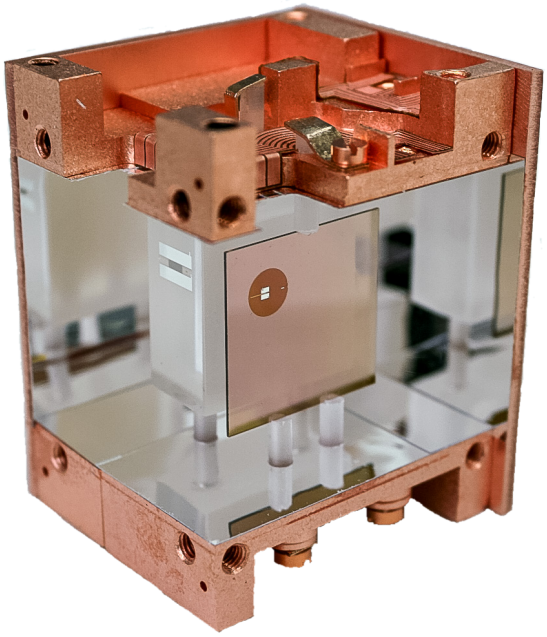

(b)

Figure 3.9: $CaWO_4$ crystals exposed to UV light (a). The surfaces of the two crystals have been treated differently. The surface of the left crystal (facing the camera) is polished, whereas the one of the right crystal is roughened. It is clearly visible that sharp edges and roughened surfaces are favoured escape routes for the scintillation light. In (b) a photograph of an open detector module is shown.

electrons. On the contrary, neutrons interact mainly via single scattering on nuclei so that only a single nucleus is hit and receives all the energy transferred by the incident neutron. The first interaction mode is more efficient than the second in converting the deposited energy into scintillation light. Hence, the light output corresponding to a certain deposited energy via scattering off nuclei is reduced compared to the same energy deposition caused by a e/γ (and α) particles. A detailed study of scintillation properties of materials of interest for cryogenic dark matter search can be found in [83].

The Light Yield vs Energy plot

CRESST data are usually presented in Light Yield vs. Energy plot. If E_l is the energy measured by the light channel and E_p the one measured by the phonon channel, the light yield LY is defined as:

$$LY = \frac{E_l}{E_p} \tag{3.13}$$

E_l and E_p are calibrated using known γ lines, so that events induced by a e/γ interaction have a unitary LY. The LY vs. Energy plot has a clear horizontal bands structure,

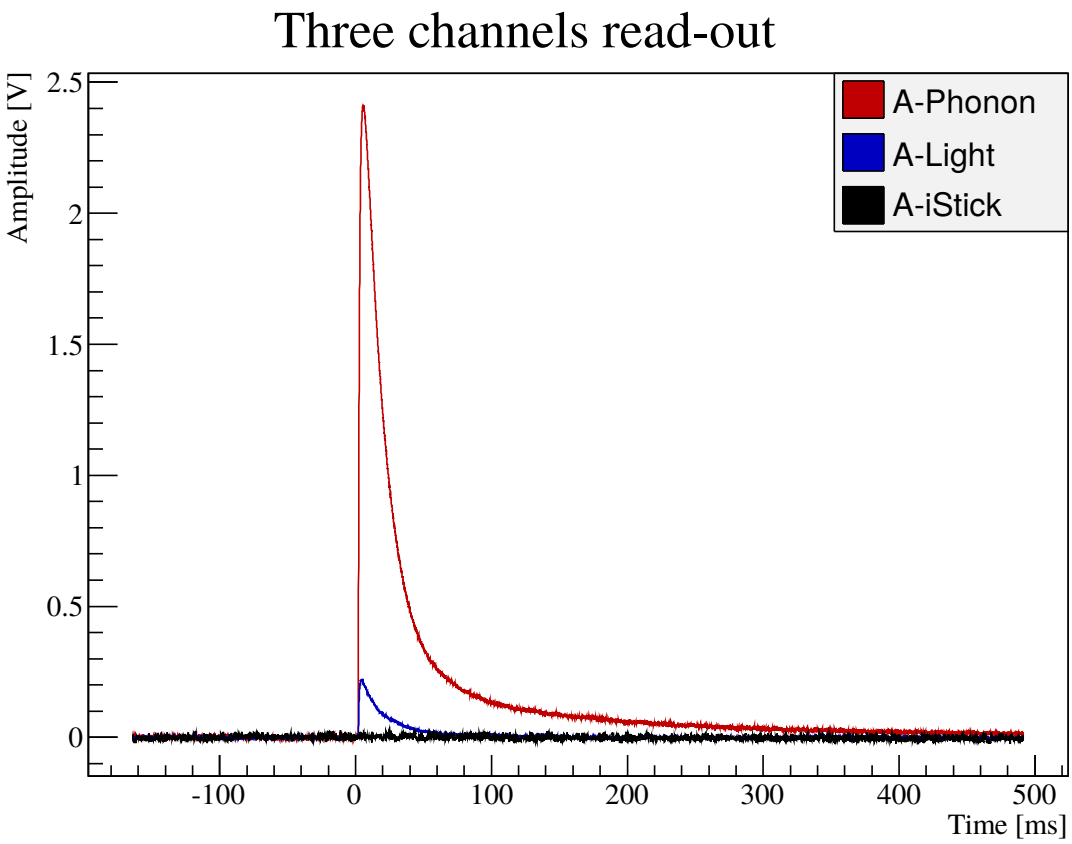

Figure 3.10: CRESST-III detector's output to a particle interaction occurred in the main absorber. In red is the signal recorded from the phonon channel, in blue the one from the light detector and in black the iStick channel. The absence of signal in the iStick channel proves the occurrence of the interaction in the main aborber. The ratio of the two signal amplitudes of the light and phonon channel is, after calibration, the Light Yield of the event.

where each band identifies a different class of events (Figure 3.12). To some extent it is even possible to discriminate which nuclear species recoiled in case of nuclear scattering. In this units the LY is the relative light output suppression with respect to an electron equivalent interaction, also called the **Quenching Factor**. The more general definition of the quenching factor for a nuclear species x is:

$$QF_x(E_r) = \frac{LY_x(E_r)}{LY_\gamma} \tag{3.14}$$

where LY_γ is the average Light Yield of the e/γ band. Because of a slight energy dependence, we conventionally set for $LY_\gamma(122\text{keV}) = 1$ and, consequently, LY_γ may deviate from unity for energies different than the calibration point at 122keV. An energy-dependent measurement of the quenching factors in $CaWO_4$ at mK temperature

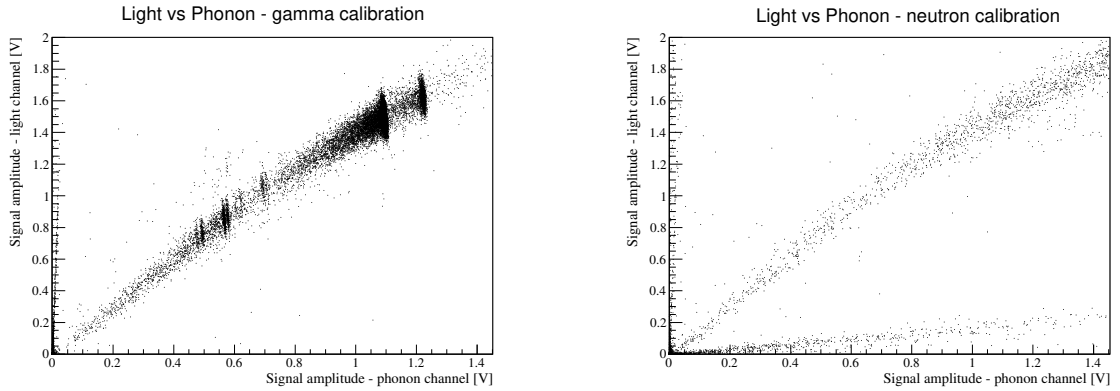

(a) (b)

Figure 3.11: Different behaviour of the light output due to e/γ events and neutron events. (a) Light signal vs phonon signal in presence of a γ source (^{57}Co). The two most densely populated structures are the 122keV and 136keV γ peaks. (b) Light signal vs phonon signal in presence of a neutron source (AmBe). Both the e/γ and the nuclear recoil band are populated. That is because the neutron source emits γ as well. It is clear that for the same signal in the phonon channel, the light output is enhanced for e/γ events compared to the nuclear recoils.

LY band	QF
e/γ (122keV)	1
O recoil	0.112±0.005
Ca recoil	0.0594±0.0049
W recoil	0.0172±0.0021

Table 3.2: Measured quenching factors from the operation of CRESST detectors. The reported values are averaged over 8 detectors. Data from[84].

was carried out irradiating CRESST detectors with fast neutrons created by a particle accelerator[84]. The values for the three nuclei of interest, in the energy range 10-40keV, are reported in Table 3.2.

Surface background

The Light-Yield vs. Energy plot is a very effective tool to identify nuclear recoil events and reject backgrounds. Nonetheless, it is ineffective when the background has the same signature (i.e. nuclear recoils) of a possible signal.

A particularly dangerous background comes from the decay of ^{210}Po, a daughter nucleus of the ^{222}Rn introduced at the beginning of this chapter. The decay is the following:

$$^{210}\text{Po} \rightarrow^{206} \text{Pb}(103\text{keV}) + \alpha(5.3\text{MeV}) \tag{3.15}$$

The decay by itself poses no threat, since both the decay products have energies above

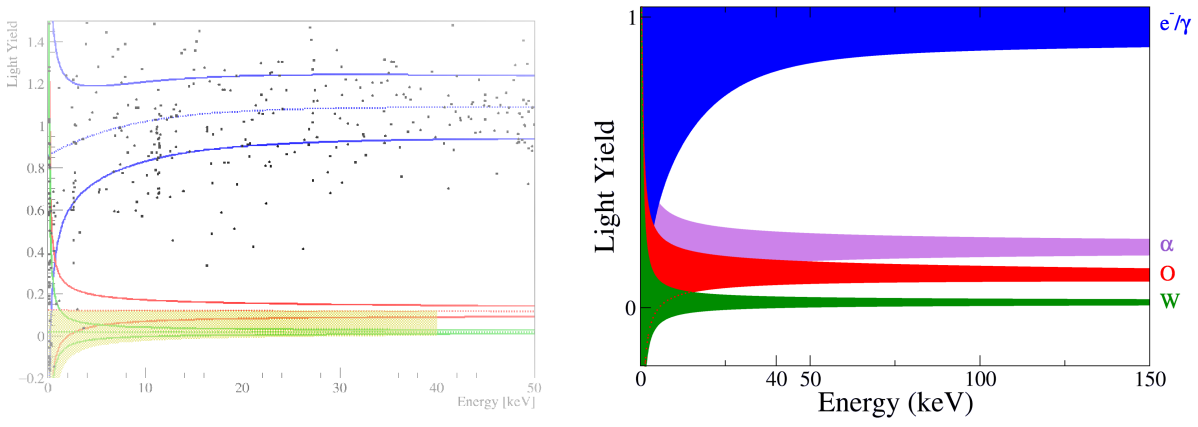

(a) (b)

Figure 3.12: The Light Yield vs Energy plot. (a) Plot of background data corresponding to a raw exposure of 2.39kg·day. Picture from [85]. (b) Schematic depiction of the band structure of the LY vs energy plot.

the region of interest (see Figure 3.12). The complication arises in case such decay occurs slightly below the surface of the material facing the main absorber. Such a situation is illustrated in Figure 3.13. The α particle as well as the lead nucleus can lose part of their energy escaping form the surface, so they can leak in the region of interest of the Light-Yield plot. The α particle can imping in the detector with a low energy such that its light yield overlaps with the nuclear recoil bands (see Figure 3.12b). The recoiling lead is even more dangerous since it is heavier than tungsten and, thus, its quenching factor causes it to fully leak in the recoil band. Despite all the precautions to prevent exposure

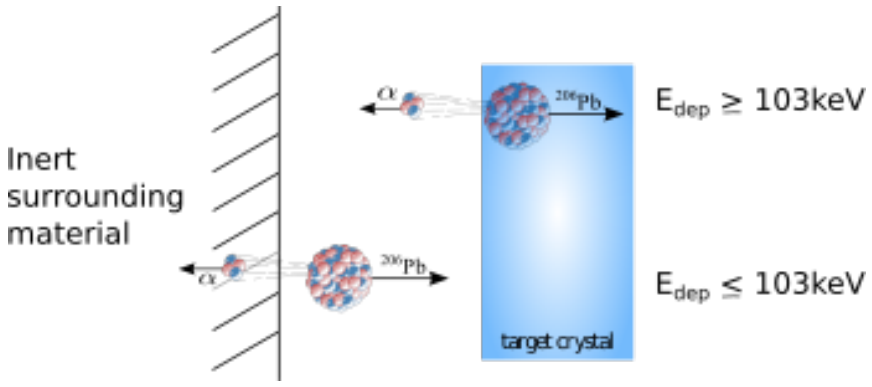

Figure 3.13: Representation of the issue arising from surface ^{210}Po contamination. The possibility for the otherwise high energy α to lose energy in the vicinity of a surface may lead to a signal in the recoil region. A worse scenario is when the α is undetected and the ^{206}Pb nucleus interacts via nuclear scattering in the crystal.

to ^{222}Rn contamination, an absolute absence of ^{210}Po cannot be guaranteed.

In order to overcome the problem, the main absorber is surrounded by a reflective and scintillating polymeric foil (Figure 3.8). The purpose is to tag this class of events with its scintillation light.

3.3.3 Detector read-out

The typical resistance of the normal conducting state of TES used in CRESST is $\mathcal{O}(100\text{m}\Omega)$. When operated as temperature sensor, the working point is usually[3] set such that the TES resistance is around half of the normal conducting state resistance. In order

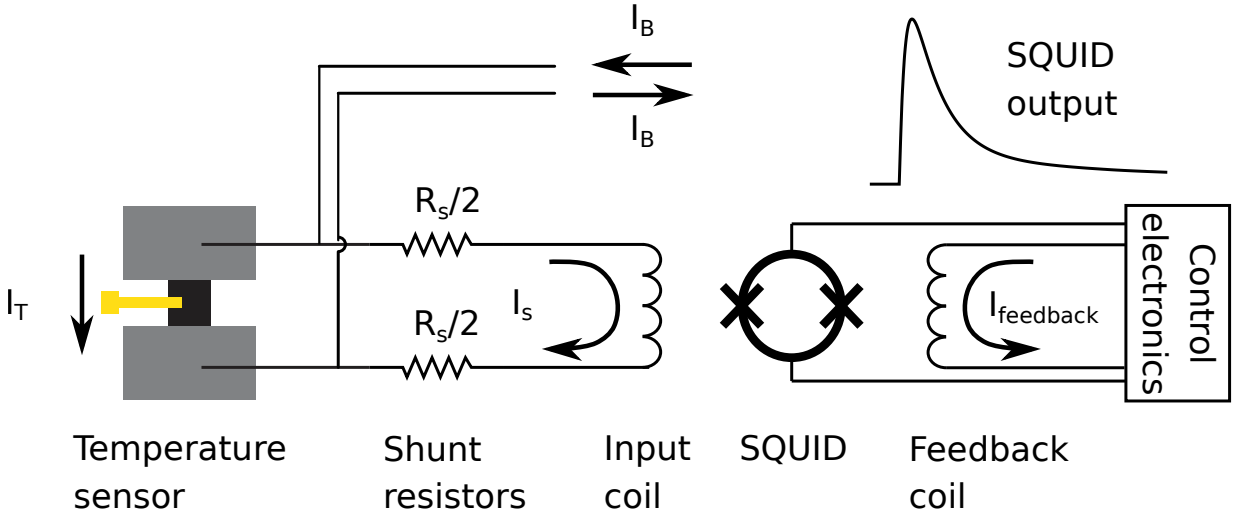

Figure 3.14: Read-out scheme for the temperature sensors in CRESST. The parallel shunt resistor R_s consists of two resistors of resistance $R_s/2$ placed to realise a differential measurement of the splitting current. The SQUID sensor is inductively coupled to the shunt branch of the bias circuit and to a control electronics. The control electronics produces a feedback signal which nullifies the one coming from the input coil.

to detect resistance variations of mΩ, CRESST adopted a DC SQUID-based read-out.

Bias scheme

SQUIDs (Superconducting Quantum Interference Devices) are extremely sensitive magnetometers. Their use in CRESST is illustrated in Figure 3.14.

The TES is placed in parallel to a shunt resistor R_S and the circuit is biased with a DC current I_B. I_B splits in the two branches according to:

$$\begin{aligned} R_T I_T &= R_S I_S \\ I_B &= I_S + I_T \end{aligned} \tag{3.16}$$

[3]The working point is determined via accurate optimisation of several parameters. Such optimisation is carried out for each sensor individually.

The R_S branch of the circuit is in series with an inductor, the input coil. Resistance variations of the TES cause the I_S current to change. Consequently, a change of the magnetic field in the input coil occurs and is measured by the SQUID.

The change of the current in the input coil δI_S caused by a small temperature variation δT is then:

$$\delta I_S = \frac{I_B}{(R_S + R_T)^2} R_S m \delta T \tag{3.17}$$

where m is the slope of the transition at the working point.

SQUID operation

A DC SQUID is a superconducting ring with two Josephson junctions placed in parallel. The voltage drop V across the two junctions is a function of the applied magnetic field Φ and it reads:

$$V = \frac{R}{2}\sqrt{I^2 - [2I_0 \cos(\pi\Phi/\Phi_0)]^2} \tag{3.18}$$

Details of Equation 3.18 are well beyond the scope of this thesis work and will not be covered. The interested reader can find a derivation and description of it in [86].

The important aspect of Equation 3.18 is its non-linearity and periodicity as a function of the chained magnetic flux $\Phi \propto I_S$. If δI_S is directly proportional to the temperature rise and, thus, to the deposited energy, it is convenient[4] to linearise the SQUID output.

The linearisation is based on the so-called "flux-locked loop". In such an operation mode, the SQUID is coupled to a second coil, the feedback coil (see Figure 3.14). The control electronics injects a small AC modulation signal in the SQUID loop. The resulting modulation voltage across the SQUID is used to produce a feedback flux in order to keep the magnetic flux in the loop constant. The current $I_{feedback}$ generated to compensate for variations of the magnetic flux in the SQUID loop is passed through a resistor. The voltage drop across this resistor is the actual signal output from the SQUID electronics.

The SQUID output is monitored by a hardware trigger which outputs a logical signal whenever the amplitude exceeds a given threshold, signalling the occurrence of an event in the detector. The trigger signal is used to digitise a finite data window of the SQUID output, as in Figure 3.10.

3.3.4 Temperature control

The TES response is non-linear and very dependent on the temperature (see Figure 3.4). Hence, as already mentioned, a very accurate and stable temperature during operation is fundamental for a reliable operation of CRESST detectors.

[4]This convenience is not limited to the linear response. The periodicity limits the dynamic range of the squid to one Φ_0.

Control pulses

Every sensor operated in CRESST is equipped with a dedicated resistor, the heater. This device is used to externally increase the TES temperature via Joule heating. In order to determine the working point, at a given time, an artificial pulse is injected by means of the heater. Such pulse, the **control pulse**, is large enough to drive the TES out of transition. An illustration of the principle is shown in Figure 3.15. Because of the plateau at the top of the transition, visible in the saturation of the pulse in Figure 3.15b, the evaluation of the signal excursion is an accurate determination of the current working point. The temperature stabilisation is realised implementing a PID (proportional-integral-derivative) control loop whose feedback is injected as a DC current in the heater. Upper fluctuations of the working point are compensated reducing the DC heating current and, conversely, lower fluctuations are corrected increasing the dissipated power in the detector.

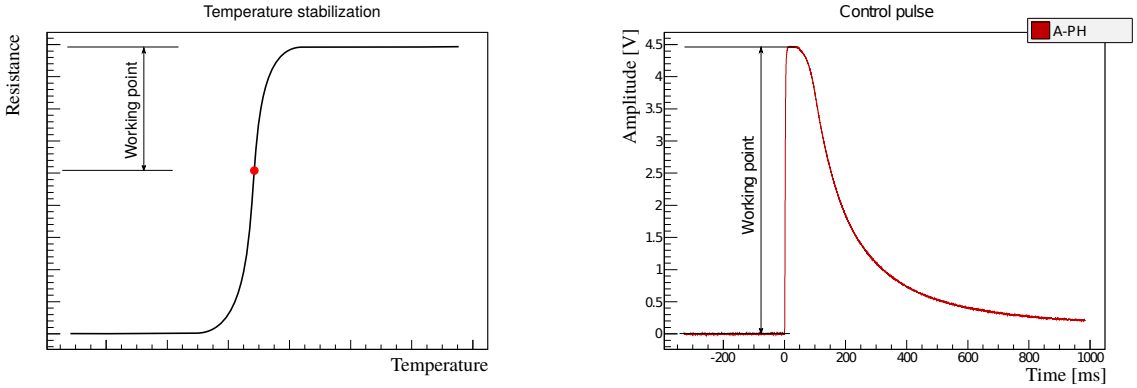

(a) (b)

Figure 3.15: Principle of temperature control. (b) A large pulse is injected in the heater device. (a) Because of the flatness of transition in the normal conducting state, the working point can be evaluated with high accuracy.

Test pulses

The non-linearity of the transition affects the detector response over almost its full dynamic range, depending on the specific shape of the transition. In addition, despite the on-line temperature control, small fluctuations are still present. Therefore, the detector response can be time-dependent.

Both aspects can be accounted for by means of **test pulses**. Like control pulses, they are artificially injected driving a current signal through the heater. In this case, their amplitude is not fixed to drive the TES to saturation. Instead, they are of several amplitudes and are meant to sample the detector response at different energies and over time. Their simple use to linearise the detector response will be shown in Chapter 4. Their use for the time-dependent linearisation is explained in detail in [87]. The specific application to the CRESST-III data analysis is reported in [88].

In Figure 3.16, the detector response to artificially injected heater pulses for the phonon channel of detector A is shown. The several injected amplitudes clearly show the effect of the online temperature control as they are in a comb-like pattern, meaning that the detector response is constant[5] over time. The large amount of different amplitudes present at the lowest pulse amplitudes is meant for a fine sampling of the detector response in the low energy region. The full acquisition setup used to operate the cryogenic detectors of

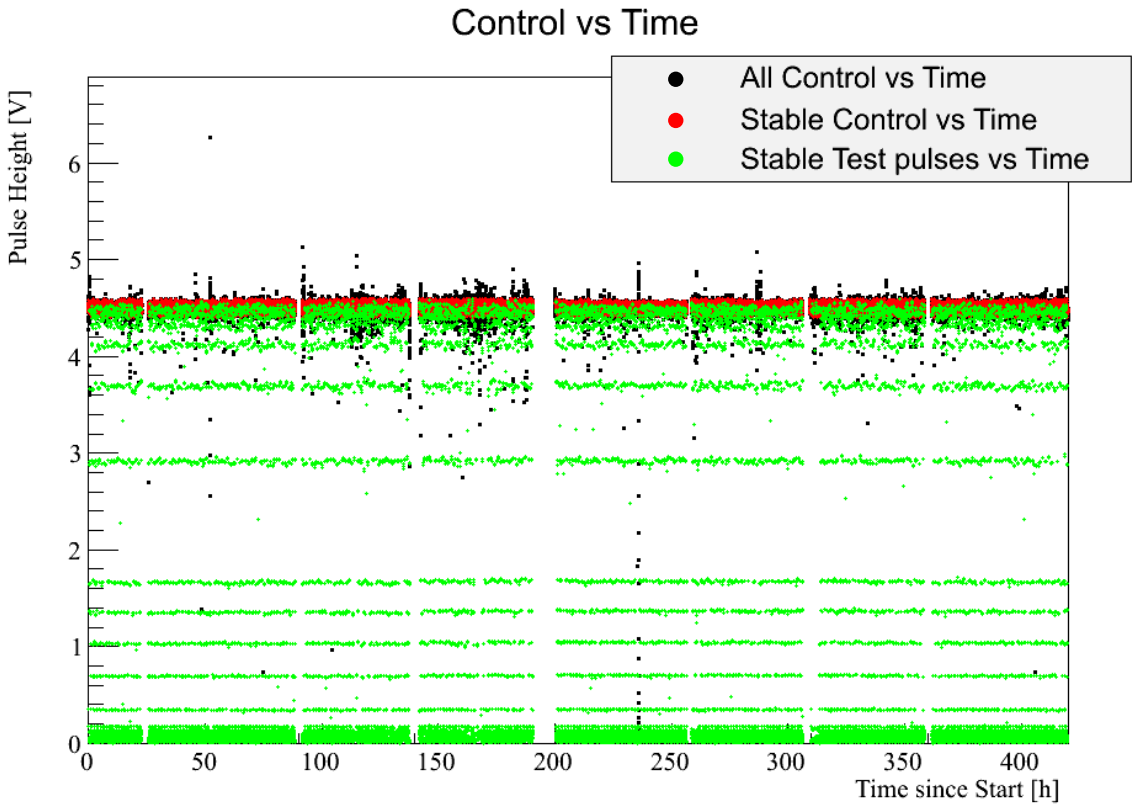

Figure 3.16: Detector response to heater pulses in ∼400h of data-taking of CRESST-III. Color-coded in black are the control pulses delivered during operation. In red are marked control pulses referring to stable periods. The working point is set such that the control pulses have an amplitude of 4.5V. The stability condition requires control pulses to deviate no more than 0.2V from the set working point. The green shows the test pulses delivered during stable periods of operation.

the CRESST-III experiment in shown in Figure 3.17.

[5]The (small) time dependence of the detector response becomes evident with an accurate resolution evaluation.

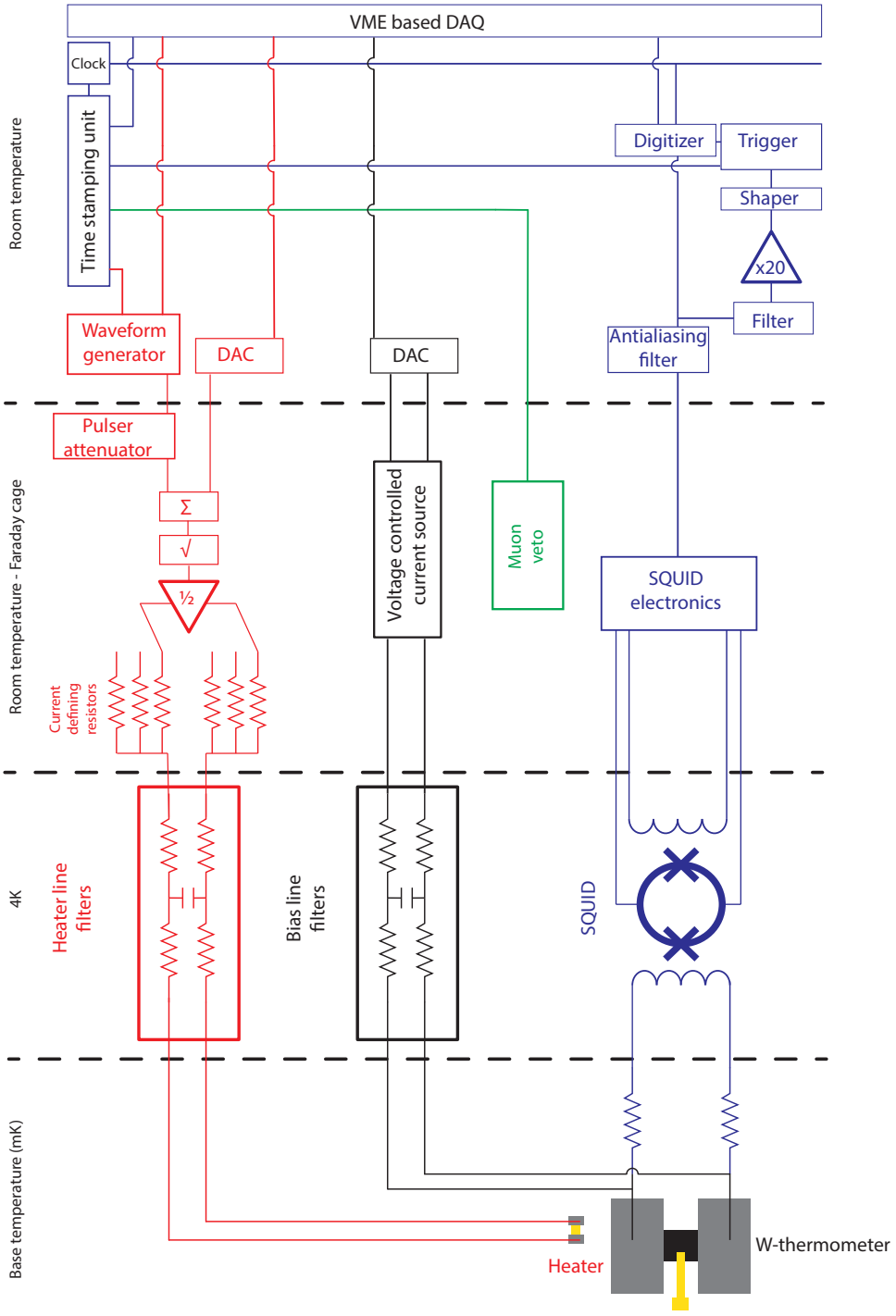

Figure 3.17: Schematics of the CRESST acquisition system. In red is highlighted the electronics driving the heater device. The heater electronics allows for the delivery of a DC current (defined by the DAC, with the purpose of heating the detector) superimposed to a time-varying signal (created by the waveform generator, it is used to generate artificial pulses such as control and test pulses). In black is represented the electronics for the electric bias current of the sensor and in blue is the SQUID electronics and data acquisition.

3.4 Basics of Data Analysis

This section gives an outline of the basic steps of the offline analysis of CRESST data. The complete description of the analysis chain and results from the CRESST-III experiment can be found in [88]. Here, the relevant points used for this thesis work are reported.

3.4.1 Pulse Amplitude evaluation

Pulses are the basic objects carrying information about particle and artificial events in the detector modules. They are characterised by a number of shape parameters, the most relevant of which is certainly their amplitude. This quantity is the one used, after calibration, to derive the deposited energy in the detector. Hence, its accurate evaluation is essential in order to fully exploit the excellent energy resolution of cryogenic detectors.

The standard way of evaluating the pulse height in CRESST is based on the so-called template fit. A central point of this thesis work is the development of a signal evaluation based on optimal filtering. Its description and advantages are reported in Chapter 4, In here, the conventional evaluation is discussed.

Template fit

Every pulse coming from a sensor is unavoidably affected by noise. In order to suppress the noise contribution, every pulse is fitted with a noiseless pulse with the right shape. Such a pulse is called a template and it is computed averaging a large number of time-aligned pulses[6]. Stochastic noise fluctuations are suppressed by the averaging process and the actual pulse shape emerges.

The amplitude is extracted by scaling the template pulse, aligning its baseline and shifting it in time to match the recorded pulse. In Figure 3.18 an example of template pulse matched to a real pulse is shown. The amplitude is the maximum of the scaled template pulse, from which the baseline offset is subtracted.

A pulse is represented as a vector of real numbers recorded from the SQUID output. Taking y_i as the vector of a recorded pulse and s_i as the one of the template pulse, the fitting algorithm needs to maximise the likelihood:

$$L_j(y_i|A) = \prod_i \frac{1}{\sqrt{2\pi}\sigma} \exp\left[-\frac{(y_i - As_{i-j})^2}{2\sigma^2}\right] \tag{3.19}$$

where σ is the RMS of the baseline and A the desired amplitude. It is important to notice that the likelihood explicitly depends on the index j. j is the time shift between the recorded pulse and the template pulse (see Figure 3.18).

The amplitude A can be extracted maximising the likelihood in Equation 3.19:

$$A = \frac{\sum_i y_i s_{i-j}}{\sum_i s_i^2} \tag{3.20}$$

[6]These pulses are selected applying a first set of quality cuts.

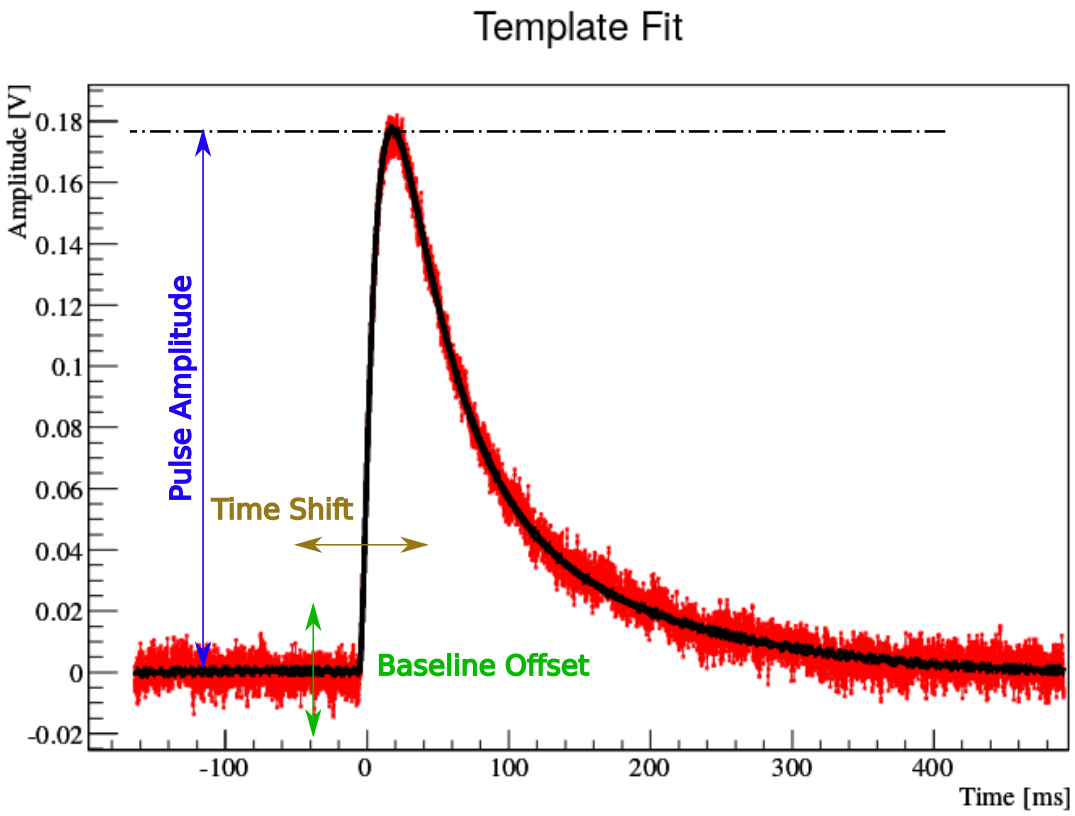

Figure 3.18: Example of pulse of detector A fitted to a template. In red are the sampled points of the pulse, in solid black the scaled and aligned template. Amplitude, baseline position and time shift are the relevant parameters to match the template to the pulse.

The dependence on j remains in the expression for A, so we write explicitly A_j. The correct j is found by the 1-dimensional minimisation of:

$$\chi^2_j = \frac{1}{n}\sum_{i=0}^{n}(s_i - A_j s_{i-j})^2 \tag{3.21}$$

where n is the size of the vectors y_i and s_i. If $\bar{j}$ is the index which minimises[7] χ^2_j, then the amplitude of the pulse is $A_{\bar{j}}$.

Baseline model

The 3-dimensional minimisation required for the fit (minimisation with respect to Amplitude, Time shift and Baseline offset) was reduced to the 1-dimensional minimisation in Equation 3.21. While we openly discussed the minimisation with respect to Amplitude and Time shift, the Baseline offset was neglected.

[7]The χ^2 minimisation, in its actual implementation, needs a search algorithm. Details in [87].

From Figure 3.18 one would consider the Baseline as simply a constant value. The situation is often different and better results are obtained accounting for a non-flat Baseline. A common choice, adopted in this work as well, is a third-order polynomial baseline model. The likelihood in Equation 3.19 becomes:

$$L_j(y_i|A) = \prod_i \frac{1}{\sqrt{2\pi}\sigma} \exp\left[-\frac{(y_i - As_{i-j} - a - bi - ci^2 - di^3)^2}{2\sigma^2}\right] \tag{3.22}$$

The maximisation of the likelihood in Equation 3.22 leads to the following set of equations:

$$\begin{bmatrix} -\sum_i s_{i-j}s_{i-j} & -\sum_i s_{i-j} & -\sum_i is_{i-j} & -\sum_i i^2 s_{i-j} & -\sum_i i^3 s_{i-j} \\ -\sum_i s_{i-j} & -\sum_i 1 & -\sum_i i & -\sum_i i^2 & -\sum_i i^3 \\ -\sum_i is_{i-j} & -\sum_i i & -\sum_i i^2 & -\sum_i i^3 & -\sum_i i^4 \\ -\sum_i i^2 s_{i-j} & -\sum_i i^2 & -\sum_i i^3 & -\sum_i i^4 & -\sum_i i^5 \\ -\sum_i i^3 s_{i-j} & -\sum_i i^3 & -\sum_i i^4 & -\sum_i i^5 & -\sum_i i^6 \end{bmatrix} \begin{bmatrix} A \\ a \\ b \\ c \\ d \end{bmatrix} + \begin{bmatrix} \sum_i y_i s_{i-j} \\ \sum_i y_i \\ \sum_i iy_i \\ \sum_i i^2 y_i \\ \sum_i i^3 y_i \end{bmatrix} = 0 \tag{3.23}$$

The set of equations 3.23 is linear and symmetric, so that it can be efficiently solved with standard numerical methods. An example of a pulse fitted with such baseline model is depicted in Figure 3.19.

Truncated fit

Another complication arising from the amplitude evaluation of pulses generated by a TES is the strong non-linearity at large amplitudes. In this regime, the pulse shape dramatically changes and a standard fit is not possible.

The solution to overcome this limitation is to define a truncation limit. The truncation limit defines the maximum signal height to be considered for the fit. As the signal develops over time, the shape is affected by the shape of the transition of the TES. The truncation is then defined to mark the maximum signal height at which the TES output can be considered linear. The implementation of the truncated fit consists basically in restricting the running index i of the likelihood in Equation 3.19 to those samples with a value lower than the defined truncation limit t: $i \mid y_i < t$. A saturated pulse fitted with a truncated template is shown in Figure 3.20.

3.4.2 Calibration

The determination of the energy of a certain particle interaction is carried out mapping the amplitude A_x, where the subscript x indicates the interaction type, into the corresponding energy E. The calibration function $f(A_x) \Rightarrow E$ is determined exposing the detector modules to a known radioactive source. In CRESST a ^{57}Co source is usually employed. The two gamma peaks of energies 122.06 keV and 136.47 keV are used to set the absolute scale of the calibration. Because of the double-channel readout, two functions are necessary for each detector module. For the phonon channel, as the signal amplitude is a precise measure

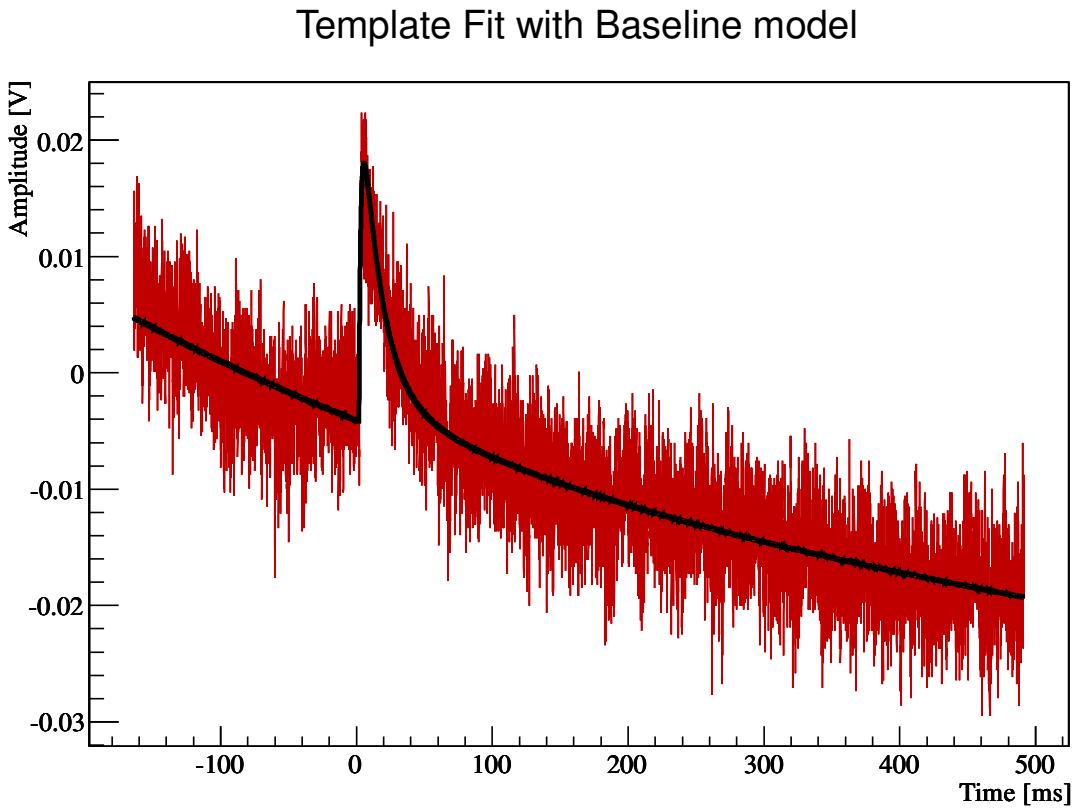

Figure 3.19: Template fit to a pulse with a third-order polynomial baseline model. In contrast to the case in Figure 3.18, the baseline here is substantially non-flat. The fit without a model for the baseline shape would lead to a misreconstruction of the amplitude, resulting in a worse detector resolution.

of the deposited energy, the pulse-amplitude of a γ interaction is directly converted into the corresponding energy. The light channel is calibrated using the scintillation light emitted by the main absorber as a consequence of the deposition of the energy E. Therefore, the light channel is calibrated in **electron equivalent** keV and the convenience of the aforementioned definition $LY_{\gamma}(122keV) = 1$ becomes clear.

The function f is chosen in order to account for non-linearities in the detector response. Monoenergetic lines artificially generated by means of the injection of test pulses are used to map the detector response at several energies so that a suitable f (typically a polynomial function or a spline) can be determined. In addition to that, test pulses can account for time-dependence in the detector response. See [87] for details.

3.4.3 Cuts

The detector output can be affected by a number of disturbances and working conditions which deteriorate the performance and, ultimately, spoil the sensitivity to dark matter

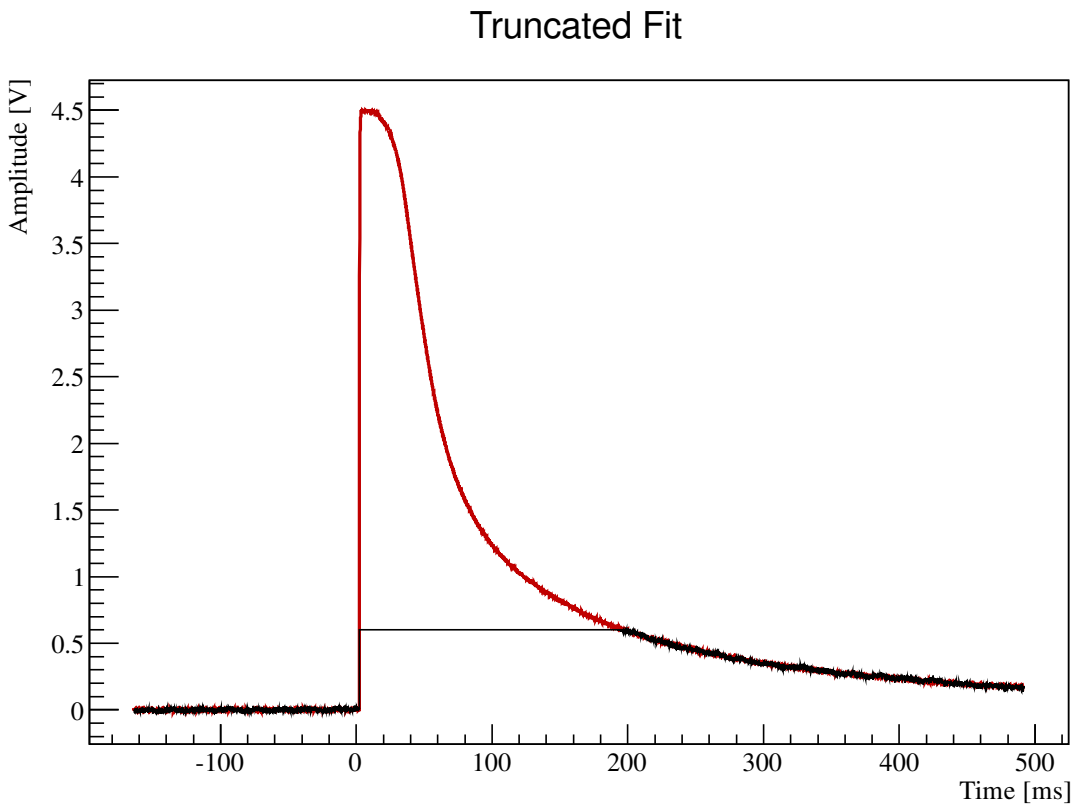

Figure 3.20: Template pulse fit with truncation limit at 0.6V. All samples above the truncation limit are not considered by the fitting algorithm.

particle interactions.

A data selection is, therefore, necessary. The main selection criteria are listed here.

- **Stability:** As already remarked, the temperature at which each sensor is operated is a crucial parameter defining the detector output. The monitoring of this parameter is done with the injection of control pulses. Time periods when the working point deviates from the optimised value are excluded from the analysis.

- **Coincidences:** The rarity of a dark matter particle interaction is such that multiple scattering in different detectors of the same particle is not to be expected. Therefore, time-coincident events in different detectors are to be rejected. In addition to the rejection of time coincident events across cryogenic detectors, time-coincidences with the muon veto are also not considered for dark matter analysis.

- **Data quality:** The energy reconstruction of a particle event is a central aspect of the data analysis and the amplitude evaluation is definitely of major importance. Events whose amplitude can not be reliably calculated are a source of data pollution and, hence, a quality selection is needed. Several parameters characterising the shape

of pulses are used to design cuts addressed to tag electronic glitches, SQUID resets, pile-up, and improperly shaped pulses. Out of many, the RMS of the template fit is a very general and powerful indicator of the quality of the amplitude reconstruction.

3.4.4 Sensitivity to dark matter

The discovery of dark matter particles scattering off nuclei requires a detailed understanding and modelling of the backgrounds and of the expected signal. The latter was discussed in the previous chapter, the former is very detector-specific and may be insidious. Likelihood-based methods are the most suitable tools to support the claim for a positive signal.

The current scenario is somewhat easier, given the absence of confirmed positive signals. The sole exclusion of a nucleon-dark matter particle elastic scattering cross-section σ for a dark matter particle of mass m_χ can be evaluated conservatively in the presence of unknown background. CRESST exclusion limits are usually computed using the Yiellin Optimum interval method[89]. The general framework is presented in the following section.

The acceptance region

The Light Yield vs. Energy plot is the condensation of CRESST data from which the spectrum of accepted events is extracted. The acceptance region in Light Yield is chosen to include 50% of the oxygen recoil band as the upper limit and the 99.5% lower boundary for the tungsten recoil band as the bottom limit.

Because of the loss of coherence in the scattering off tungsten, an upper limit in energy is set at 40keV. No lower limit is set, and events with energy down to threshold are accepted in order to fully exploit the sensitivity to low mass dark matter particles. A precise characterisation of the energy threshold is, therefore, mandatory and it will be the main focus of this thesis work.

The Yiellin maximum gap method

The input for the dark matter sensitivity computation is the set of events lying in the acceptance region. Given the set of accepted events with energy $E_i (i = 1, ..., N)$, first we define the "size" of the ith **gap** x_i as:

$$x_i(\sigma; m_\chi) \equiv \int_{E_i}^{E_{i+1}} \frac{d\Gamma(\sigma; m_\chi)}{dE} dE \tag{3.24}$$

where $d\Gamma/dE$ is the expected differential spectrum due to the interaction of dark matter particles of mass m_χ and cross-section σ. From such a definition, $x_i(\sigma; m_\chi)$ is the number of expected events in the energy range (E_i, E_{i+1}). E_0 and E_{N+1} are defined as the extremes of the acceptance region in energy.

We choose the gap $\bar{x}$ out of the set $\{x_i\}$ with the maximum "size": $\bar{x} = x_i | x_i = \max_i\{x_i\}$. As gaps are defined across adjacent events, the number of observed events

in each gap is always 0. Hence, x_i also assumes the meaning of the difference between the number of expected events and the number of observed events in the energy range (E_i, E_{i+1}). See Figure 3.21. The size of the maximum gap depends on the assumed σ. The

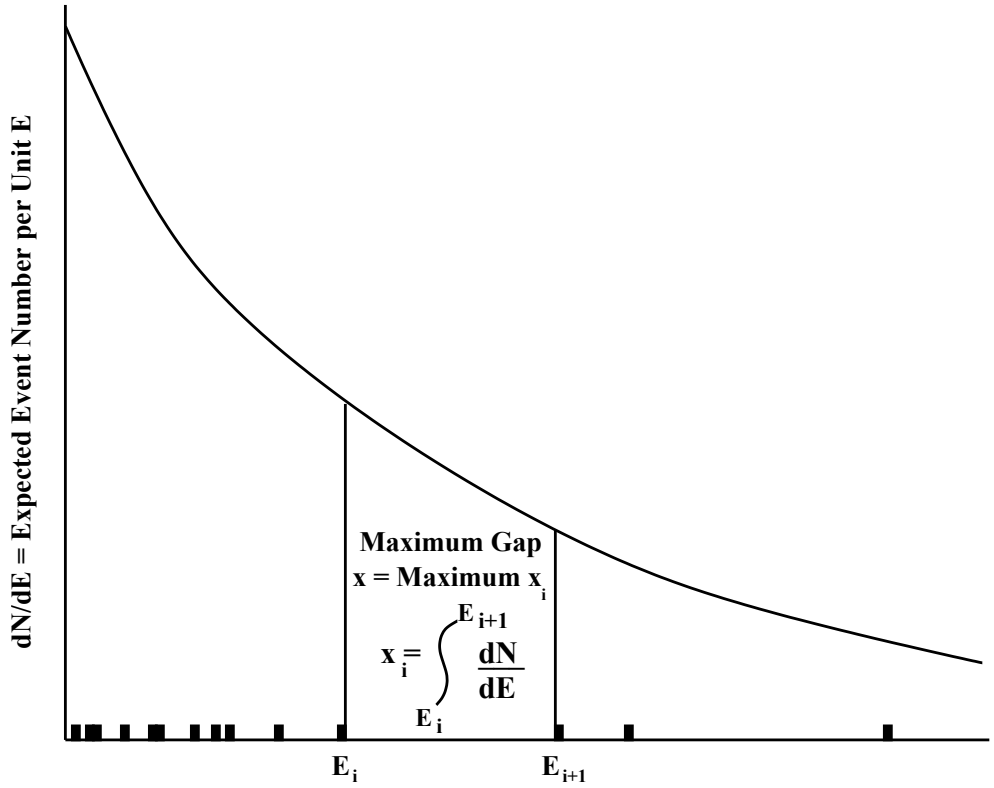

Figure 3.21: Representation of the maximum gap method. The black rectangles represent the energies of the accepted event. The solid line is the expected spectrum for the given σ. The maximum gap corresponds to the largest area under the solid line contained between two adjacent events. Picture from [89].

larger the σ, the larger the $\bar{x}$. One can set σ so large that $\bar{x}$ excludes the zero observed events in the maximum gap to a certain confidence level. In order to make this idea quantitative, we define μ as the total number of expected events in $[E_0, E_{N+1}]$. It is proven that the probability for the maximum gap $\bar{x}$ being smaller than x is:

$$C_0(x,\mu) = \sum_{k=0}^{m} \frac{(kx-\mu)^k e^{-kx}}{k!} \left(1 + \frac{k}{\mu - kx}\right) \tag{3.25}$$

where m is the largest integer such that $m \leq \mu/x$. $C_0(x = \bar{x}, \mu)$ is then the confidence level at which the σ can be excluded. We observe that m rises as σ rises, as does C_0.

The procedure to exclude σ at 90% C.L. consists of evaluating $C_0(x = \bar{x}; \mu)$ for increasing values of σ until it reaches the value 0.9.

The optimum interval

In case of an elevated density of events in the data, the maximum gap method may not be really convenient. High density of events implies very small gaps and hence, few expected events.

The maximum gap method can be generalised considering **intervals**[8] instead, so that a non-zero number of observed events is considered in comparison with the number of expected events. In the absence of background, we define $C_n(x, \mu)$ as the probability that the sum of all expected events in the intervals containing up to n observed events is $\leq x$. This definition of $C_n(x, \mu)$ has no analytical expression and needs to be tabulated. $C_n(x, \mu)$ increases as x increases, and as n decreases.

Once n is chosen, we can determine the interval with the maximum number of expected events $\bar{x}$ and compute $C_n(x = \bar{x}, \mu)$. Similar to $C_0(\bar{x}, \mu)$, we interpret $C_n(x = \bar{x}, \mu)$ as the confidence level at which we can reject σ for being too high, given μ and $\bar{x}$. The maximum gap method is then a special case where n is forced to 0 *a priori*.

In the case of the optimum interval method, we are free to choose n, resulting in the most compelling exclusion of the input σ: $C_{max} = \max_n C_n(x, \mu)$. The "toll" to pay for such a choice is that C_{max} is not the desired confidence level, as it would have been determined *a posteriori*. We define the function $\bar{C}_{max}(C, \mu)$ such that the fraction C of all experiments

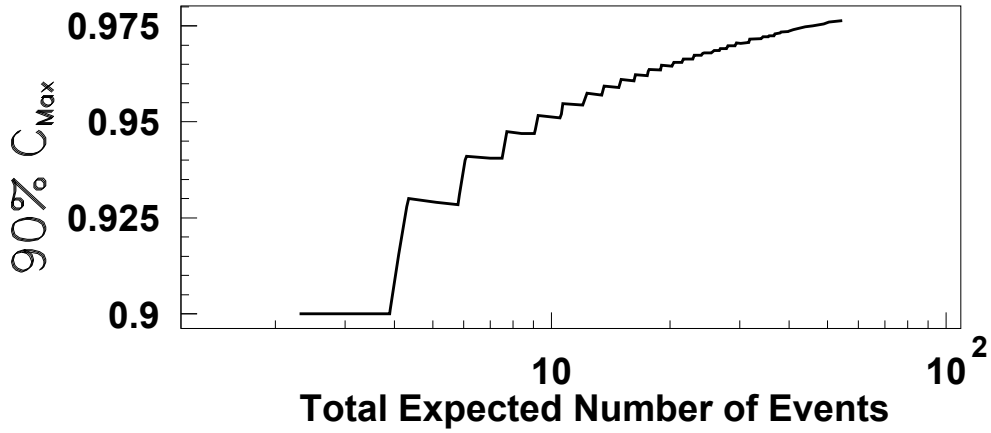

Figure 3.22: $\bar{C}_{max}(0.9, \mu)$ as a function of the total number of expected events μ. It the value that C_{max} needs to reach varying σ to find the 90% CL of exclusion for that σ. Plot from [89].

with a fixed μ to have $C_{max} \leq \bar{C}_{max}(C, \mu)$, so in order to exclude σ at 90% confidence level, one has to increase σ to find $C_{max} \leq \bar{C}_{max}(0.9, \mu)$. In general it holds $C_{max} > 0.9$, being the penalty for the freedom of choosing n. $\bar{C}_{max}(C, \mu)$ has also no analytical expression and needs to be tabulated with Monte Carlo methods. $\bar{C}_{max}(0.9, \mu)$ is shown in Figure 3.22.

[8]Differently from gaps, intervals are not constrained to have adjacent events at the end points. They can even have no events at the endpoints. Nonetheless, such intervals can be extended to the proximity of the closest event (or to the end of the acceptance region) without changing C_n. So the amount of possible C_n given N observed events is (N+1)(N+2)/2.

Chapter 4

Lowering the energy threshold

The foremost aspect considered for the development of the CRESST-III experiment is attaining a low energy threshold, even at the price of reducing the exposure. The design goal, based on the results from CRESST-II, was set to achieve a threshold of 100eV. The detectors, keeping their working principle, had been completely redesigned in almost all their aspects in order to achieve the required performance.
The key parameter in defining the energy threshold is the signal-to-noise ratio (S/N ratio). The strategy followed was to improve this quantity by increasing the signal amplitude, i.e. the sensitivity. A complementary way to improve the S/N ratio is to apply pulse reconstruction algorithms that are tailored to each sensor. It is no longer the physical signal from the detector which is optimized, but rather the algorithm which extracts the signal amplitude from the raw signal. Such algorithms initially require an iteration of data processing in order to fully characterize the detectors' response, after which they can be applied to the whole produced data. The CRESST setup as in Chapter 3 does not allow for a full data reprocessing since all the data which does not fire the hardware trigger is lost. Another disadvantage of relying on a hardware trigger is the mismatch between pulse amplitude reconstruction carried out by the trigger, hardcoded in the electronic board, and the more accurate one implemented in data analysis.
In this chapter, a new data acquisition specifically designed for full data reprocessing is presented, along with a trigger algorithm which effectively lowered the energy threshold of the detectors. Results and the impact on the sensitivity of dark matter particles are discussed.

4.1 A triggerless acquisition for CRESST-III

The straightforward approach to allow for full data reprocessing is to record and save to disk the continuous stream of all sensors during operation. This task can be perceived as equivalent to the digitisation of a triggered events, with the difference that the total number of acquired samples needs to be large enough to represent the sensors' output,

or *datastream*, during measurement time[1]. The recorded data must be manipulated in order to extract the events and present them in a form that can be fed into the CRESST analysis chain, see Section 3.4 and Appendix A. The output of the detectors is not the only information needed, as the CRESST installation (see Section 3.1), among other things, consists of a muon veto and an artificial pulse generator which are operated in contemporaneity with the cryogenic detectors. The new continuous data acquisition system then needs to be integrated with the standard acquisition of the experiment.

4.1.1 The continuous sampling of the datastream

The solution adopted to sample the detectors during operation requires the doubling of the number of sampled channels. Each output from the detectors is split into two lines and these are each fed into two separate transient digitisers. The transient digitisers are then operated in a switching mode, such that when one is sampling, the other is being read out. This guarantees that no sample from the datastream is lost during the read out, as long as the memory buffer of the sampling digitiser is deep enough to store the data, while the other module is transferring its own (filled) buffer to the acquisition computer. Figure 4.1

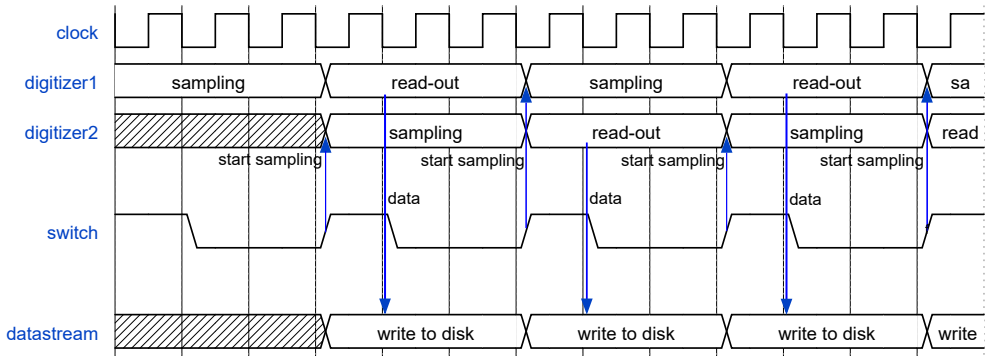

Figure 4.1: Sketch of the basic principle for the continuous read-out. Two digitisers are operated in parallel and supplied with the same sampling clock. As one starts being read-out, the second one samples the detectors' output. Assuming full reliability of the switch signal, no sample is lost while writing the datastream to disk

shows how the digitisers are used. Crucial to the proper acquisition is the timing of the switch (or synchronisation) signal.

Synchronization of the digitisers

The device used to built the acquisition described in this chapter is a commercial 16-bit, VD80 transient digitiser [90], which can sample up to 16 channels simultaneously. Its internal buffer can store 16MSamples per channel. The requirement for CRESST-III is a

[1]Because of the maintenance of the cryogenic infrastructure, the data taking is interrupted approximately every second day.

sampling rate of 25kHz, meaning that the maximum storage of one digitiser is 640s. The VD80 device can sample the data indefinitely and take a shot of limited size upon a TTL signal called the trigger[2]. The internal buffer can be subdivided into regions of different sizes (refer to Figure 4.3):

- Pretrigger region: user-specified number of samples (presamples) stored before the trigger signal (trigger1).
- Posttrigger region: user-specified number of samples (postsamples) stored after the trigger signal (trigger2).
- Shot: total number of samples recorded. This is greater than presamples+postsamples. It it guaranteed that the samples exceeding presamples+postsamples come after the last postsample.

In Figure 4.2 this structure of the buffer is depicted. An additional feature of the VD80

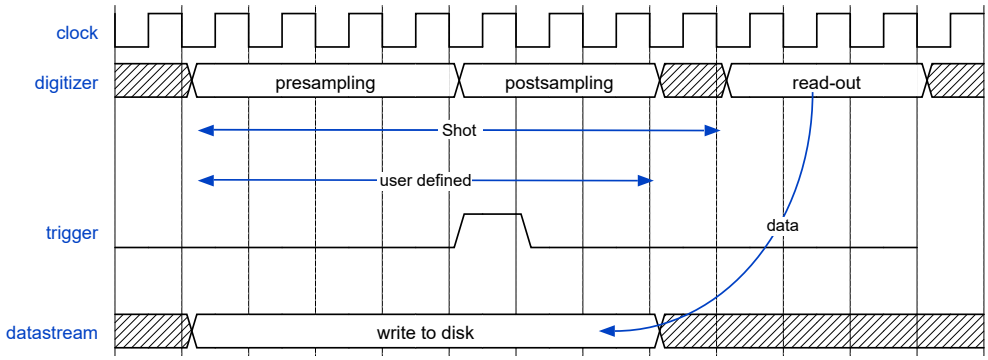

Figure 4.2: VD80 digitiser read-out. The digitiser stores the data at input and saves it after receiving a trigger signal. It can be configured to store a user-defined number of samples in the pretrigger and posttrigger regions. The trigger position is the only reliable timing in the picture.

is the possibility to delay the reaction to the trigger signal, by a specified number of clock counts, and to regenerate it at that time. Since we need a self-running system with accurate timing, this possibility is used to synchronise the two boards. Given the scheme in Figure 4.2, the pretrigger region is used to store the actual data while the posttrigger region is discarded. What follows is the list of executed steps to carry out continuous sampling, with Dig1 and Dig2 representing the two digitisers:

1. Dig1 and Dig2 are both sampling. Dig1 generates a trigger and keeps storing the samples until the buffer is full. As soon as the buffer is full Dig1 is read-out and returns to its sampling state.

[2]The trigger signal used in the DAQ implementation has nothing to do with the trigger used to tag pulses.

2. Dig2 receives the trigger signal from Dig1 and waits a number of clock cycles equal to the size of the pretrigger buffer, then it reacts to the trigger storing the postsample data and it regenerates the trigger.

3. Dig2 fills up the buffer, it is read out, and Dig2 returns to sampling state.

4. Dig1 waits a number of clock cycles according to the buffer size of the pretrigger in order to regenerate the trigger.

5. Return to point 1.

Given this scheme, it is necessary to define the presampling region big enough to store data for the time needed to: fill the posttrigger region, complete the shot, and transfer the data to the disk. A visual depiction of this scheme is given in Figure 4.3.

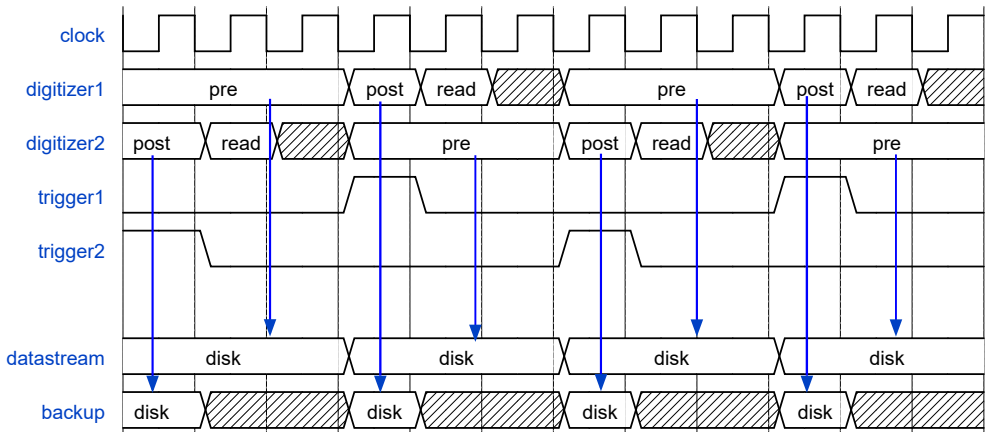

Figure 4.3: Complete schematics of the continuous read-out using two switching digitisers. The trigger synchronisation allows for continuous datataking without loss of samples, as long as the pretrigger memory is deep enough to buffer the data during posttriggering and read-out. Although the postsamples are not needed, they are saved separately from the presampling data (the actual continuous datastream) as a safety measure. In case of accidental misalignment of the trigger signal, given that the misalignment, in clock cycles is not greater that the number of postsamples, the datastream can be fully retrieved.

Aligning the trigger to the clock

One subtle aspect regarding the continuous DAQ and its proper timing needs to be elucidated. As the VD80s rely only on the trigger signal to take data and provide proper time alignment, the time difference between two trigger signals must be constant in time, at least within a tolerance in the order of the sampling rate. This is unfortunately not the case. The propagation of the trigger signal through the VD80s undergoes a delay, somewhere in between 25ns and 50ns (from manufacturer specifications). Such a delay may not be problematic for one cycle between two boards. However, in order to match

the CRESST-III requirements, six boards are needed, and long term reliability must be provided since a typical measurement in CRESST lasts several days. In order to overcome such inconvenience, some foresight is vital. Given that each clock cycle is made of one rising and one falling edge, the actual data sampling can be aligned to the down falling edge of the clock, while the trigger signal generation to the upward rising one. This approach allows for accurate timing within the required resolution, as long as the introduced delay is shorter than one half of the clock cycle.

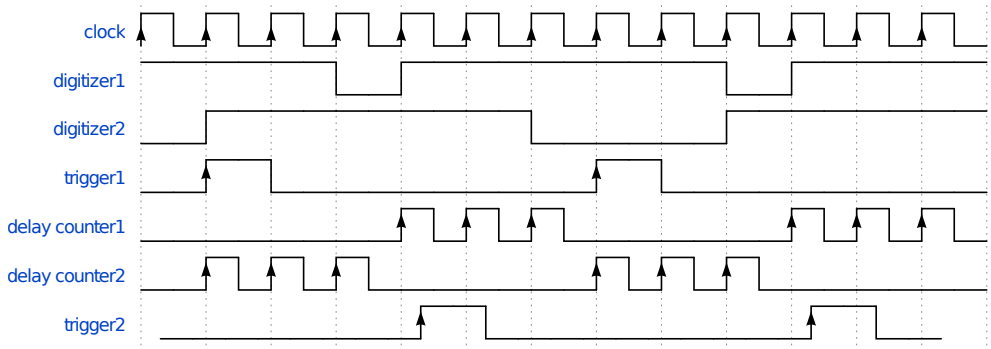

Figure 4.4: Graphic representation of the proper timing of the trigger signal. The high state for the digitisers means sampling state. The digitiser 1 is always generating a trigger signal aligned to the upward rising edge of the sampling clock. Any further propagation of the trigger signal undergoes a delay. The sampling itself takes place at the downgoing edge of the clock. Provided that the trigger delay is shorter than half a clock cycle, the reaction upon the (delayed) trigger signal is guaranteed to occur before the next sampling operation.

Uniform behaviour of the two digitisers

Analog-to-digital converters can be affected by gain and/or offset errors, i.e. the digitised signal can appear deformed and shifted compared to the original, analog signal. Such effects are usually quantified by the manufacturer. For the case of the VD80, the gain error is stated to be below 0.05% and the offset error 3LSB at most. Such inconveniences are usually not problematic for a standard acquisition, as they would uniformly affect the data in its entirety and can be accounted for, i.e. with calibration. In the case of interest, it is important to provide a datastream whose chunks do not show any difference due to the operation of two digitisers. In order to prove that the data produced with the acquisition described so far is not affected by differences between the digitisers, a test was conducted. Instead of operating the digitisers in switching mode, they were set to sample the input in contemporaneity and supplied with a sawtooth-like signal. Figure 4.5 shows the recorded signal by the two digitisers and their difference.

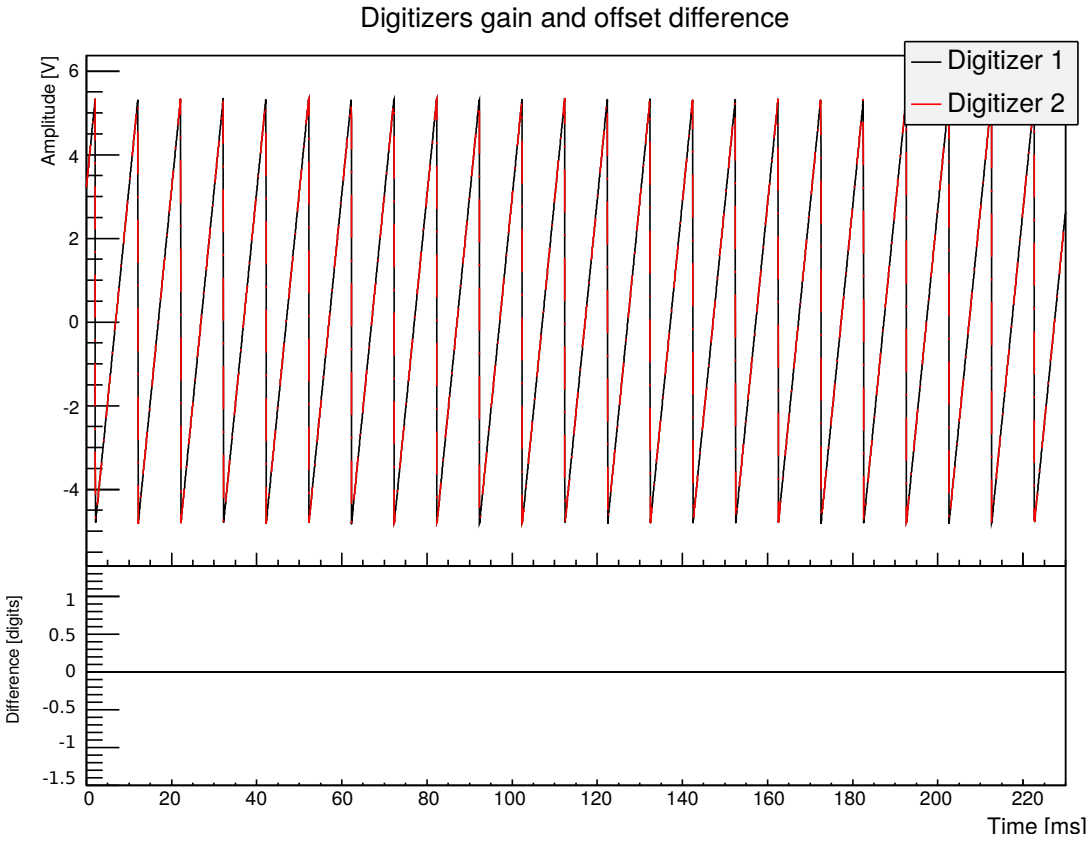

Figure 4.5: Recorded signal from two digitisers. The acquisition boards have an input range ±10V and 16bit resolution (1bit corresponds to 0.3mV). The two VD80s were operated in parallel and recorded a signal injected with a function generator in the same channel. In red and black (upper plot) are the digitised signals. In the bottom the subtraction of the two signals is shown. No difference is present down to one digit.

4.1.2 Integration in CRESST-III

The CRESST setup provides several types of information regarding detectors' operation and the surrounding environment. Crucial for the proper usage of the recorded data are the following:

- Muon data: time and signal amplitude of signals coming from the muon veto, necessary to identify muon interactions in the detectors.
- Pulser data: time and amplitude of signals generated by the pulser. These data are needed to tag artificially-induced heater pulses in the detectors.
- Control data: time and reconstructed amplitude of control pulses. These data are needed to identify working point variations over time and tag time periods of stable detectors' operation.

The time information is the essential parameter in the aforementioned points, needed to properly integrate the continuous DAQ in the CRESST experiment. The new configuration of the CRESST installation is shown in Figure 4.6. As for all the other components of the experiment, timing is carried out by the time stamping unit. The trigger signal previously described is fed into the time stamping unit, so that the datastream produced with the new acquisition can be aligned to match the rest of the output of CRESST.

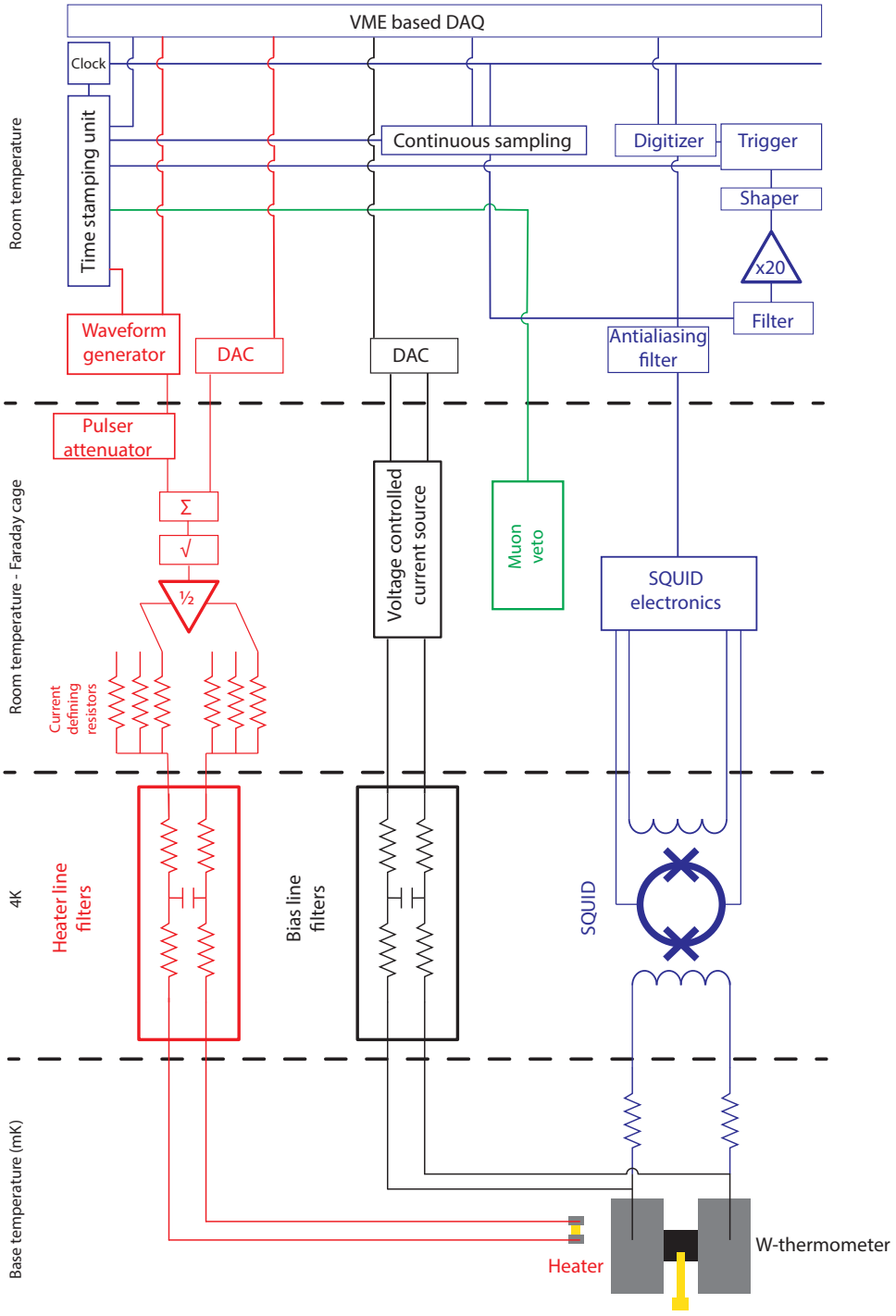

Figure 4.6: Updated schematics of the CRESST installation in Laboratori Nazionali del Gran Sasso with the new acquisition.

4.2 Raw Data Stream

The detectors' output is digitized at 25kHz with 16-bit resolution and the whole output is provided by the acquisition described in this chapter. Figure 4.7 shows a small chunk of data stream from the phonon channel of Detector A. The artificially generated heater pulses are tagged in the stream using the pulser data and the synchronization signal of the continuous DAQ. A datastream as in Figure 4.7 is given for every active channel in

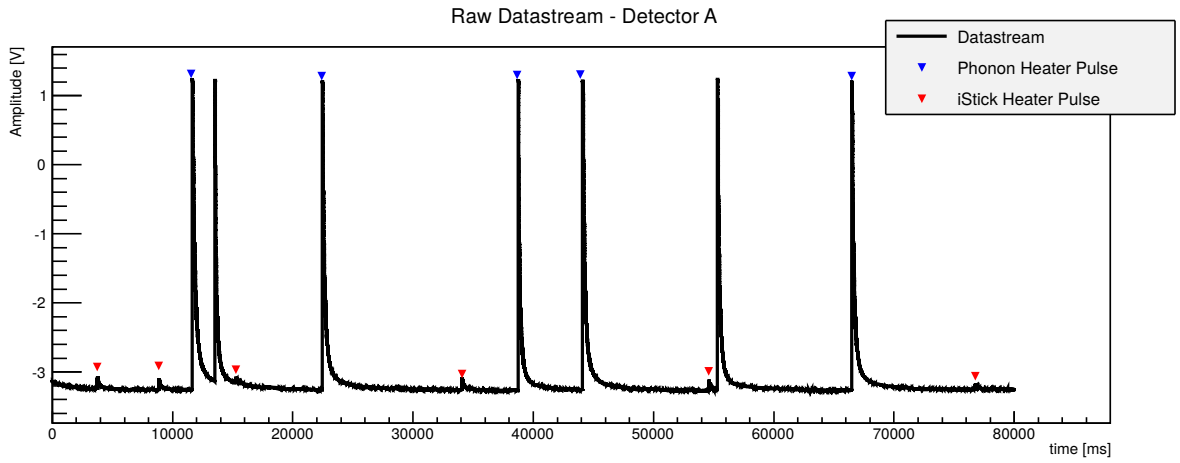

Figure 4.7: Sample of datastream from the phonon channel of Detector A (solid black line). Blue diamonds are heater pulses generated on the main adsorber. Red diamonds are heater pulses generated on the iSticks that appear on the phonon channel because of the direct contact between the main adsorber and the iSticks. Pulses with no marker are particle induced.

CRESST-III. In order to make use of such data, it is fundamental to implement a trigger algorithm able to identify pulses in the datastream and group them together detector-wise (event building). Three (main) advantages come from event building based on the raw datastream, compared to the use of a hardware trigger (as in CRESST-II):

- The energy threshold can be (re-)defined *a posteriori* and optimised to the actual data (no risk of data losses).
- The amplitude evaluation from the software trigger is the same as the one carried out in the analysis.
- The amplitude evaluation at trigger level can be more sophisticated than what can be implemented in hardware, resulting in a lower threshold.

These points will be expanded in the following section of this chapter, dedicated to the implementation of a low threshold trigger for the CRESST-III experiment.

4.2.1 Digital filtering

A trigger is a functionality which, given its input, is able to timestamp a desired class of signals. In the case of cryogenic detectors the sought-for signal is a pulse as the ones shown in Figure 3.10. A sketch of the trigger circuit adopted in CRESST-II (and still in operation in CRESST-III) is reported in Figure 4.8. The input of such a device is the

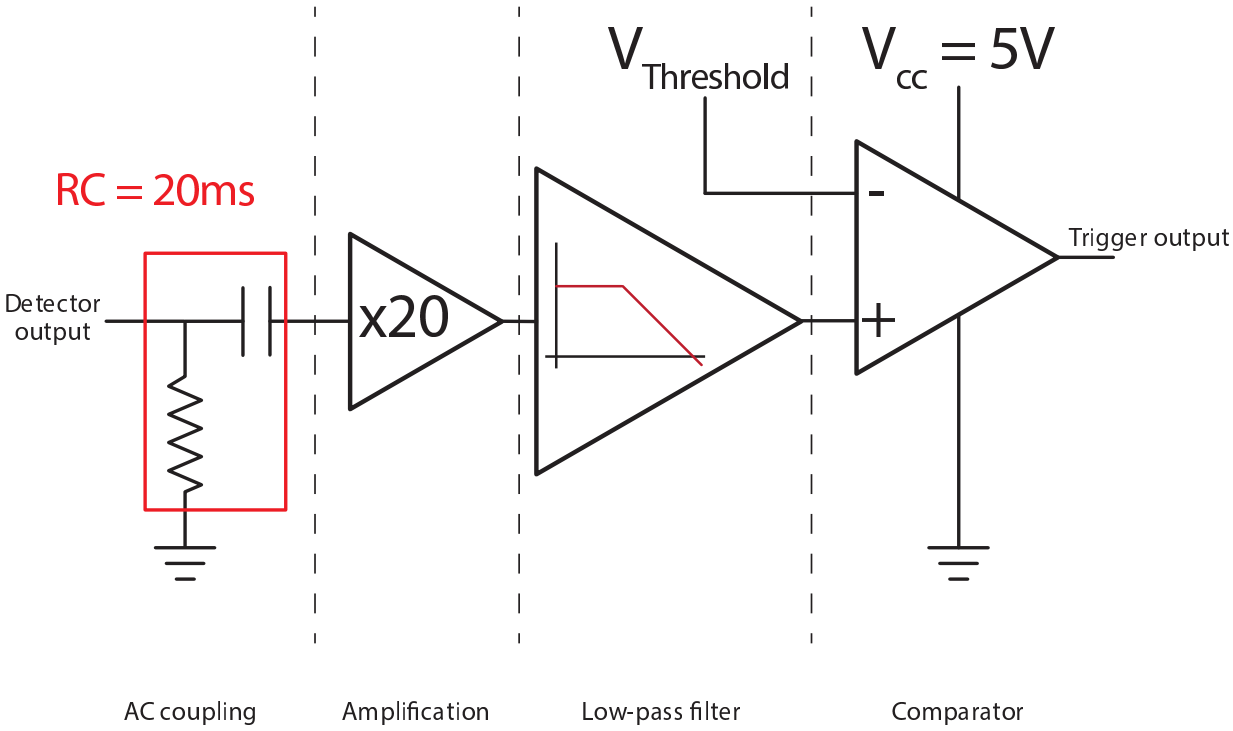

Figure 4.8: Generation of the hardware trigger logical output in CRESST. A first stage AC couples the signal from the detector in order to subtract the baseline (DC component). The signal is then amplified and fed into a (programmable) low-pass filter. This stage is meant to boost the signal-to-noise ratio, as the noise should extend over all the frequencies, while the signal is bandwidth-limited. The final stage is a simple comparator which outputs a logical signal as soon as its input exceeds the supplied threshold voltage value.

signal directly from the detector and its output is a logical signal (TTL) fired at the time when the trigger criterion is satisfied. The criterion chosen in CRESST is simply based on the threshold crossing of the filtered signal. Therefore, the filter's output is the signal to be compared to the desired threshold value.

The newly deployed continuous data acquisition allows for a flexible trigger implementation. The filter output, in particular, defines the signal-to-noise ratio, which limits the threshold that can be set. In case of too low a threshold, the (inevitable) baseline noise fluctuations would drive the comparator, resulting in a chaotic and useless trigger signal. A crucial point of this thesis work is to use a filter specifically optimised to the operating conditions of each sensor, in order to improve the S/N ratio and thus, reach a

lower threshold value compared to the one achievable with the hardware trigger.

The very first issue to tackle to achieve this goal (even before the definition of the filter) is how to process the datastream as it is acquired. In the system shown in Figure 4.8, the signal is constantly passing through the filter and being monitored by the comparator. If $y(t)$ is the raw signal from the detector, $y_F(t)$ the output at the filter, and $H(t)$ the filter response function, these quantities are related by the convolution operation:

$$y_F(t) = \int_{-\infty}^{+\infty} H(\tau) y(t-\tau) d\tau \tag{4.1}$$

Equation 4.1 is often handled in frequency domain where, thanks to the convolution theorem, it assumes the easier form:

$$\hat{y}_F(\omega) = \hat{H}(\omega)\hat{y}(\omega) \tag{4.2}$$

where the $\hat{}$ symbol stands for the Fourier transform of the function.

It is clear that a real data treatment needs to use Equations 4.2 and 4.1 in their finite form, i.e. all the mentioned functions are limited in time and have a finite number of samples. The convolution theorem in its finite form states the following equivalence:

$$\sum_{k=-M/2+1}^{+M/2} H_k y_{j-k} = \mathscr{F}^{-1}\{\hat{H}_i \hat{y}_i\}_j \tag{4.3}$$

where $\hat{H}_i$ and $\hat{y}_i$ are the discrete Fourier components of the filter and the signal respectively. $\mathscr{F}^{-1}$ denotes the inverse discreete Fourier transform. H is often called the finite impulse response (*FIR*) of duration M. An exhaustive description of discrete data treatment with the Fourier transform can be found in [91].

There are two assumptions behind the equivalence 4.3:

1. y_j must be a periodic signal with period M.
2. y_j and H_j are both of duration M.

In the case of the continuous datastream, both assumptions are not satisfied in the form they are stated above. y_j is the sampled signal from a temperature sensor, a very large sequence of values acquired during the detector's operation without any periodicity. The second assumption does not hold since the typical detector output to a particle interaction lasts several milliseconds, whereas the continuously sampled output lasts days. An easy workaround to the second requirement is the splitting of y_j into several chunks, each with the same duration as H_j, so that they can be filtered individually and merged together at the end of the processing.

The first point is more complicated to overcome. Even if no periodicity is present in y_j, no matter how large the total number of samples N, the computation of the discrete Fourier transform will always result in a wrapped-around function with periodicity N.

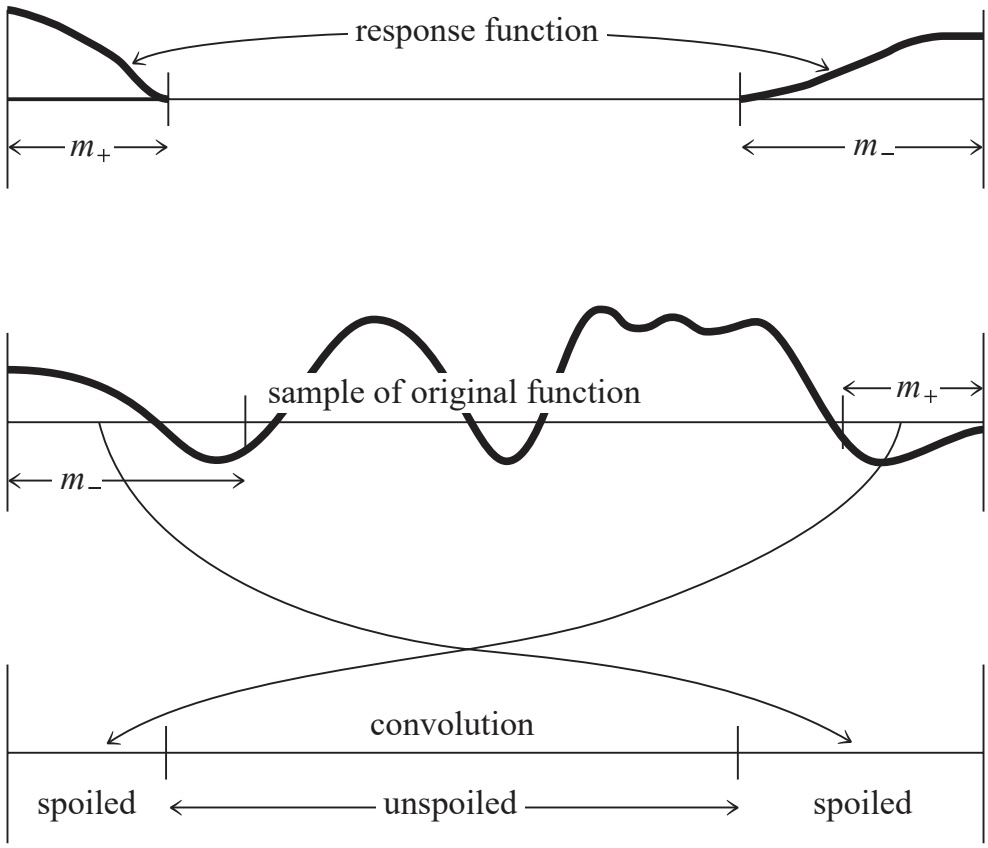

Figure 4.9: Graphic representation of finite convolution of two signals. The response function (upper part) had beed extended with 0s to match the length of the signal (middle part). In the resulting convolution (bottom part), polluted and unpolluted samples due to the wrap-around are highlighted. Picture from [91].

In Equation 4.3 all the samples y_{j-k} where $j - k < -\frac{M}{2} + 1$ and $j - k > \frac{M}{2}$ do not exist and, because of the assumption of periodicity, these are replaced with the periodic extension of y_j according to $y_{j+N+M} = y_{j+N}$, giving rise to the wrap-around problem as depicted in Figure 4.9. It is important to note that the number of samples affected by this issue equals the amount of the non-zero samples of the impulse function. The affected samples are those at the two ends of the signal y_j. The solution adopted in this work makes use of the largeness of the sequence of samples y_j (compared to H_j) and the necessity of splitting them into chunks in order to process them with a finite memory machine. Given the finite impulse response H_k of duration M, the procedure adopted is the following:

1. Take a chunk of samples of size $2M$ from the datastream.
2. Zero pad H_k to extend it to $2M$ samples.
3. Apply the convolution as in Equation 4.3.
4. Discard the first and the last $M/2$ samples.

5. Shift in the datastream by M samples, start again from point 1, and append the convolution output to the current one.

This algorithm guarantees that the processed data does not suffer from wrap-around problems, as the affected M samples are discarded in point 4, and that the actual output reproduces what is done at the filter in Figure 4.8, with the freedom of choosing any desired filter, specifically filters which cannot be implemented in hardware, in order to reach the lowest threshold possible. Figure 4.10 shows how the filtered datastream is built.

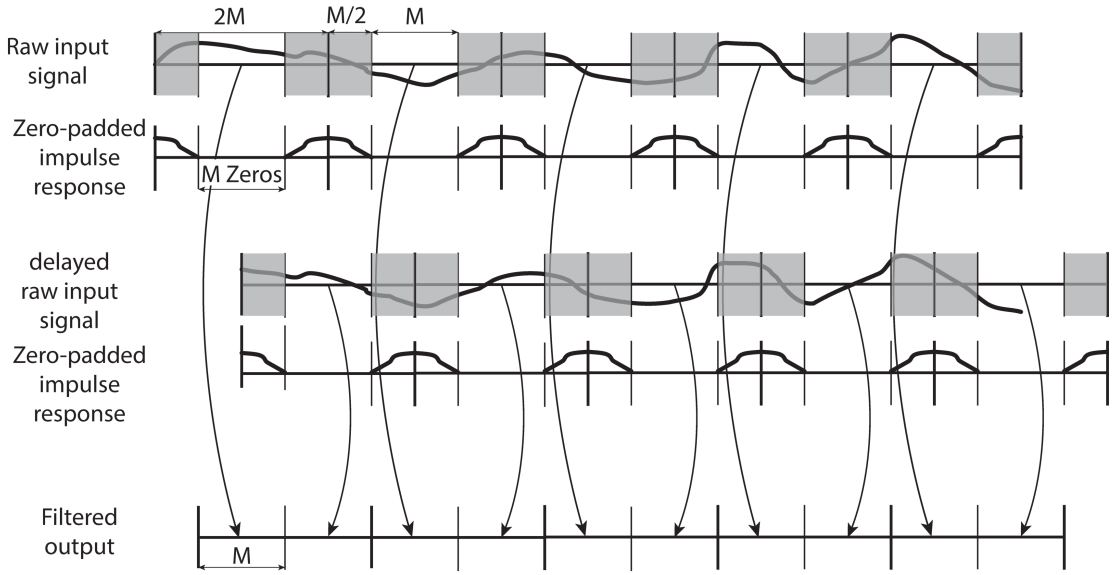

Figure 4.10: The assembling of the continuously filtered datastream. The raw datastream is split into chunks of size $2M$ and the zero-padded response function is applied to each chunk. The first and the last $M/2$ samples (grey-shaded areas) are discarded. The same procedure is re-applied to the raw datastream, but in this second case all the data is delayed by M samples. The unpolluted samples from the raw datastream and the delayed datastream are contiguous in time and can then be attached together, producing a time-consistent filtered datastream.

4.2.2 Boosting the S/N ratio: Optimum Filter

In cryogenic detectors, particle interactions cause a temperature rise followed by thermal relaxation which restores the original working temperature of the detector. The temperature rise and the subsequent relaxation result in a specific pulse-like detector's response, whose shape, for the case of CRESST sensors, is well-modelled with an exponential rise and two decaying components (thermal and non-thermal, for details see Section 3.2.3). The actual shape of the detector's response is, in good approximation,

independent of the deposited energy (in linear regime[3]), so that the information of the deposited energy is entirely encoded in the pulse amplitude. We are now interested in the reconstruction of this amplitude with the highest possible accuracy.

Statement of the problem

In real world applications, the detector output is always superimposed to noise of various origins (vibrations, thermal fluctuations, electronics...). The additive nature of the noise allows us to write the output to a particle interaction, occurring at time t_0, as:

$$y(t) = As(t - t_0) + n(t) \tag{4.4}$$

In Equation 4.4 $s(t - t_0)$ is the ideal detector output (or template pulse), normalized to unity for later convenience and the onset placed at t_0, A is the signal amplitude (deposited energy after calibration), and $n(t)$ is a stochastic term representing the noise. We are interested in the best evaluation of A. This can be obtained using a **least square** method. The strategy followed to address the issue is based on a class of filters which known as Optimum Filters. See [92] and [93] for an in-depth discussion of optimum filters and their applications to particle detectors.

The case of white noise

We begin with a simplified situation in which, without loss of generality, the signal consists of two rectangles of short width Δt, amplitudes A_1 and A_2 respectively, mutual time distance τ, and ergodic white noise bandwidth limited to $1/\Delta t$. The ratio A_1/A_2 is fixed to α and the sought-for amplitude is A_1 only. It is convenient to normalize the first rectangle to 1, so that we can express the signal as $A_1 s(t)$, where $s(t)$ is our template waveform. If we naively extract A_1 from the first rectangle only (see Figure 4.11), the S/N ratio is $A_1/\langle v_n \rangle^{\frac{1}{2}}$, where $\langle v_n \rangle^{\frac{1}{2}}$ is the ensemble root mean square of the noise. Making use of the second rectangle, we end up with a S/N ratio of $\alpha A_1/\langle v_n \rangle^{\frac{1}{2}}$. We would like to make use of the full information coming from the known template waveform (i.e. we want to exploit $A_1/A_2 = \alpha$). To do so, we first delay the input signal $A_1 s(t)$, so that it becomes $A_1 s(t - \tau)$, then we superimpose it to the original $A_1 s(t)$, weighted by a factor β, and we take the output value at time τ to measure the amplitude A_1. Such an operation is depicted in Figure 4.12. In this case the signal amplitude (at the time of measurement τ) is $A_1(1 + \alpha\beta)$, while the noise contribution is $n(t) + \beta n(t + \tau)$. Because of the white noise hypothesis, we can consider $n(t)$ and $n(t + \tau)$ uncorrelated and the ergodicity ensures that they have the same root mean square value. Hence, the S/N ratio is:

$$\frac{A_1(1 + \alpha\beta)}{(1 + \beta^2)^{\frac{1}{2}} \langle v_n \rangle^{\frac{1}{2}}} \tag{4.5}$$

[3]The S/N optimisation presented here is intended to improve the performance of the trigger for signal amplitudes close to the noise. In this regime the linear approximation always holds.

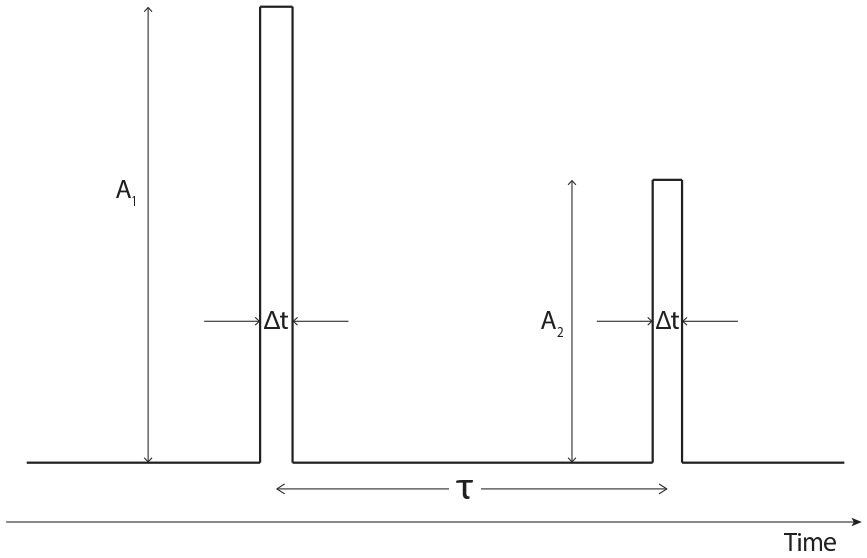

Figure 4.11: Signal composed of two rectangles of width Δt, time distance τ, and amplitudes A_1 and A_2. This example, as simple as it may look, accounts for the general case in which the signal has a shape known *a priori*. As a matter of fact, any waveform sampled with frequency τ can be seen as a sequence of rectangles with fixed amplitudes ratios.

The maximum of the expression 4.5 holds for $\beta = \alpha$, giving the maximum S/N ratio:

$$\frac{A_1(1+\beta^2)^{\frac{1}{2}}}{\langle v_n \rangle^{\frac{1}{2}}} \tag{4.6}$$

It is important to point out that the best S/N ratio happens to be at time τ. We can interpret the operation which results in the best S/N ratio presented in Equation 4.6 in terms of signal filtering. To do so, it is sufficient to see the outcome of the operation (leaving the weighting function $\beta s(t)$ unaltered) given a δ-like (or single, unit-normalized rectangle) input signal, and interpret it as a finite impulse response of the *Optimum Filter*, i.e. the filter which provides (at its output) the maximum S/N ratio given by the expression 4.6. Looking at Figure 4.12, the output would consist of two rectangles at time distance τ, the first of which has amplitude β and the second of amplitude 1. Such output is nothing but the original template waveform after time reverse operation.

Therefore, in the case of white noise only, the Optimum Filter of a signal $As(t)$ is simply $s(-t)$, or $\hat{s^*}(\omega)$ in Fourier representation. The evaluation of the amplitude A has to be carried out at the time position of the maximum of $s(t)$.

General, coloured noise case

In dealing with complex systems, it is hardly ever the case that one finds pure white noise. The first step we made was to define a filter tailored to a very specific signal shape, assuming

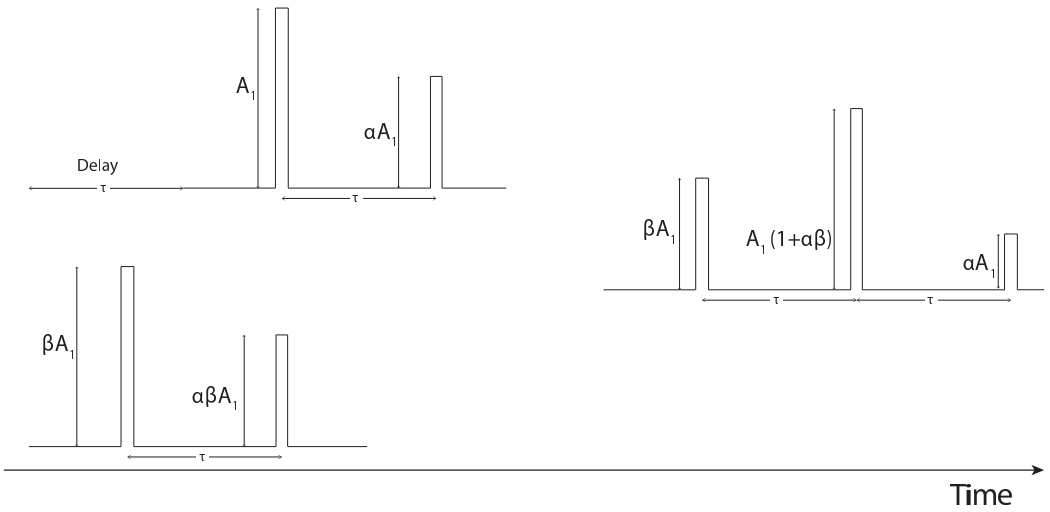

Figure 4.12: The input signal $A_1 s(t)$ is delayed by τ, while being superimposed to its weighted original form $\beta A_1 s(t)$. The resulting signal has a maximum at time τ of value $A_1(1 + \alpha\beta)$.

a featureless (white) noise. We want now to extend the application of the Optimum Filter to the general case of coloured noise.

We define again the signal as $As(t)$, where $s(t)$ is the signal template, and A the amplitude we want to reconstruct. Let τ_M be the time position of the maximum of $s(t)$ and $N(\omega)$ the noise spectral density. This time $N(\omega)$ can have any dependence on ω, but we still require the ergodicity hypothesis. We assume that there exists a transfer function $H(\omega)$, which applied to $As(t)$ gives, at the time τ_M the best output for A, where "best" has the same meaning as previously discussed in the white noise case.

We can write, given $As(t)$ as input, the filter output $y_F(t)$:

$$y_F(t) = \frac{A}{\sqrt{2\pi}} \int_{-\infty}^{+\infty} H(\omega)\hat{s}(\omega)e^{i\omega t} d\omega \tag{4.7}$$

The root mean square of the noise takes the form:

$$\langle v_n \rangle^{\frac{1}{2}} = \frac{1}{\sqrt{2\pi}} \Big\{ \int_{-\infty}^{+\infty} |H(\omega)|^2 N(\omega) d\omega \Big\}^{\frac{1}{2}} \tag{4.8}$$

We call ρ the S/N ratio at the time τ_M and take its squared value:

$$\rho^2 = A^2 \frac{\Big\{ \int_{-\infty}^{+\infty} H(\omega)\hat{s}(\omega)e^{i\omega\tau_M} d\omega \Big\}^2}{\int_{-\infty}^{+\infty} |H(\omega)|^2 N(\omega) d\omega} \tag{4.9}$$

The expression 4.9 is upper bounded and this bound corresponds to the desired $H(\omega)$. To

prove this we make use of the Cauchy-Schwarz inequality:

$$A^2 \frac{\left\{ \int_{-\infty}^{+\infty} H(\omega)\hat{s}(\omega)e^{i\omega\tau_M} d\omega \right\}^2}{\int_{-\infty}^{+\infty} |H(\omega)|^2 N(\omega) d\omega} \leq A^2 \frac{\left\{ \int_{-\infty}^{+\infty} |H(\omega)|^2 N(\omega) d\omega \right\} \left\{ \int_{-\infty}^{+\infty} \frac{|s(\omega)|^2}{N(\omega)} d\omega \right\}}{\int_{-\infty}^{+\infty} |H(\omega)|^2 N(\omega) d\omega} = A^2 \int_{-\infty}^{+\infty} \frac{|s(\omega)|^2}{N(\omega)} d\omega \tag{4.10}$$

In order to maximize the S/N ratio at the time τ_M we take the upper bound in 4.10 and interpret it as the application of a transfer function, $H(\omega)$ (the Optimum Filter), to the signal $s(\omega)$. $H(\omega)$ reads:

$$H(\omega) = K \frac{\hat{s^*}(\omega)}{N(\omega)} e^{-i\omega\tau_M} \tag{4.11}$$

where K is a (dimensioned) normalisation constant which may be defined such that the pulse amplitude is preserved at the output of the filter.

4.2.3 Filtering Detector A

We conclude the discussion about optimal filtering with a concrete example applied to one channel of CRESST-III. As a case study we pick Detector A, the detector that showed the best energy resolution among all the others. The ingredients needed to build the transfer function $H(\omega)$ of the filter are the signal template and the noise power spectral density of the channel. The former is obtained by averaging many pulses so that noise contributions are suppressed and the remaining waveform is a noiseless pulse representing the ideal detector response to a particle event. The latter is computed making an ensemble average of spectral contributions from a large set of randomly sampled waveforms containing no pulses. Both power spectral densities are shown in Figure 4.13. Extra care is needed when computing the Noise Power Spectrum. As already discussed in the previous sections, the discrete Fourier transform makes a periodic extension of waveforms, wrapping them around. The original data, being non periodic, introduces a discontinuity at the wrapping point.

Building the Noise Power Spectrum

The classical method to deal with the wrap-around of non-periodic signals is the weighting of the waveform with a window function. The goal of the window function is to force the samples of the waveform (in time domain) to smoothly go to zero at the two ends of the waveform, which are to be considered contiguous because of the periodic extension. This guarantees the applicability of the convolution theorem (Equation 4.3). The window function was chosen to be a tapered cosine (Tukey window), defined as:

$$w(x) = \begin{cases} \frac{1}{2}\left\{1 + \cos\left[\frac{2\pi}{r}(x - \frac{r}{2})\right]\right\}, & 0 \leq x < \frac{r}{2} \\ 1, & \frac{r}{2} \leq x < 1 - \frac{r}{2} \\ \frac{1}{2}\left\{1 + \cos\left[\frac{2\pi}{r}(x - 1 + \frac{r}{2})\right]\right\}, & 1 - \frac{r}{r} \leq x \end{cases} \tag{4.12}$$

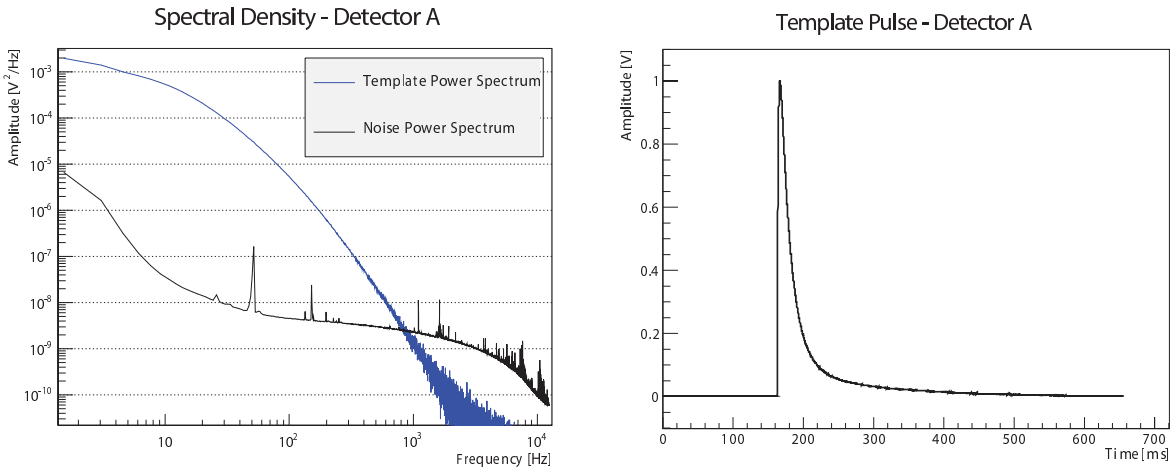

(a) (b)

Figure 4.13: Ingredients to build the Optimum Filter for the phonon channel of Detector A. (a) Spectral Power Density of the template pulse (blue) and Noise Power Spectrum of the same channel (black). Since the amplitude of the template pulse carries no information (it is normalized to 1 for convenience), its power spectrum is scaled to fit in the same picture of the Noise Power Spectrum. (b) Template pulse for the phonon channel of Detector A in time domain. The size of the window is 16384 samples, with a time base of 40μs, for a total duration of 655ms. The noise, being a stochastic function, is given in its power spectral density only.

An example of windowing of an empty trace from Detector A is shown in figure 4.14 ($r = 0.5$).

Starting from a large set of empty baselines (i.e. randomly sampled traces containing no pulses), the Noise Power Spectrum is computed as follows:

- The window function is applied to each empty baseline $n_i(t)$.
- The discrete Fourier transform $n_i(\omega_k)$ is computed for each windowed empty baseline.
- The Noise Power Spectrum $N(\omega_k)$ is computed as the ensemble average $\langle n_i(\omega_k) n_i^*(\omega_k) \rangle_i$.

The resulting Noise Power Spectrum of Detector A is shown in figure 4.13a.

Computing the Optimum Filter

After obtaining the noise characterisation (the Noise Power Spectrum) and the ideal detector response (Figure 4.13b), we can construct the transfer function $H(\omega)$ according to Equation 4.11.

To visually depict the complex $H(\omega)$, we can plot its modulus in frequency domain and its output when applied to the original template pulse (see Figure 4.15). The action

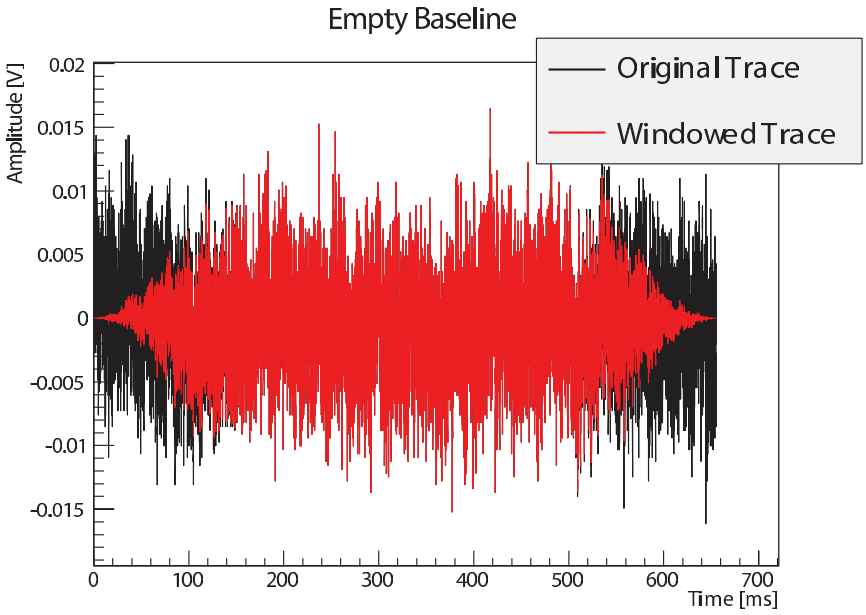

Figure 4.14: Randomly sampled empty baseline of Detector A (black). In order to force the two ends of the trace to the same value (zero) a tukey window is applied (the windowed trace is in red).

of the Optimum Filter is to weight all the signal components, in Fourier space, with their S/N ratio. In the specific case of Detector A, the 50Hz disturbance (coming from the power network) is filtered out, as are low (slow baseline fluctuations) and high (electronic interferences) frequency components, while the surviving components are those roughly in the range [10-100]Hz. The increase at the high frequencies (>4kHz) is an artefact due to the division by small numbers. The time domain representation of the filtered template pulse (Figure 4.15b) shows that the filter does not preserve the original pulse shape. The filtered template appears symmetric (to the contrary of the original pulse) and the 50Hz suppression creates "wiggles" in the signal.

Filtered Datastream

The method outlined allows us to manipulate the long datastream coming from the acquisition and to define a filter to get the best possible S/N ratio. An example of data, filtered with the transfer function in Figure 4.15, is reported in Figure 4.16, together with the time stamps of heater-induced events.

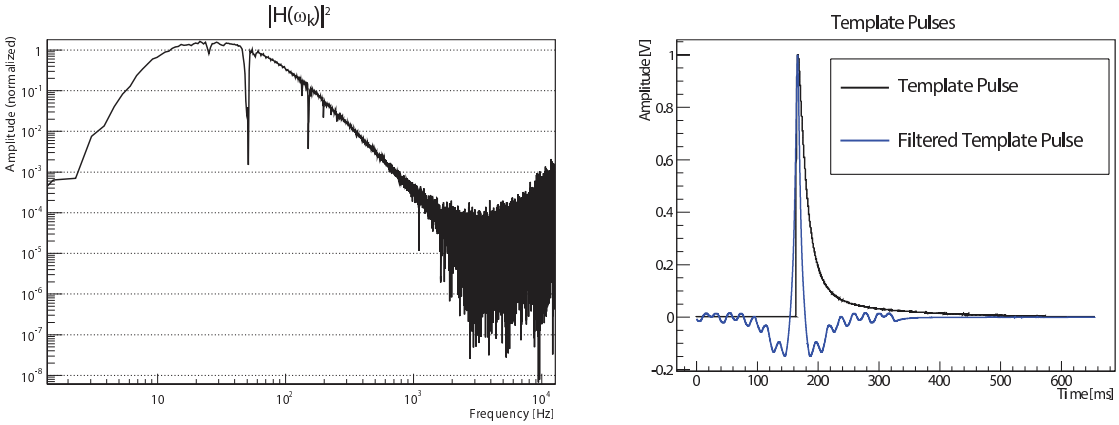

(a) (b)

Figure 4.15: Graphical representation of fundamental aspects of the Optimum Filter. (a) Squared modulus of the transfer function $H(\omega)$ showing the spectral shape of the filter. It roughly follows the spectral shape of the template pulse, suppressing the relevant features present in the noise (i.e. 1/f and 50Hz). (b) Template pulse before the filter (black) and after (blue). The "optimal" definition of the filter is such as to optimise the S/N ratio and there is no requirement about pulse shape preservation. Therefore, the filtered pulse has a very different shape from the original one.

4.3 A New Trigger for Very Low Thresholds

For triggering the continuous datastream, the scheme reported in Figure 4.8 is being reproduced from the detector output to the input of the comparator. The hardware trigger output is a logical signal in time coincidence with the triggered event, used to drive the acquisition to save the detector's output at the time of interest. In the case of the continuously recorded data, the trigger output is a list of positions in the stream where the filter output is above the defined threshold value.

The actual application to the data, its performance and drawbacks, including a comparison with the hardware trigger, are discussed in the following sections.

4.3.1 The Trigger Algorithm

With the filtered datastream available, the implementation of the comparator stage is straightforward. The trigger algorithm is nothing but a search over the entire datastream for samples exceeding the threshold value.

In order to properly identify a pulse, consisting of possibly several samples above threshold, the "natural" duration of the filter (i.e. the duration of the template pulse used to build the filter[4]) is used. The data was triggered according to the following steps:

[4]Pulses are stored individually in data window and all data windows have the same size. This size, the recordlength, is optimised for pulses in the region of interest. The recordlength used to process the

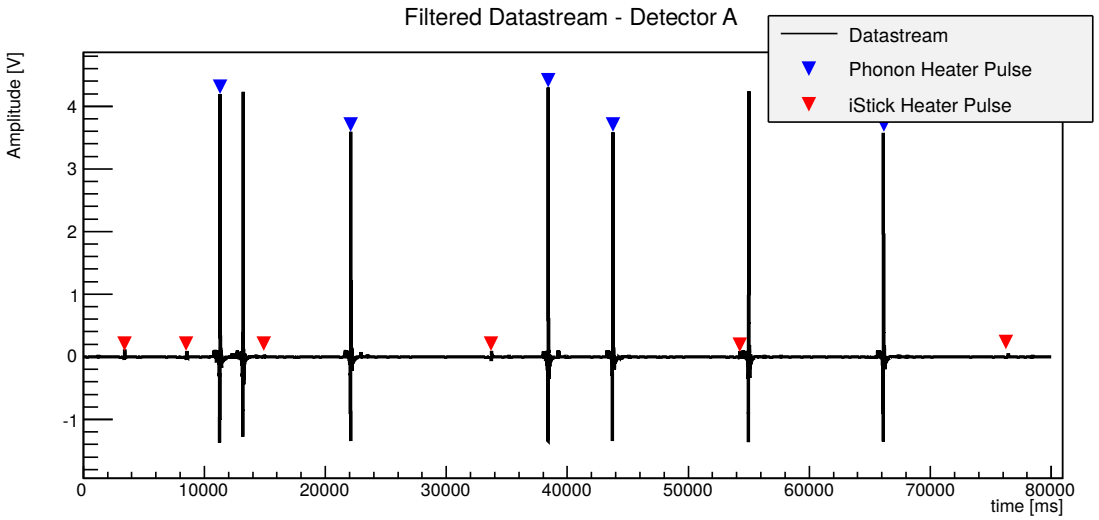

Figure 4.16: Sample of filtered datastream corresponding to the data shown in Figure 4.7. Compared to the original data, the baseline is set to zero and pulses have a shorter duration in time.

- The filtered datastream was scanned looking for samples above the threshold value.
- Any time a sample was found above threshold, a data window from that sample onwards was taken.
- The sample in the considered data window with the maximum value was assumed as the triggered pulse position. The data window is centred around that sample.
- The value of the maximum sample in the data window was assigned as the amplitude of the triggered pulse.
- The scanning for samples above threshold continued after the data window.

In Figure 4.17 an example of a triggered pulse with amplitude close to the threshold (amplitude $\sim$ 8.3mV and threshold value of 6.8mV) is shown.

The application of the filter is linear and it expects pulses whose shape scales linearly with their amplitude, so that the shape and the duration do not change as a function of the signal amplitude. Because of this, a trigger based on the Optimum Filter is ideal for cases where the signal amplitude is close to the noise fluctuations, as for the one in Figure 4.17: the filtered pulse exceeds the threshold for a certain number of samples and then the filtered datastream returns to fluctuate around the zero value of the baseline.

The presence of the "wiggles", visible in Figure 4.15b, can be problematic if the triggering is based solely on threshold. For those pulses whose amplitude is large enough,

data in the dark matter analysis is therefore a natural choice. Recalling the zero-padding process, the recordlength of the template pulse corresponds to half duration of the filter.

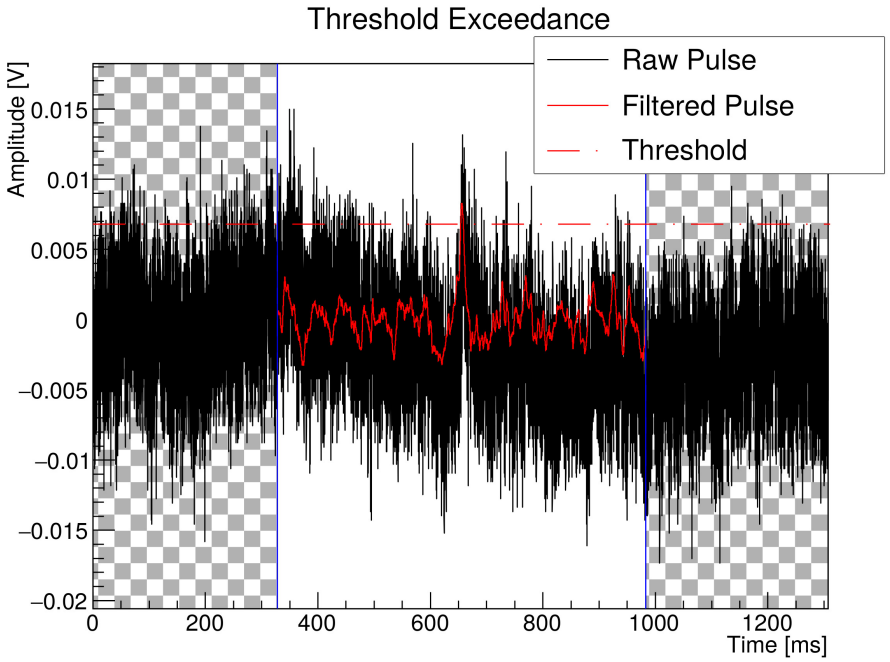

Figure 4.17: Depiction of the triggering of a pulse. The filtered datastream (solid red) is evaluated and whenever a sample exceeds the threshold (6.8mV, dashed red line) the trigger is fired. A data window of half the size of the filter duration is taken (datapoints between the blue solid lines) such that the maximum of the filtered data is placed in the middle position. The chequered area contains the samples affected by the wrap-around pollution and the corresponding filter output is not shown.

this distortion can fluctuate above and below threshold before the time of the pulse's maximum sample, leading to the misidentification of the pulse. The third point of the trigger algorithm guarantees that within the duration of the trigger, only the real pulse's maximum position is taken into account.[5]

The signal amplitude evaluation with the Optimum Filter fails as soon as the waveform to process does not follow the expected shape, which is the case for saturated pulse as in Figure 4.18. From the picture, it is apparent that the shape of the filtered pulse is distorted (it is not symmetric) and the resulting pulse amplitude is not to be trusted. This kind of inconvenience is encountered with pulses whose amplitude, wrongly evaluated, is large enough to be triggered. Therefore, for saturated pulses, the truncated Template Fit is the only reliable amplitude evaluation, but this does not prevent the trigger based on the Optimum Filter to correctly tag them as particle interactions, since they are well above

[5]The Optimum Filter is a non-causal filter, meaning that early samples of the output can depend upon later samples. This can be seen in Figure 4.15b: The original pulse develops after 160ms from the beginning of the considered data window. The filtered pulse, on the contrary, develops since the very beginning. The total number of samples, before the actual pulse's on-set, which is affected by the presence of the pulse cannot be larger than the filter duration.

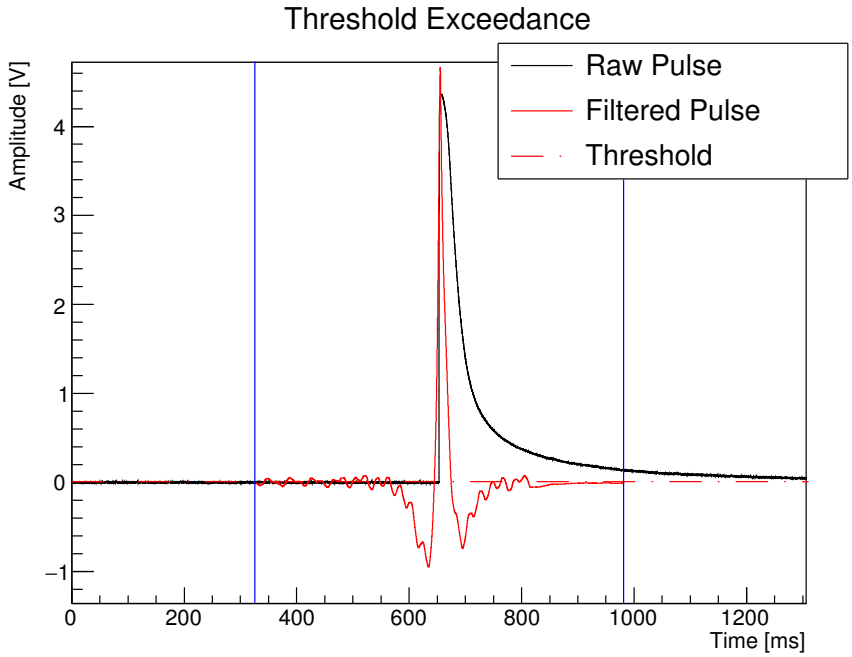

Figure 4.18: Triggering of a saturated pulse. The energy deposition corresponding to this pulse is large enough to drive the TES sensor out of linear regime, showing the saturation effect on the pulse (black line). The distortion due to the saturation is also visible in the filtered pulse, which is asymmetric.

threshold.

The most extreme situation is when the pulses under investigation are saturated and their duration is much longer than the filter duration. An example of such a pathological pulse in reported in Figure 4.19. The very long decaying tail of the pulse causes the trigger to fire twice in a row. Even though such an effect is undesirable, decaying baseline can be easily identified and rejected.

4.3.2 Filter Resolution

The width of the baseline distribution at the output of the filter is the crucial parameter which sets the performance of the trigger, and ultimately limits the threshold. For low energy interactions in CRESST detectors, the width of the baseline distribution corresponds to the detector resolution (sometimes called "zero-energy resolution"), since electronic noise is the dominant uncertainty contribution. By baseline distribution we mean the random noise fluctuations of the detector output in absence of a signal. In order to evaluate the resolution of the filter, we try different ways to estimate the baseline resolution.

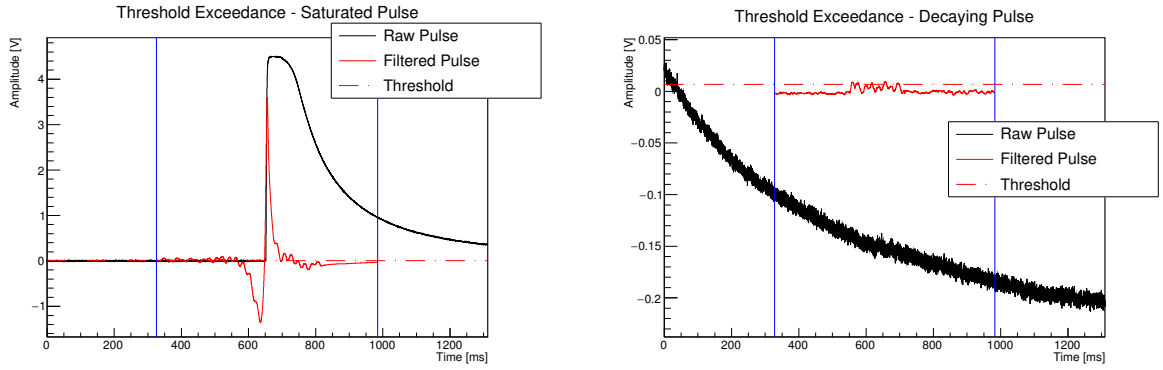

(a) (b)

Figure 4.19: Example of a pulse unsuitable for being processed with the filter described in this chapter. (a) Saturated pulse before the filter (black) and after (red). (b) The long tail of the pulse in the left Figure and the corresponding filtered data. Two main features are apparent, namely the pulse shape and the long decaying tail. Due to saturation, the pulse shape does not reproduce the one of the template pulse used to build the filter. As a direct consequence, the filtered pulse looks very different from the expected one, as in Figure 4.13b, and the amplitude evaluation is invalid. The original pulse does not decay completely within half duration of the filter (blue vertical lines) and its tail extends much further, causing the trigger to fire after several hundred microseconds (Figure 4.19b).

Random sampling

The first approach to determine the baseline resolution was carried out according to the following:

- A large ensemble of empty baselines was taken.
- The Optimum Filter was applied to each empty baseline.
- The sample in the middle from each baseline was taken as representative.

The distribution of the representative samples for Detector A is shown in Figure 4.20.

Superimposed signal

Another way to evaluate the resolution of the filter consists of superimposing a template pulse on an empty baseline and then computing the signal amplitude as if it were a real particle event. If a pulse of a certain amplitude is superimposed to a large set of empty baselines, then the resolution can be evaluated as the amplitude distribution from the filter's output of each waveform. The procedure used is:

- A large ensemble of empty baselines was taken.
- The template pulse of a given amplitude was superimposed to each empty baseline.

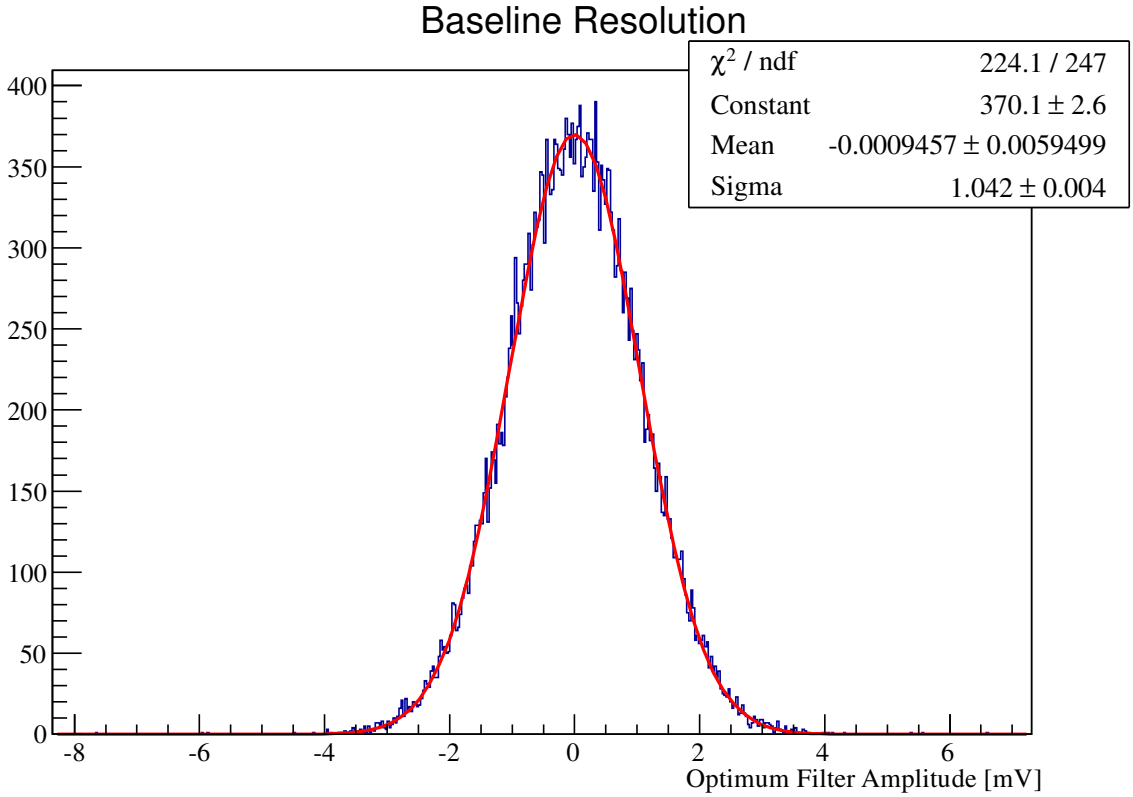

Figure 4.20: Baseline resolution of the phonon channel of Detector A, computed using the Optimum Filter. A large set (31085) of empty baselines from the training set, randomly acquired during operation, has been filtered. One sample from each empty baseline is taken as entry of the histogram. The data is well-fitted to a gaussian distribution. The resulting resolution (σ) is 1mV.

- Each waveform was processed with the Optimum Filter.
- The maximum amplitude from each filtered waveform was taken as the signal amplitude estimator.

A comb-like energy spectrum had been simulated using five different amplitudes: 6.8mV, 25mV, 45mV, 60mV, 80mV. The very same list of empty baselines employed in the random sampling method had been split (and shuffled) into five lists, each of which was used to simulate one of the five listed amplitudes. The spectrum after the application of the filter is shown in Figure 4.21. The results from the two methods are summarized in Table 4.1. The quality of the amplitude reconstruction and the resolutions at the different simulated amplitudes are the relevant aspects. The former are in agreement with their expected values at worst at the 1‰, the latter do not scatter more than 1% away from the average value 1.03mV. This implies that the two methods are substantially equivalent. The main focus of this work is the trigger behaviour at threshold, where noise fluctuations are dominating,

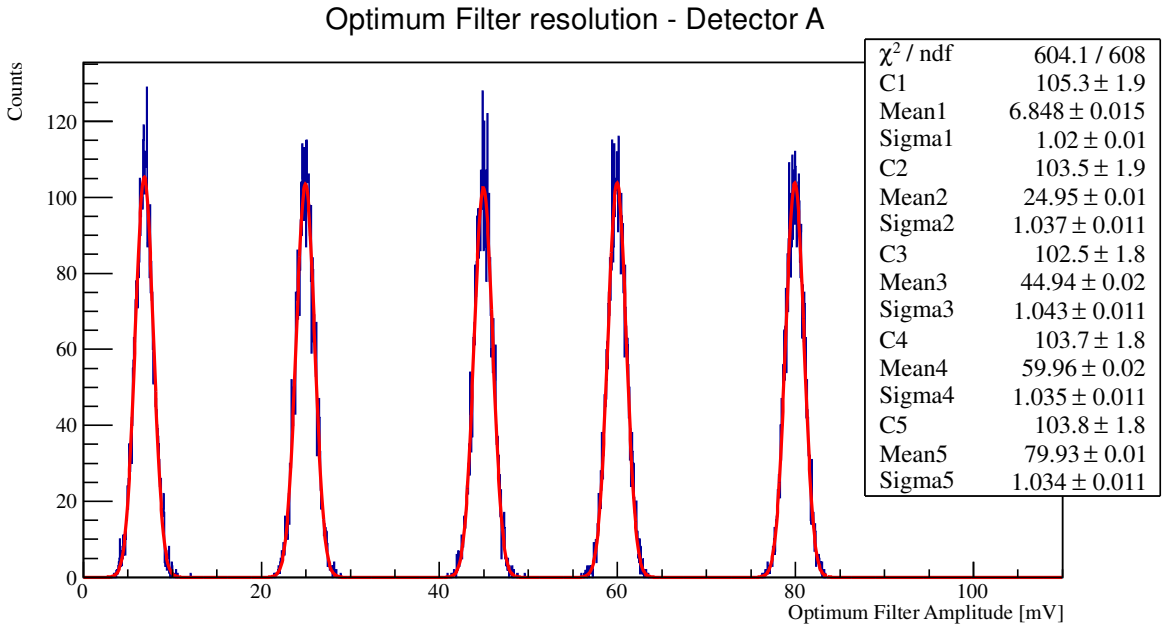

Figure 4.21: Determination of the filter's resolution using empty baselines with superimposed pulses. Five amplitudes were simulated and the corresponding filter's output is shown. The spectrum was fitted to five (independent) gaussian distributions.

Simulated Amplitude mV	**Reconstructed Amplitude** mV	**Resolution** mV
0	-10^{-3}	1.04
6.8	6.84	1.02
25	24.95	1.03
45	44.94	1.04
60	59.96	1.03
80	79.93	1.03

Table 4.1: Evaluation of the filter's resolution. The first entry in the table was computed using the random sampling method (Sec. 4.3.2, Figure 4.20), the other five using superimposed signals (Sec. 4.3.2, Figure 4.21). The inputs from Detector A are the template pulse and the ensemble of empty baselines. The set of empty baselines used for the evaluation of the first entry was divided into five sets (randomly sorted), each of which was used to simulate one of the five non-zero simulated amplitudes.

therefore, the random sampling method is favoured, being the exact reproduction of the detector's output in the absence of any signal.

Maximum search vs amplitude at τ_M

The Optimum Filter offers the best amplitude evaluation for a signal at its maximum at the (known) time τ_M (see Equation 4.11). It should be noted that the trigger described in this chapter works in the opposite way: the maximum output is taken as the amplitude estimator and τ_M determined after the finding of the maximum sample. A way to visualize the problem comes from the comparison of the two methods used to characterize the filter's resolution:

- Random sampling: the mid sample of empty baselines was taken as amplitude evaluation, implying that the mid of the window is τ_M and the amplitude determined at that data point, in accordance with the Optimum Filter prescription.
- Superimposed signal: the data window superimposed to a signal of given amplitude was scanned looking for the maximum, implying that τ_M was determined from the maximum amplitude.

While the first method outputs a 0mV average amplitude with a gaussian distribution whose σ is determined by noise fluctuations, the same would not apply if the empty baselines were processed with the maximum search algorithm and no superimposed pulse. The maximum search would always be biased by upward noise fluctuations and never by the downward ones. Being the maximum search the algorithm effectively used to trigger the data, it is necessary to study its validity. We chose to repeat the maximum search characterisation using, this time, amplitudes across the noise level. Three amplitudes (0.6mV, 1.2mV, 3.4mV and 6.8mV, given that one standard deviation of the noise is $\sim$1mV) were simulated over the ensemble of empty baselines and the corresponding maximum search outputs are shown in Figure 4.22. From Figure 4.22 we can see how the maximum search is totally dominated by the noise upper fluctuations, if the signal amplitude is in the order of the noise fluctuation (amplitudes 0.6mV and 1.2mV are indistinguishable from the 1mV noise). The choice of the threshold is naturally made not to pollute the data with noise fluctuations. In the case of Detector A the threshold was set to 6.8mV, which is a sufficient amplitude to guarantee that the maximum search algorithm outputs a reliable value, as it can be inferred from the gaussian shape of 6.8mV in Figure 4.22, which has the right mean value and the expected resolution.

4.3.3 Energy calibration

The CRESST setup was exposed to a ^{57}Co source for $\sim$420h in order to calibrate the detectors. We use here calibration data to extrapolate the factor to convert signal amplitudes from volts into energy units, and eventually express the achieved results in terms of physical units.

The energy spectrum obtained during the calibration campaign is shown for the case of the phonon channel of Detector A in Figure 4.23. In the plot both the test (in red) and particle induced (black) pulses are depicted. We use the test pulses-induced spectrum

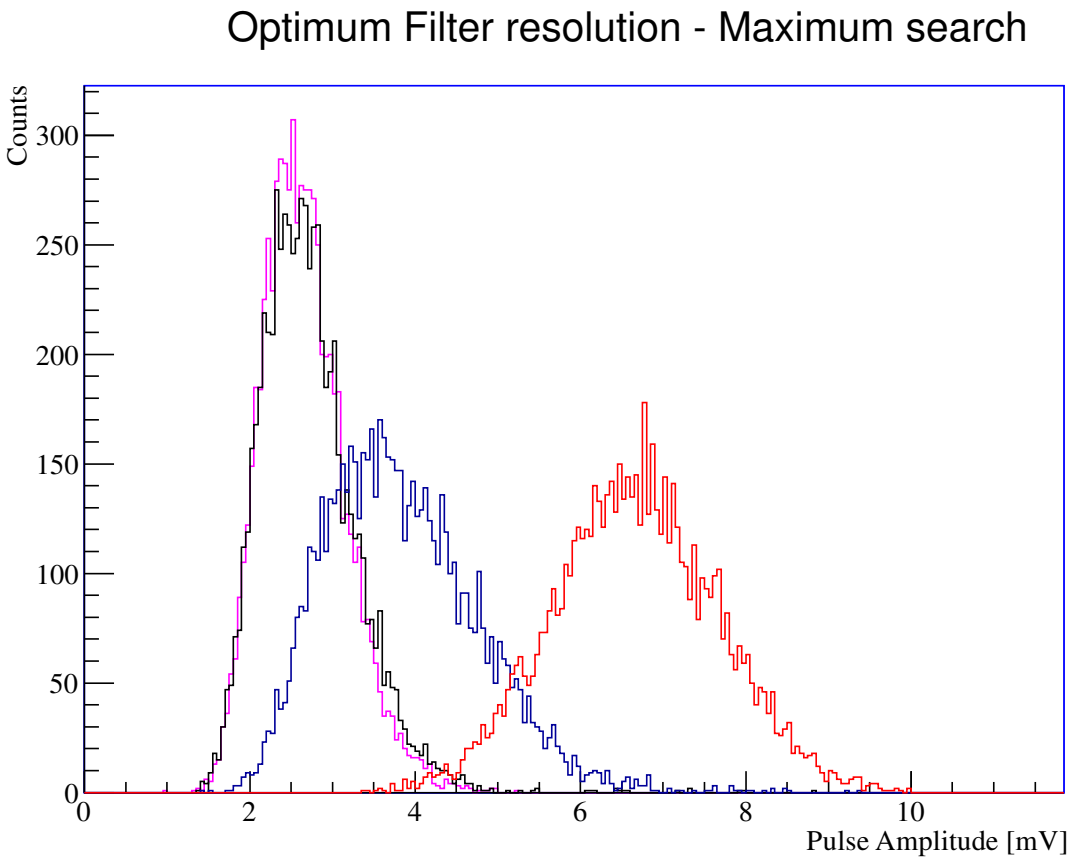

Figure 4.22: A spectrum of three amplitudes was generated and processed with the maximum search algorithm to evaluate the amplitude. The resulting spectrum is shown for four amplitudes: 0.6mV (black), 1.2mV (pink), 3.4mV (blue), and 6.8mV (red). The 6.8mV amplitude is the one which reproduces a gaussian output. The lower the amplitude, the more the distribution deviates from a gaussian shape, being the signal amplitude below the noise.

to determine the detector's response (which is typically non-linear) over the interesting dynamic range, and then the energy peaks induced by the calibration source to set the absolute energy scale. The mapping of the injected energy into corresponding pulse amplitude is shown in Figure 4.24. A fifth order polynomial is fit through the points is order to evaluate the energy response at all amplitude values. The absolute energy is assessed by scaling the mapping in order to match the acknowledged energy peak to its nominal value (red scale at the right of the plot). In this chapter we are interested in signals of very small amplitudes, close to the minimum identifiable output from the detector. In this regime the conversion from signal amplitude to energy is given just by the linear term of the polynomial fit in Figure 4.24. In the case of Detector A the conversion factor is 4.28keV/V.

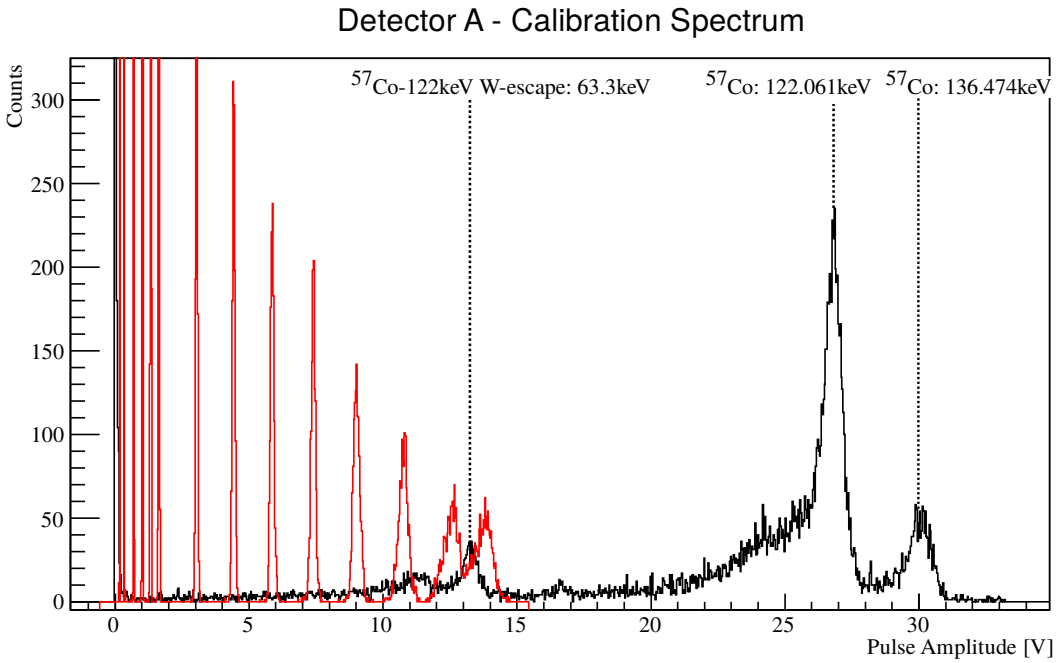

Figure 4.23: Energy spectrum measured by the phonon channel of Detector A during ^{57}Co calibration campaign. The energy spectra of test pulses (red) and particle induced pulses (black) are overlayed. The two most prominent peaks are caused by the 122keV and 136keV gammas emitted by the source. The third most prominent peak (63.3keV) is due to the escape of the W X-rays ($K_{\alpha 1}$ and $K_{\alpha 2}$) and it can be used for calibration since it appears in the range of the test pulse spectrum. Its amplitude is at 13.2V. All amplitudes are computed using the truncated template fit to account for saturation effects.

4.3.4 Comparison with the hardware trigger

A direct evaluation of the signal-to-noise in the hardware trigger is not possible, because the signal filtered by the electronic board is not acquired. We try to model it according to the manufacturer's specifications. The filter is said to be equivalent to a sixth order Bessel filter and the cut-off frequency set to 150Hz. In Figure 4.25 the relevant features of the software implementation of such a filter are shown. The comparison with the Optimum Filter is carried out evaluating the baseline resolution of the Bessel filter. The application is identical to the random sampling method introduced before. The effect in time domain of the application of the two filters is plot in Figure 4.26a. The baseline distributions of the two filters are shown in Figure 4.26 together with the distribution without any filtering. The data in the plot are fitted to a gaussian distribution. The results from the fit are summarized in table 4.2.

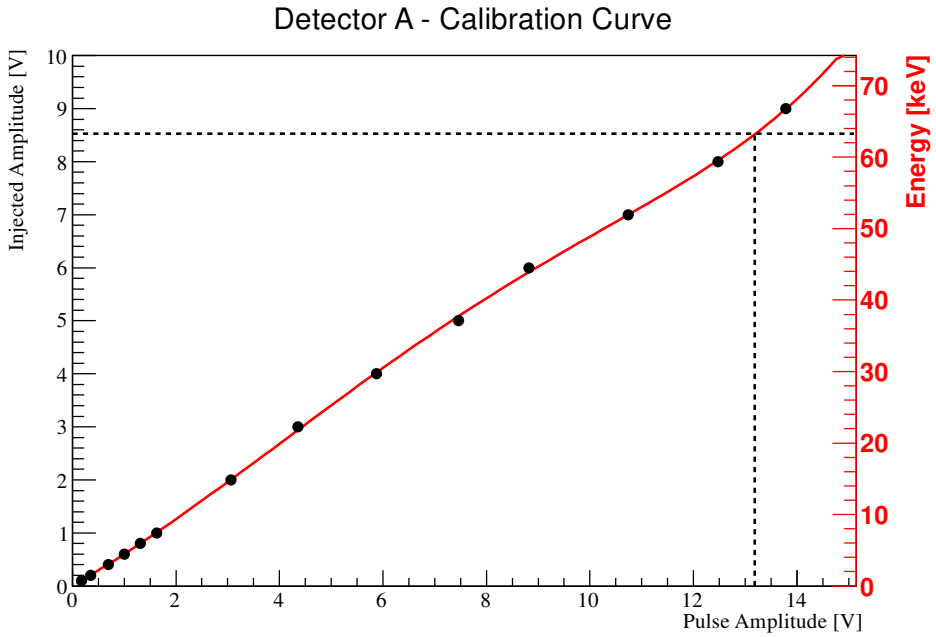

Figure 4.24: Calibration curve for the phonon channel of Detector A. The dashed lines mark the amplitude used to determine the absolute energy scale (63.3keV peak). Test pulses are injected in order to sample the sensor's response at different energy depositions (and over time). A fifth order polynomial interpolation is used to determine the response at all energies, accounting for non-linearities. The conversion from injected test pulse energy into keV is then just a linear scaling which assigns the identified peak to the nominal value. The evaluation of the polynomial at the amplitude of the W escape peak is 8.38V (left y-axis), so that the conversion from the left to right axis is 7.55keV/V. The linear term of the polynomial is (0.527±0.006)V/V in left y-axis units and the resulting sensitivity at low energies is (4.28±0.04)keV/V.

4.3.5 Comparison with the Template Fit

Although the template fit is never used in the context of the trigger, it is interesting to compare it with the Optimum Filter to see the improvement of the pulse amplitude reconstruction. Once again, we are interested in the uncertainty in determining a null amplitude signal to evaluate the baseline noise. We run the template fitting algorithm on the same set of empty baselines used for all the characterisation, an example of this fitting is reported in Figure 4.27a. The distribution of evaluated amplitudes is the measure of the baseline noise affecting the amplitude reconstruction. The distribution is shown in Figure 4.27b.

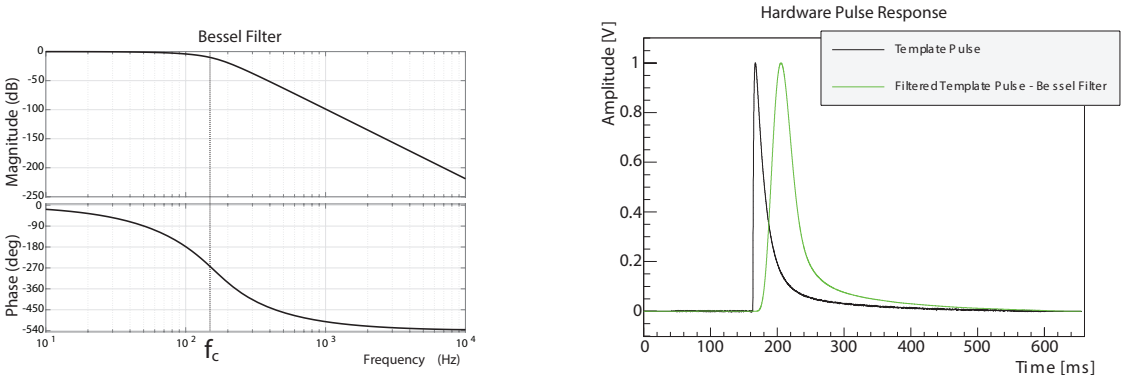

(a) (b)

Figure 4.25: Frequency response of the bessel filter and its effect on the standard pulse. These plots are to be compared with the ones made with the optimum filter. (a) Frequency response of the (simulated) hardware filter. Top is the magnitude, bottom the phase response. (b) Template pulse before (black) and after (green) the filtering process.

	Mean value [mV]	**Resolution [mV]**
Raw trace	-0.6	3.6
Bessel output	$-6 \cdot 10^{-3}$	2.3
OF Output	-10^{-5}	1.04

Table 4.2: Comparison of the filters' resolutions. The data for the Optimum Filter are taken from table 4.1.

4.3.6 Trigger efficiency

As already remarked in this work, the precise knowledge of the detector's threshold is crucial to obtain the energy spectrum at the lowest accessible energies. This is particularly important for CRESST detectors since the phonon channel gives a direct measurement of the energy. The trigger efficiency is, in principle, an ideal step function (see the comparator stage in Figure 4.8, totally equivalent to the software implementation), meaning that all signals above the threshold value are triggered, and all those below are not. The finite baseline noise complicates the picture, making the actual trigger efficiency the convolution between the step function, the detector's output, and the filter's response function.

The evaluation of the trigger efficiency follows two different ways, depending on whether we want to study the software trigger, presented in this chapter, or the hardware trigger.

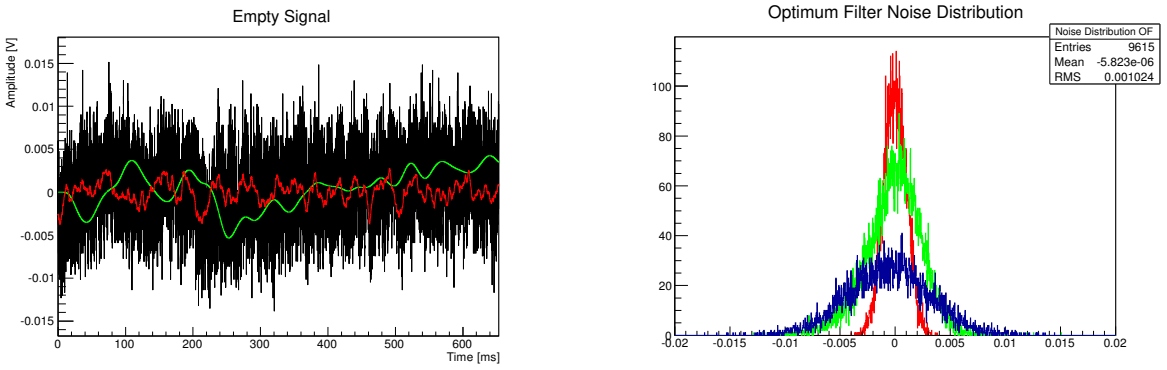

(a) (b)

Figure 4.26: Evaluation of the noise fluctuation at the output of the Bessel filter. (a) Comparison of the bessel filter with the optimum filter. The original empty trace (black) is filtered with the Optimum Filter (red) and the bessel filter (green). The original signal does not contain a pulse, hence the filtered traces are the noise fluctuation at the output of the corresponding filter. (b) Distribution of the samples taken from the large set of empty baselines. In blue is drawn the raw noise distribution, in green the Bessel filtered noise and in red the Optimum Filter noise.

Hardware trigger efficiency

We use the pulser to deliver several test pulses with amplitudes around the threshold value. Any time a test pulse of a given amplitude is delivered, we look for a time coincidence of the trigger and adopt the ratio of triggered pulses to delivered pulses of that amplitude as the trigger efficiency. Because of transient noise variations, a slight cut on the baseline root mean square was applied, in order to get rid of anomalous noise conditions.

Software trigger efficiency

The software trigger can be evaluated by only making use of simulated pulses. A spectrum of several amplitudes of template pulses are randomly superimposed to the datastream. The trigger algorithm is run normally and at the end we compute the fraction, for each energy, of triggered superimposed pulses. The very same cut on the baseline root mean square was applied as in the case of the hardware trigger threshold efficiency evaluation.

Comparison

In both cases what we look for is the function $f(E)$ representing the probability for an event of energy E to be triggered. Assuming a gaussian noise distribution, an energy threshold E_{th} and energy resolution σ, the trigger efficiency can be modelled with the expression in Equation 4.13:

$$f(E) = \frac{1-p_1}{2}\left[1 - erf\left(\frac{E-E_{th}}{\sqrt{2}\sigma}\right)\right] + p_2 \tag{4.13}$$

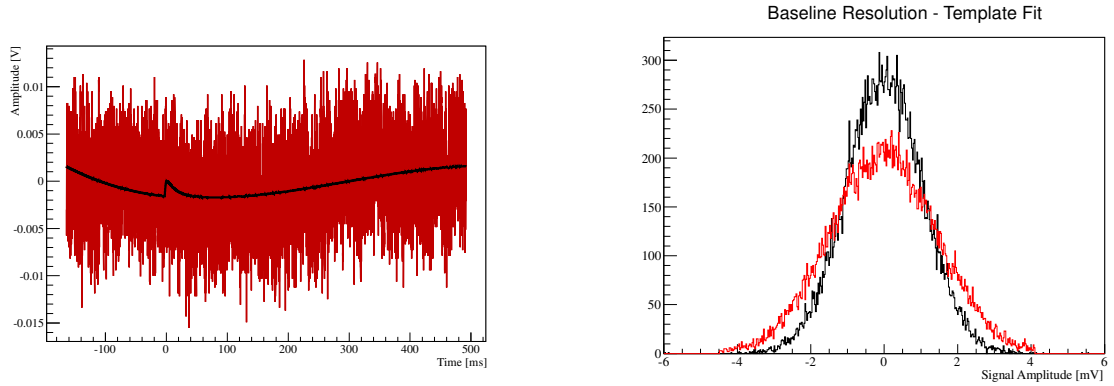

(a) (b)

Figure 4.27: Evaluation of the resolution at zero energy of the template fit. (a) Extrapolation of the amplitude via Template Fit. (b) Distribution of recostructed amplitude using the template fit (red) and the corresponding Optimum Filter evaluation for comparison (black). The former is well described by a gaussian function with mean 0V and σ 1.42mV

In Equation 4.13 p_1 represents the probability for a random noise fluctuation to exceed the threshold E_{th} at the time of the simulated/injected pulse. p_2 accounts for a non-100% efficiency at large amplitudes due to dead time and cut efficiency, which causes pulses well above threshold not to be considered. The results of the trigger efficiency evaluation are shown in Figure 4.28. The energy threshold of Detector A, achieved with the new scheme

Trigger	**Threshold [eV]**	**Resolution [eV]**	p_1	p_2
Software Trigger	28.93±0.06	4.51±0.06	0.006	0.094
Hardware Trigger	51.27±0.73	10.44±0.83	0.028	0.1

Table 4.3: Results of the trigger efficiency fit

proposed in this chapter, leads to a result which is 1.7 times better than what is obtained with the hardware trigger of the standard CRESST acquisition system. In addition, the resolution of the Optimum Filter is improved by a factor of ~ 2.3 compared to the bessel filter. In σ-units, the software threshold was set at 6.4σ above the noise level, while the hardware trigger was at just 4.9σ. Setting a threshold at a larger value (in σ-units) resulted in the p_1 parameter being reduced to 20% of the one for the hardware trigger. The effect is then a reduced amount of fake triggers induced by random noise fluctuations.

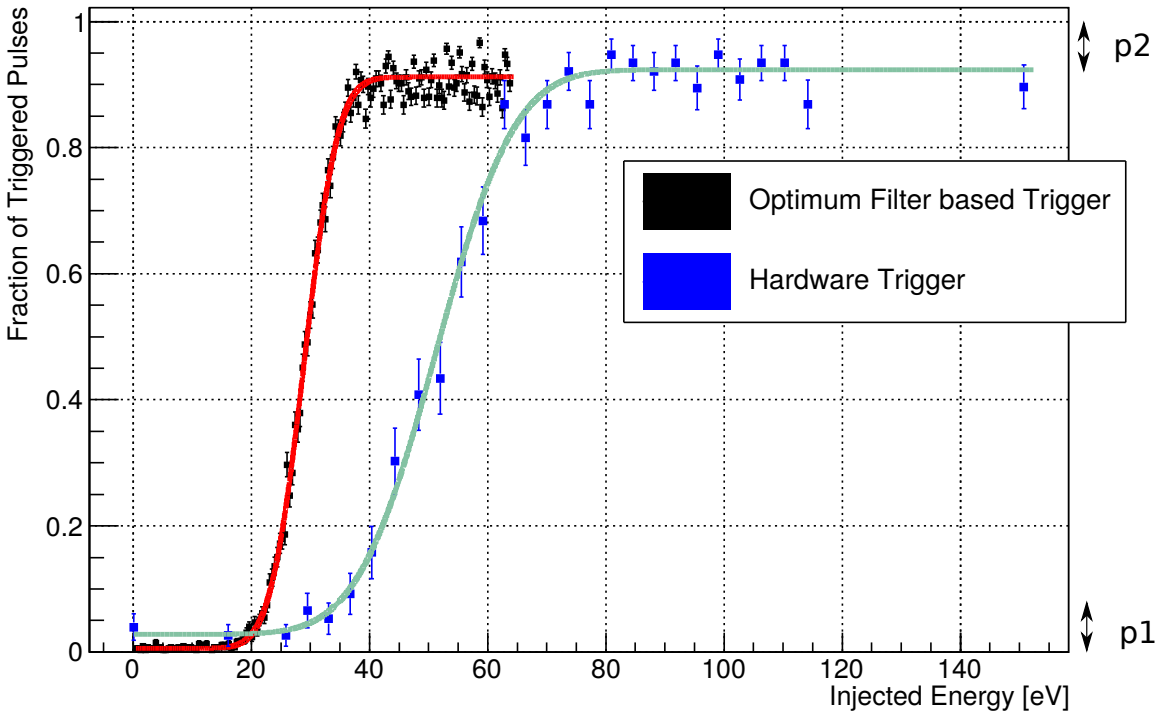

Figure 4.28: Trigger thresholds of the phonon channel of Detector A. The resolution (σ) obtained with the Optimum Filter based trigger is (4.51±0.06)eV, in agreement with what is expected from the Optimum Filter resolution (4.45eV). The resolution of the bessel filter (obtained with the simulation, 9.84eV) is also in agreement with what measured in hardware (10.44±0.83)eV. Color coded in red is the fitted efficiency for the software trigger and in turquoise, the one for the hardware trigger.

4.4 Impact on dark matter sensitivity

The newly developed data acquisition, together with the Optimum Filter based trigger, allowed for an energy threshold improved by roughly 43% of the one achieved with the conventional acquisition and data processing. We present here the impact of such improvement on the dark matter sensitivity for the CRESST-III experiment.

At the time of writing the official CRESST-III analysis is not yet finalised and the full dataset still not accessible[6]. In order to investigate the sensitivity without making use of the full dataset we proceeded in three steps:

- We made use of a reduced amount of data to derive a data-driven background model.

[6]CRESST results are usually derived by means of a blind analysis. First the analysis specifications are determined using a restricted dataset, the training set, and then the analysis is blindly applied to the full dataset in order to avoid an analysis bias in the results. See [88] for details.

- The background model was used to implement a montecarlo simulation for a large number of identical experiments, each of which with the desired exposure (50kg·day).
- For all simulated experiments the exclusion limit was computed. The final result is an exclusion contour that contains 68% of the exclusion limits (1σ C.L.).

The three steps were applied considering the two cases of an energy threshold of 28.93eV (the one of the trigger developed in this work) and 51.27eV (conventional acquisition trigger) to have a direct comparison.

4.4.1 The background model

The data used to derive the background model is shown as a light yield vs energy plot in Figure 4.29. The bands describing electron and nuclear recoils were determined with a dedicated neutron calibration, see Appendix B for details. The background is largely contained in the e/γ band and it does not show features. In order to develop a montecarlo we assume that the background is due to electron recoils only and that events in the nuclear recoil bands are caused by a leakage into the region of interest. The leakage is, in turn, determined by the broadening of the bands at the lowest energies, a regime in which active background rejection is not possible.

Because of the absence of features for most of the background down to 300eV (see Figure 4.30) we model it as constant (around 3 counts/keV/kg/day). The montecarlo will then generate random experiments (one light yield plot for each) with an electron/gamma background created accordingly.

4.4.2 Dark matter sensitivity

The dark matter sensitivity is computed applying the Optimum Interval method described in Section 3.4.4 to each simulated dataset. As a result we show the upper and lower contours referring to a 1σ C.L.

At first we need to define for which range of dark matter particle mass the Yiellin method has to be applied. Indeed we are interested at the lowest experimentally accessible masses. Recalling Equation 2.3, we can determine the minimal mass that a dark matter particle in the galactic halo needs to have in order to induce a nuclear recoil above threshold. Already at this point we can see how a lower threshold is beneficial to optimise the sensitivity to the low mass region of the parameter space. The lower the threshold, the lower the mass of the lightest detectable dark matter particle. For the case of the hardware trigger threshold (51.27eV) the search stops at 246MeV/c^2. The Optimum Filter based trigger extends the reach down to 184MeV/c^2. The comparison of the sensitivities in the two considered cases is reported in Figure 4.31.

In addition to the lower dark matter particle bound, the new threshold improves the sensitivity below 1.1GeV/c^2 to a maximum of around three orders of magnitude at 246MeV/c^2, where the conventional trigger stops being sensitive. The discussion based on montecarlo simulations served the purpose to illustrate the sole role of the energy

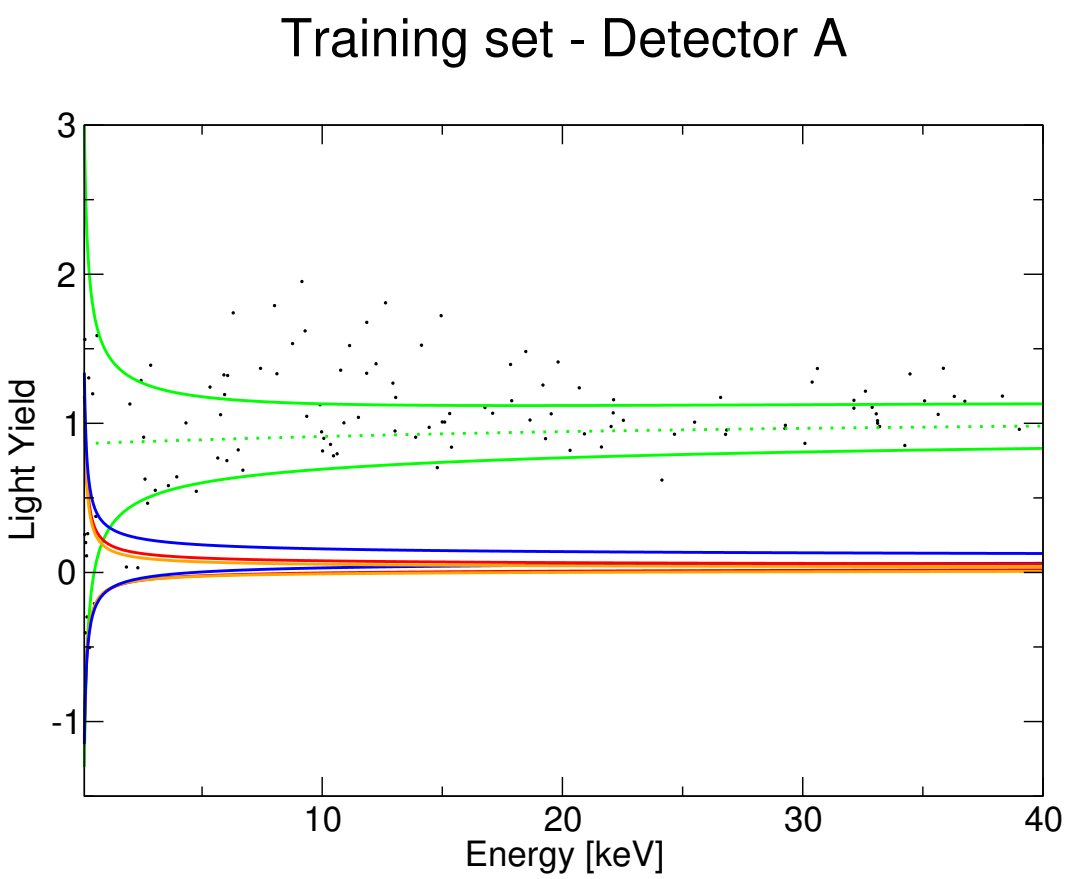

Figure 4.29: Training set data of detector A in the Light Yield plot. The solid lines represent the 90% upper and lower boundaries for each class of events (colour-coded in green, blue, red and orange are electron recoils, nuclear recoils on oxygen, nuclear recoils on calcium and nuclear recoils on tungsten respectively). The derivation of the bands description is reported in Appendix B.

threshold and what could be the maximum improvement of CRESST-III in the light of what is presented in this chapter. Two assumptions make the sensitivities in Figure 4.31 too optimistic. First of all detector A is the one that achieved the lowest threshold of all, whereas the simulated 50kd·day imply that all detectors have the same energy threshold. The second assumption is the background model. A simple constant description is clearly too simplistic given the feature present below 300eV in Figure 4.30. The large number of events at low energy in the spectrum is of unknown origin and currently under investigation. A discussion about possible interpretations of these events goes beyond the scope of this work and we limit ourselves to consider it a background.

In order to get a more realistic idea of the achievable sensitivity of CRESST-III we computed the exclusion limit on the actual training set. The result suffers from the limited exposure, but takes into account the real features of the background. In Figure 4.32 the exclusion limits computed considering the two thresholds are shown. Despite being less

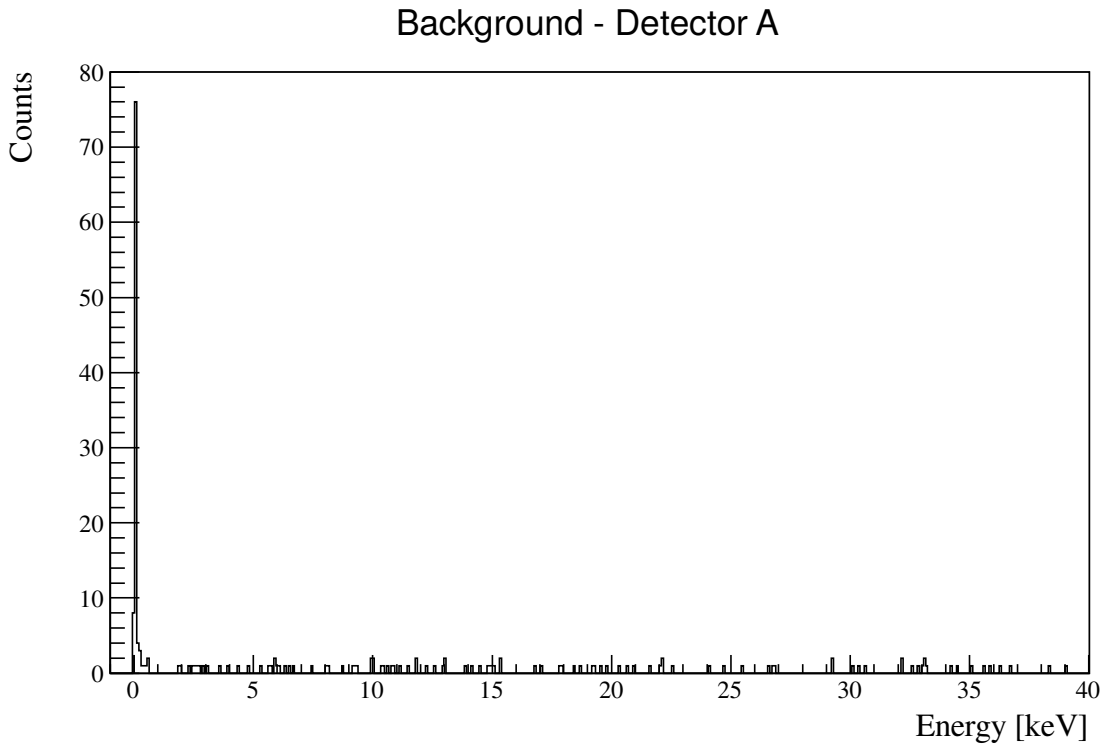

Figure 4.30: Energy spectrum measured by detector A. It is mainly due to electron recoils (see Figure 4.29).

impressive than what is shown in Figure 4.31, the limit computed on the real data still shows a substantial improvement when determined with the Optimum Filter triggered data. In particular, being solely a consequence of kinematics, the reach to dark matter particles of mass 184MeV/c^2 is preserved.

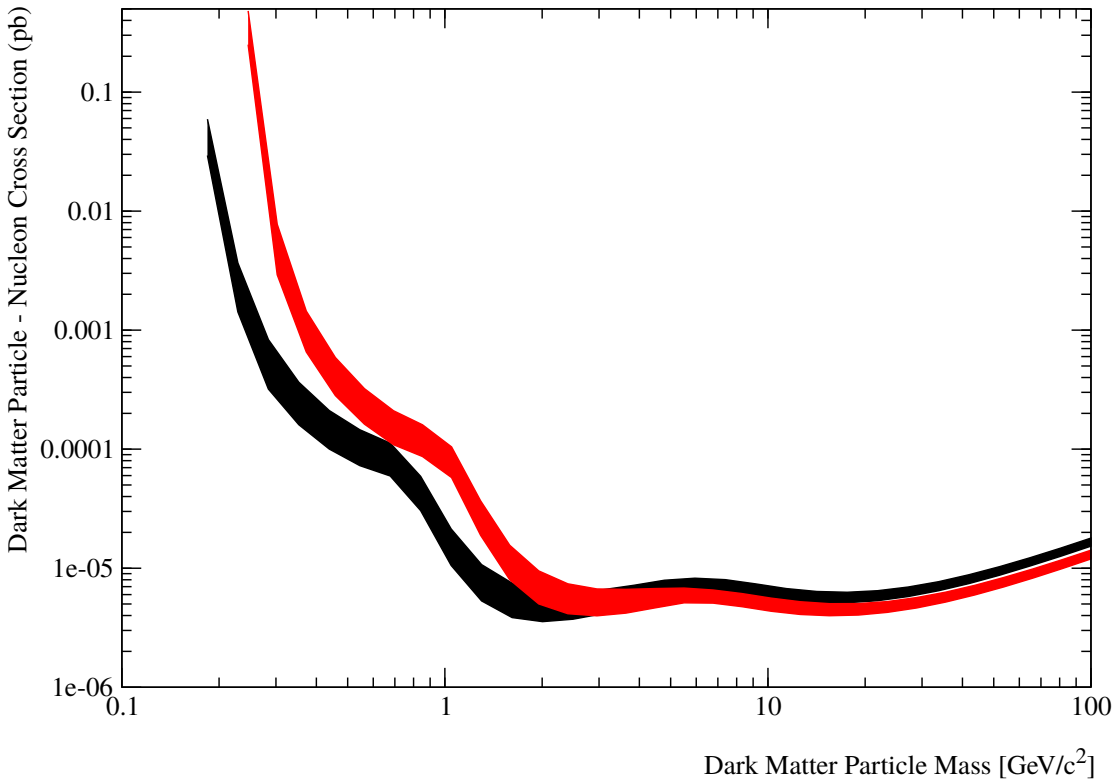

Figure 4.31: 1σ C.L. exclusion limits for 10,000 montecarlo generated experiments, based on the energy spectrum in Figure 4.30. The simulated exposure is 50kg·day. In black is drawn the exclusion obtained with the software trigger threshold, in red with the hardware trigger threshold.

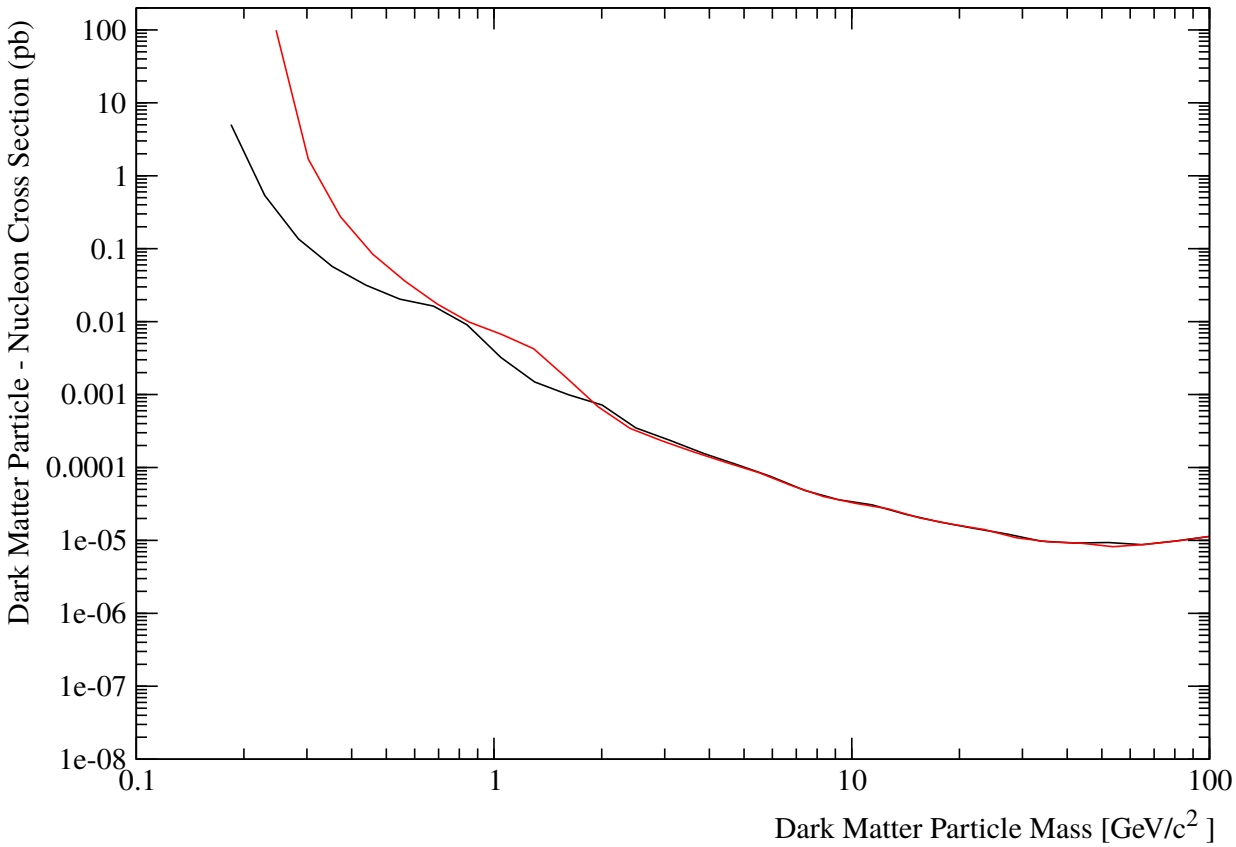

Figure 4.32: Exclusion limits computed with the Yellin Optimum Interval method on the training set of detector A. Colourcoded in red is the limit corresponding to the hardware threshold. In black the limit with the software trigger threshold.

Chapter 5

Test measurement of a TES sensor with modulated BIAS

The results presented in Chapter 4 are based on the continuous DAQ described in Section 4.1. Such a system does not provide any active thermal stabilisation necessary for the operation of cryogenic detectors. Therefore, the operation of the detectors in CRESST-III and their continuous acquisition is possible thanks to the parallel operation of the continuous DAQ and the standard CRESST acquisition system. The latter, as described in Section 3.3.4, provides on-line monitoring and temperature control to guarantee that the TES sensors are kept in their working points during the measurements. In this chapter, an innovative read-out scheme is proposed, with the intent to make the thermal stabilisation independent from the DAQ of the experiment, i.e. the temperature control does not rely on injected pulses, and thus allows for an independent, stand-alone continuous data acquisition. One cryogenic detector was successfully operated, providing a proof of principle, and the results are discussed together with further possible improvements.

5.1 New Electronic Configuration for TES Readout

In the CRESST set-up, all bias currents delivered to the cryogenic detectors are supplied as DC currents. The simplicity of the DC bias electronics is the main reason behind such a choice, but a number of arguments favour the use of AC bias.

The possibility to inductively couple AC lines, for example, would prevent having a direct wired link which runs from room temperature all the way down to mK stage inside the cryostat, reducing the heat-load in the experimental set-up.

Another advantage comes from noise considerations and the use of a Phase Sensitive Device (PSD), such as a Lock-in amplifier, to read-out the signal from an AC-biased detector. PSDs can single out signal components at a specific frequency. In the case of AC bias, all signal components are centred around the bias frequency while the electronic noise remains distributed all over the frequency spectrum and can be filtered out.

The main intent of this new read-out is to measure the resistance value of a TES during

detector operation without the injection of control pulses (as they are described in Section 3.3.4). This is achieved by means of *Amplitude Modulation* (AM) and a modified bias scheme, which requires an AC bias current.

5.1.1 Basics of Amplitude Modulation

Let $s(t)$ denote the detector response to a particle interaction (*Information*) and $m(t)$ a periodic signal of angular frequency ω_m and amplitude M (*Carrier*). Their frequency representation reads as follows:

$$\begin{aligned} s(t) &= \frac{1}{\sqrt{2\pi}} \int d\omega \widehat{s}(\omega) e^{-i\omega t} \\ m(t) &= M \cos(\omega_m t) \end{aligned} \tag{5.1}$$

We call the quantity $y(t) = [s(t) + 1]\, m(t)$ the *modulated signal*. Making use of common properties of the Fourier transformation we can express $y(t)$:

$$\begin{aligned} y(t) = [s(t) + 1]\, m(t) &= M \left[\cos(\omega_m t) + \frac{1}{\sqrt{2\pi}} \int d\omega \widehat{s}(\omega) e^{-i\omega t} \cdot \cos(\omega_m t) \right] \\ &= M \cos(\omega_m t) + \frac{M}{\sqrt{2\pi}} \int d\omega \frac{\widehat{s}(\omega + \omega_m) + \widehat{s}(\omega - \omega_m)}{2} e^{-i\omega t} \end{aligned} \tag{5.2}$$

From equation 5.2 we observe that the modulated signal appears as the superposition of two distinct components, namely the carrier and a second term containing the information on the signal, which can then be fully reconstructed (see Figure 5.1). The main advantage of amplitude modulation, for the scope of this chapter, is the possibility to fully reconstruct both the carrier and the signal at the same time. This will allow us to apply thermal stabilisation to the carrier amplitude without injection of heater pulses, thus no online trigger and pulse amplitude reconstruction is required.

5.1.2 AC BIAS current

In order to use the modulation technique, an AC bias current is needed. A naive approach would be to use the standard circuit described in section 3.3.3 and simply replace the DC current source with an AC one. The detector's output can be reconstructed by means of a phase-sensitive device, such as a lock-in amplifier.

Recalling equation 3.16, we set:

$$I_b = I_0 \cos(\omega_m t) \tag{5.3}$$

With R_{T0} as the resistance value of the TES in the operating point, we can write the current flowing through the SQUID input coil in the presence of a small variation δR_T:

$$I_s = R_s \frac{I_0 \cos(\omega_m t)}{R_s + R_{T0}} \left(\frac{R_{T0}}{R_s} + \frac{1}{R_s + R_{T0}} \delta R_T \right) \tag{5.4}$$

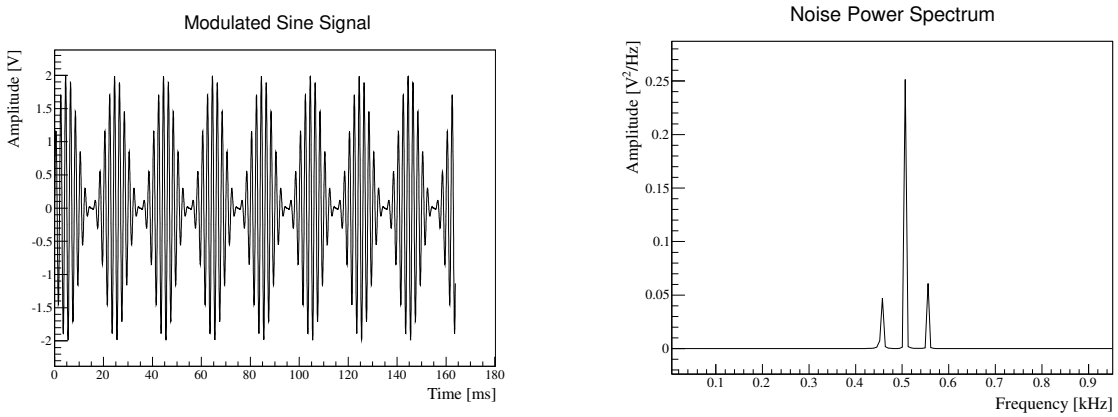

(a) (b)

Figure 5.1: The two pictures show the effect of amplitude modulation on a 50Hz sine wave (signal) modulated at 0.5kHz (carrier). (a) Time domain representation of a 50Hz sine wave modulated at 0.5kHz. (b) Signal Power Spectrum of waveform. The actual signal appears shifted in frequency and mirrored around the carrier frequency. The two side lobes are the terms $\widehat{s}(\omega + \omega_m)$ and $\widehat{s}(\omega - \omega_m)$ in equation 5.2 containing the information signal.

Defining $s(t) = \frac{1}{R_s + R_{T0}} \delta R_T$ and knowing that in the operating point $R_{T0} \simeq R_s$, we get:

$$I_s \propto \cos(\omega_m t)\,[1 + s(t)] \tag{5.5}$$

Equation 5.5 has the same form as the definition of the modulated signal in equation 5.2. In Figure 5.2a, a standard pulse from an X-ray of ^{55}Fe is shown and its power spectrum is shown in Figure 5.2b. The signal was acquired while biasing the TES with a DC current. The effect of amplitude modulation on the detector output is shown in Figure 5.3 for both the signal and its power spectrum. A modulating frequency of 6kHz had been chosen for visualisation. The reconstruction of the original signal is performed exploiting orthogonality of the cosine functions. Taking V_{out} as the SQUID output from the signal I_s in equation 5.5 and U_{out} as the reconstructed signal:

$$\begin{aligned} U_{out}(t) &= \int d\omega V_{out} \cos(\omega_m t) e^{-i\omega t} \propto \int d\omega I_s \cos(\omega_m t) e^{-i\omega t} \\ &\propto \overline{M} \int d\omega\,[1 + s(t)] \cos(\omega_m t) e^{-i\omega t} \\ &\propto \overline{M} + \overline{M} \cdot s(t) \end{aligned} \tag{5.6}$$

Equation 5.6 shows that the reconstruction of a modulated signal from a detector comes with DC component proportional to the amplitude of the AC TES excitation response $\overline{M}$. A Lock-in amplifier was used for these measurements, whose output provides the decorrelated signal as in equation 5.6. The decorrelation in equation 5.6 is handled by the Lock-in amplifier in time domain and the actual computation of U_{out} is given in

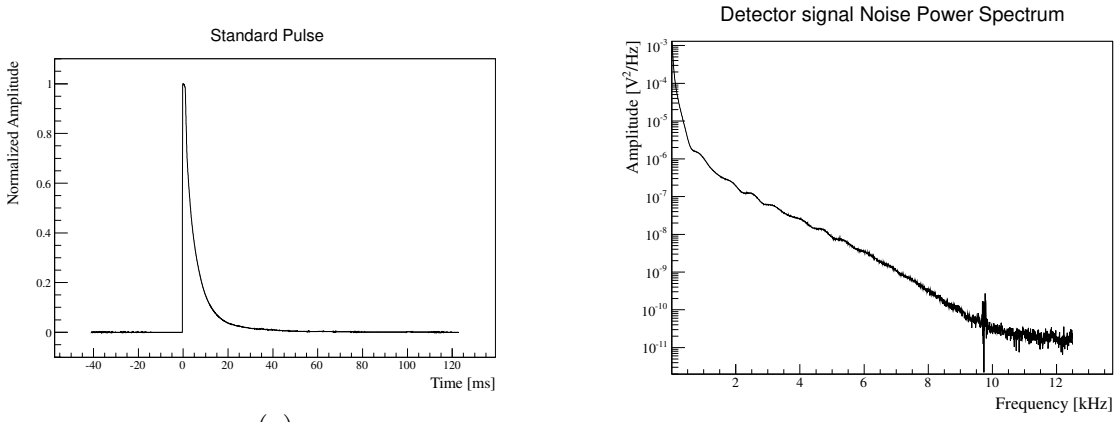

(a) (b)

Figure 5.2: (a) Standard pulse of a ^{55}Fe X-ray hit in time domain and (b) corresponding Signal Power Spectrum. The pulses were acquired while using a standard DC bias current.

Equation 5.7:

$$U_{out}(T) = \frac{1}{T}\int_0^T V_{out}(t)\cos(\omega_m t)dt \tag{5.7}$$

The reconstructed signal is obtained averaging the product of the SQUID output V_{out} and the reference signal $\cos(\omega_m t)$ over a time T larger than the period of the reference signal. The operation of averaging over T is a low-pass filter and it results in $U_{out}(T)$ being much slower than the reference. The crucial parameters in this process are the modulating frequency ω_m and the averaging time T. From Figure 5.3b we can observe that the modulated signal bandwidth is double the original signal bandwidth. Furthermore the left-side lobe is contained in the range [0-ω_m], so signal components above ω_m cannot be fully reconstructed. In addition, the averaging over the time T is a low-pass filter which limits the bandwidth of U_{out}. Therefore, it is better to have the highest possible ω_m (wherefore the shortest T). For the work presented in this chapter, the choice of the modulating frequency has been driven by experimental constraints, mainly the presence of a low-pass filter in the BIAS line, which limited the frequency delivered to 1kHz and to an averaging time of 1.25ms.

5.1.3 The proposed bias circuit

The use of AC BIAS current as presented in the previous section has the advantage of encoding the working point of the detector and the detector's response in the same signal, making the baseline value of the signal the result of an AC excitation of the thermometer, in a similar way to an excitation induced by a control pulse. Control pulses have the power to drive the TES out of the transition, offering the maximum sensitivity since they exploit the full dynamic range of the detector. This cannot be achieved with the AC BIAS current, as it implies detector's saturation during operation and thus no sensitivity

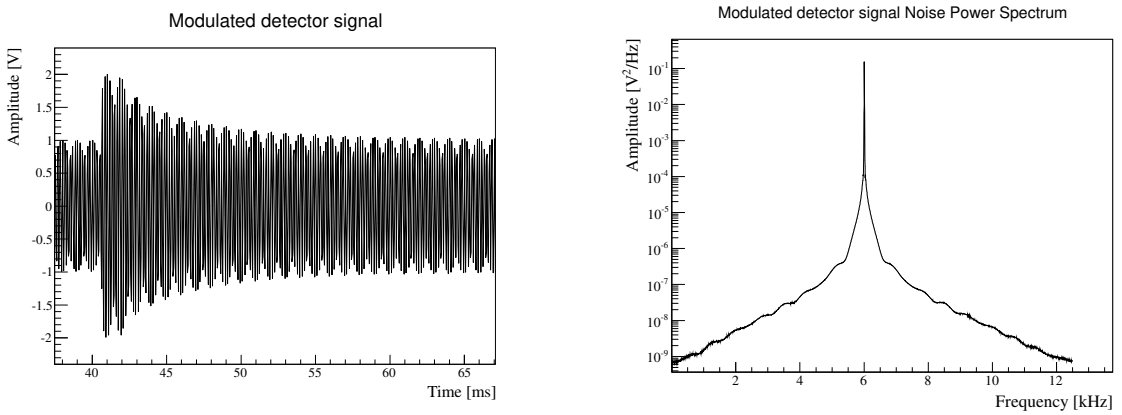

(a) (b)

Figure 5.3: The two pictures show the effect of amplitude modulation on the standard event in Figure 5.2. (a) Time domain representation of a detector pulse modulated at 6kHz and (b) its Power Spectrum. The waveform is sampled at 25kHz, which implies a frequency representation in the range 0-12.5kHz. The modulating frequency of 6kHz had been chosen is order to fit the power spectrum of the signal in the middle of (b). The frequency representation of the modulated signal clearly shows the spectral shape in Figure 5.2b, shifted by the 6kHz of modulation and mirrored around this value.

to particle interaction. Additionally, a non-zero baseline value restricts the dynamic range of the acquisition. In order to overcome these inconveniences, a new biasing scheme is proposed.

The circuit in Figure 5.4 closely resembles a Wheatstone bridge. Two branches are independently biased with the two currents i_1 and i_2. To these two branches belong the shunt resistor R_S and the TES R_T. The SQUID input coil bridges the branches and the signal input i_3 reads:

$$i_3 = i_1 - \frac{R_T(i_1 + i_2)}{R_T + R_S} \tag{5.8}$$

The sensitivity of i_3 to a small variation δR_T can be computed as:

$$\delta i_3 = -\frac{(i_1 + i_2)R_S}{(R_T + R_S)^2}\delta R_T \tag{5.9}$$

Except from the sign, sensitivity in Equation 5.9 is the same as the one of the standard circuit in equation 3.17, letting $i_1 + i_2 = I_T$.

For the experimental measurement a standard CRESST-III light detector was employed. Injecting equal currents in the circuit ($i_1 = i_2$) simplifies equation 5.8 making i_3 dependent only on $\frac{R_T}{R_S}$. While the reference resistor R_S is constant, the TES resistance value R_T can be controlled with the heater on the detector. The output of the SQUID is a function of R_T.

We can study three special cases, namely:

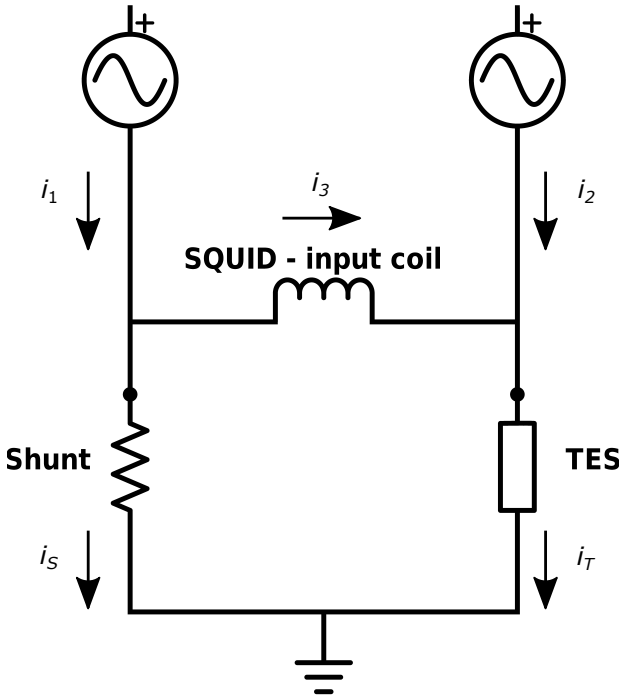

Figure 5.4: The proposed read-out scheme. The TES and the shunt resistor belong to two different branches which are independently biased with two AC current sources. The two branches are bridged by the SQUID input coil. The current flowing through the latter depends on the ratio between the two injected currents and the ratio between the TES and the shunt.

- Normal conducting TES $R_T \cong 2R_S$
- Superconducting TES $R_T = 0$
- Balanced bridge (as common configuration in a Wheatstone bridge) $R_T = R_S$

The first case is shown in Figure 5.5. Being $R_T \simeq 2R_S$, 2/3 of $i_1 + i_2$ have to flow through R_S, which means $i_3 = 1/3i_1$. In the second case, $R_T = 0$ means that all $i_1 + i_2$ goes to the TES, thus $i_3 = i_1$ (Figure 5.6). The most interesting case is when the circuit is balanced. Being $R_T = R_S$ there is no current through the SQUID input coil $i_3 = 0$ (Figure 5.7). In this case the current in the TES is simply i_2. The last case is the most interesting because having a zero-output as baseline allows for maximal amplification without saturation of the pre-amplifier, offering more sensitivity (on the contrary, a non-zero output cannot be amplified beyond the maximum input accepted by the data acquisition). As in the case of a Wheatstone bridge the measurement becomes free of any DC component, establishing a bare comparison of the R_T with the reference resistor R_S based upon the balancing of the circuit. The individual tuning of i_1 and i_2 offers the possibility to define the working point at any desired output value. In the example above, the zero-output is achieved with $R_T = R_S$ but, in real applications, the optimal operating point of the detector does not

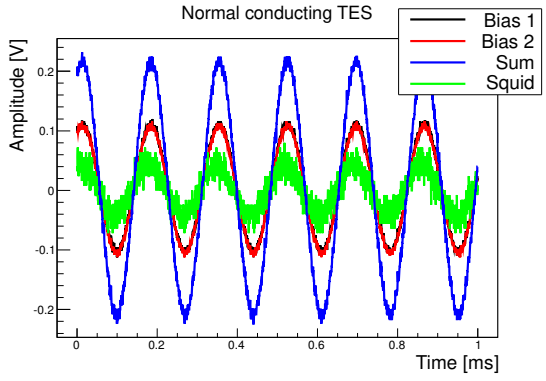

(a)

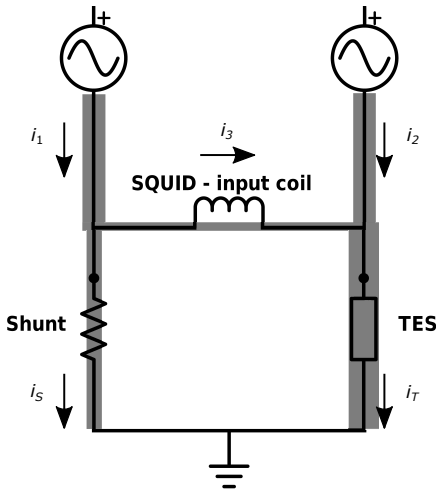

(b)

Figure 5.5: (a) AC BIAS signals and SQUID output. In black is the signal driving i_1, in red i_2, and in blue the sum of the two. The SQUID output is shown in green. (b) In the case of $R_T \simeq 2R_S$, 2/3 of the total injected current are drawn by the reference resistor. The SQUID input is $i_3 = -1/3 i_1$.

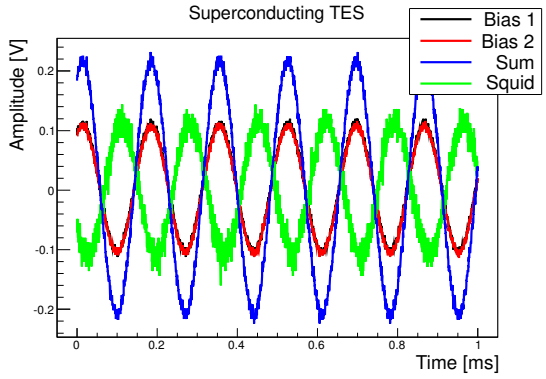

(a)

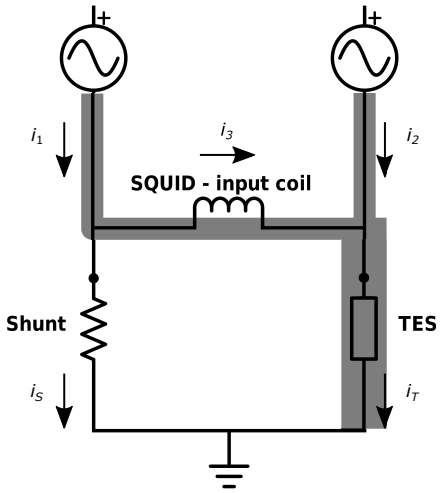

(b)

Figure 5.6: (a) AC BIAS signals and SQUID output. In black is the signal driving i_1, in red i_2, and in blue the sum of the two. The SQUID output is shown in green. (b) The condition $R_T = 0$ implies that $i_1 + i_2$ is entirily drawn by R_T and $i_3 = i_1$.

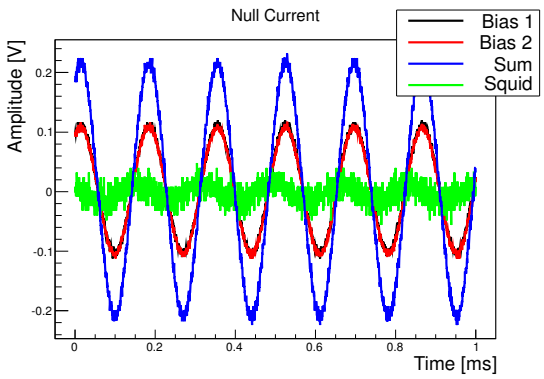

(a)

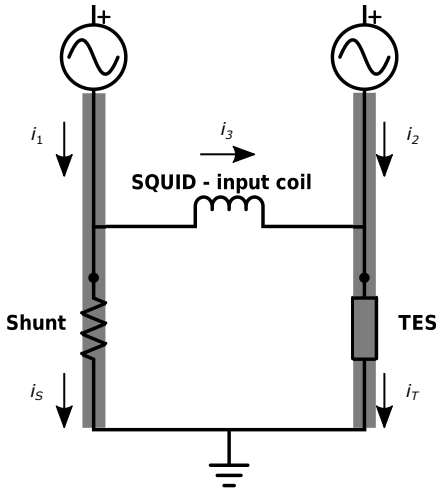

(b)

Figure 5.7: (a) AC BIAS signals and SQUID output in case of $R_T = R_S$. In black is the signal driving i_1, in red i_2 and in blue the sum of the two. In green the SQUID output is shown. In real operation the optimised working point may not correspond to such a condition. Varying the ratio i_1/i_2 keeping $i_1 + i_2$ constant allows us to balance the circuit at any desired value of R_T. A small signal at the SQUID output is still visible. This is most likely due to a small phase misalignment of the two input currents. Such a signal does not pose any issue, since the Lock-in amplifier output averages it out (it is in opposite phase with respect to the reference signal). (b) Depiction of the balance condition $i_3 = 0$.

necessarily match this condition. The total current $i_1 + i_2$ injected into the circuit splits between the two branches in accordance with R_T/R_S. The detected signal current i_3 is then the direct measurement of how much current is splitting, different from the standard scheme in Section 3.3.3 where the signal is the current flowing in one branch only. Once the operating point had been established, it is possible to balance the circuit to have $i_3 = 0$ tuning the ratio i_1/i_2 while keeping the total current $i_1 + i_2$ constant[1].

[1]This guarantees that the current through the TES i_T is kept constant, note that $i_1 + i_2 = i_T + i_S$, where i_S is the current flowing through the shunt resistor.

Figure 5.5, 5.6 and 5.7 have been obtained setting the heater output to three fixed values and acquiring the SQUID output. The full transition can be probed with a slow sweep of the heater power and by reading the demodulated SQUID output. For comparison the same transition had been measured with a DC bias of 500nA and direct acquisition of the SQUID output, with the results shown in Figure 5.9. The modulating frequency had been set to 1kHz because of a low pass filter present in the (inaccessible) cryogenic set-up. An unfortunate consequence of this is that it is not possible to quantify the actual amount of AC current delivered to the BIAS circuit, as the low-pass filter lies somewhere before in the electronics chain.

5.1.4 Operation and Performance

The detector was operated in the setup shown in Figure 5.8 for a total of $\sim$ 9 hours of data taking. During one half of the measurement, the detector was operated using the new read-out scheme and the temperature control applied to the baseline. The second half of the measurement was carried out using the standard DC bias scheme and the temperature control was performed using heater pulses. Results from the two measurements allow for a direct comparison of the two methods. Pulse amplitudes had been computed using standard event fit as described in Section 3.4.1 for both cases.

Detector operation with DC bias

For the standard DC bias current application, large heater pulses, as the one in Figure 5.10, were used to control the temperature of the TES. The stability over time and the resolution at the peak of the control pulses height are shown in Figure 5.11. The width of the peak of control pulse height distribution is an indicator of the quality of the temperature control.

Detector operation with AC bias

When applying the AC bias both the detector output and the Lock-in amplifier output were recorded. It was possible to introduce an amplification of up to a factor 10 to increase the sensitivity, without exceeding the maximum 10V input of the DAQ.

In Figure 5.12 the modulated signal corresponding to a ^{55}Fe X-ray hit is shown, together with the Lock-in Amplifier output.

The demodulated pulse shows a rise-time of $\sim$20ms, much slower than the rise-time of the pulse in Figure 5.2a. This is due to the modulating frequency being limited to 1kHz which acts as a low pass filter, reducing the bandwidth of the signal.

In contrast to the DC current bias case, with this method the temperature control and, consequently the determination of the stable detector's operation time periods, is based on the baseline output. Baseline values for the events recorded are shown in Figure 5.13a, while Figure 5.13b shows their distribution.

From Figure 5.13 we see that the mean value of the baseline is not exactly 0V, but rather -85mV. This is a consequence of having pulses randomly distributed over the baseline.

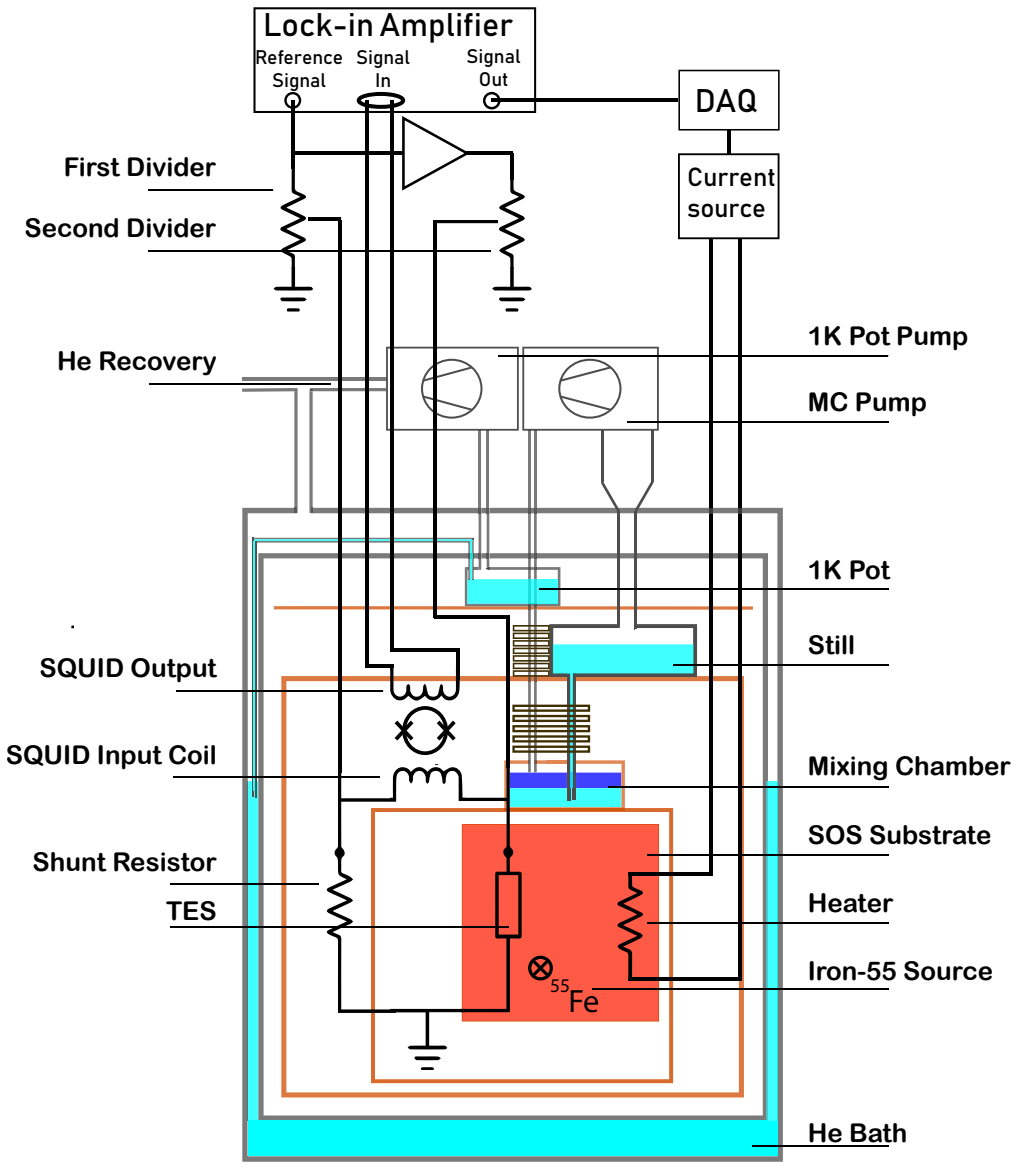

Figure 5.8: Schematics of the experimental set-up. A 2x2cm Silicon-on-Sapphire substrate equipped with a TES is operated at mK as cryogenic detector. The BIAS circuit is the one described in Figure 5.4. The Lock-in Amplifier generates a 1kHz reference signal which is split into the two branches of the circuit, each of which is fed to a voltage divider, allowing for individual tuning of the two bias currents. The SQUID output is returned to the Lock-in Amplifier which outputs the demodulated signal according to equation 5.6. The baseline is used for temperature control and deviations from the working point are corrected with a feedback delivered via the heater. In order to compare the new read-out with the standard one, one of the two bias lines can be left open and the other one used to supply a DC current, recovering the configuration in Figure 3.14.

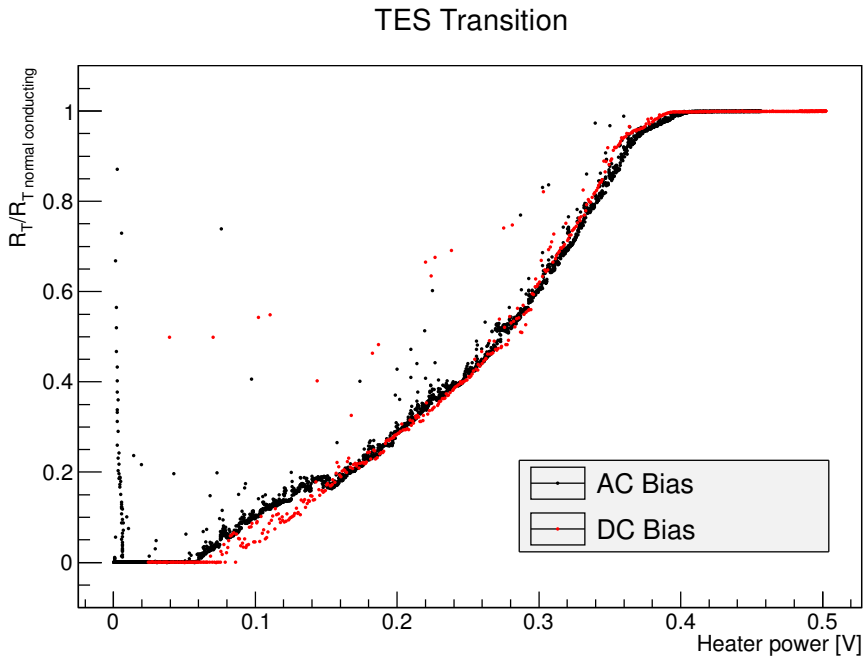

Figure 5.9: Two measurements of the TES transition. In red are the points sampled using 500nA DC Bias in configuration as in Figure 3.14, in black the points acquired with the AC Bias and the circuit in Figure 5.4. The two reproduce the same transition shape (notice the kink close to the normal conducting state) which suggests that the actual amount of effective AC current is somewhere close to 500nA. The data has been normalised to the normal conducting value and shifted to have the superconducting state at 0 output for visualisation purpose. In the case of the circuit in Figure 5.4 the zero-output corresponds to $R_T = R_S$ as discussed in this section.

Pulses, which are always positive excursions of the baseline, are compensated by the temperature control, resulting in a negative average value of the baseline, as the latter is dependent on the event rate. As a direct consequence of this, the operating point of the detector is shifted and is not the desired one. Operation in a low background environment (such as the CRESST installation) would not be affected by such an issue. Still, a possible solution is outlined at the end of this chapter.

Comparison of the two operation methods

A first indicator for the correct operation of a TES is the quality of the temperature control. In Table 5.1 the relevant quantities related to the temperature stabilisation are reported.

The resolution of the control value, accounting for the 10 times amplification, appears to be approximately 10 times worse than the one obtained using control pulses. The control value itself is different to the desired 0V output. As mentioned, the presence of particle pulses induces a compensation from the control system resulting in an effective controlled

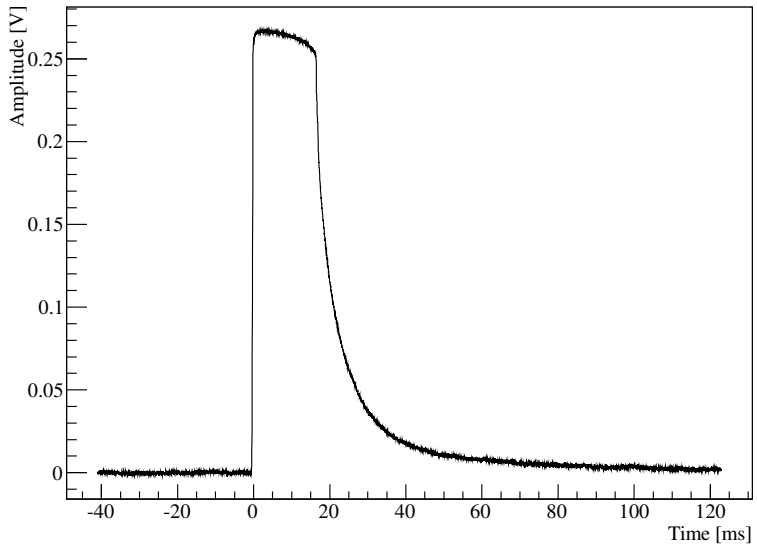

Figure 5.10: Control pulse used to control the operating point of the detector, operated with the DC bias current. The pulse saturates the TES completely and the excursion from the baseline to the plateau spans all over the sensor's dynamic range.

Bias	Resolution[V]
DC	0.0012
AC	0.112

Table 5.1: Controlled values and resolutions. The AC bias values are amplified by a factor of 10 w.r.t. the DC case.

value different from 0V.

The detector was illuminated with an ^{55}Fe source, which emits X-rays of 5.9keV and 6.5keV energy. The resolution to the ^{55}Fe X-ray interactions is assumed to be the ultimate quality parameters for this comparison. In Figure 5.14 the energy peaks of the ^{55}Fe source are shown for the two cases.

The energy spectra had been fitted using the following fit function:

$$C(E|\sigma, E1, Cnt) = \frac{1}{\sqrt{2\pi\sigma^2}} Cnt(e^{\frac{(E-E_1)^2}{2\sigma^2}} + ce^{\frac{(E-E_2)^2}{2\sigma^2}}) \tag{5.10}$$

The parameters representing the resolution (σ), the normalisation (Cnt), and the energy of the most prominent peak (E_1) had been left as fit parameters, while E_2 was defined as $E_1 + 0.6$keV and c hardcoded as the relative branching ratio of the two emissions. As a result from the fit, the resolution σ at the two ^{55}Fe peaks obtained with the new method is around 38% worse, when compared with the one from the standard measurement.

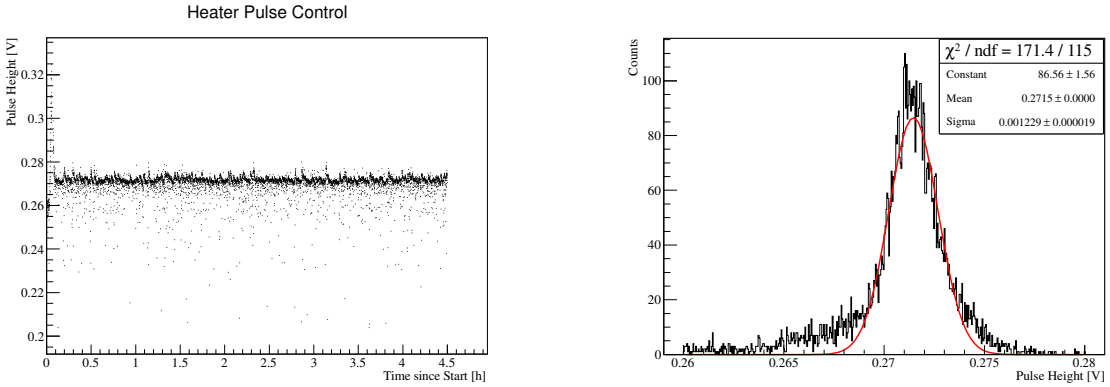

(a) (b)

Figure 5.11: (a) Control pulses height vs. time and (b) corresponding resolution. The peak resolution is evaluated with a gaussian fit. For this measurement control pulses in the interval [0.270V - 0.275V] had been considered stable.

5.2 Results and discussion

The comparison of the resolutions of the detector operated with the new read-out and the standard one shows a clear degradation in performance. As the detector's physics is exactly the same, as are the environment and corresponding systematics, this degradation has to therefore be ascribed to the new operation. Two main issues arose from the previous sections, namely the different pulse shape and the temperature control. The first affects the quality of the template fit, since signal components above the modulation are lost. To see this effect we can compare Figure 5.15 and Figure 5.16. The determination of the minimum is more accurate in the DC mode (Figure 5.16a) than in the AC one (Figure 5.15a). Looking directly at the waveforms (Figure 5.15b and 5.16b), we can observe how the loss of signal components due to the modulation degrades the pulse reconstruction, while having all the signal features available increases the quality of the fit.

Because of non-linearities in the transition, it is hard to evaluate the effect of the shift in the working point while AC bias detector operation.

In order to improve the quality of the detector operation using the modulated bias, the (as of yet) limiting aspects will be further tested. It is necessary to adapt the wiring of the cryostat so that a larger modulating frequency can be used. The temperature control can be made less sensitive to particle interaction introducing a hardware low pass filter which filters out pulses from the baseline. The cost of such modification would be to split the Lock-in amplifier output into two lines: one to acquire the detector's output (preserving the pulses to be recorded) and a second, filtered one, dedicated only to temperature control.

Despite the worse performance obtained in the measurement presented in this chapter, the use of an AC bias current is appealing for two reasons. Firstly, it allows for temperature control without the need of control pulses. In addition to the possibility of only relying on the continuous DAQ, getting rid of control pulses could allow stable operation even in

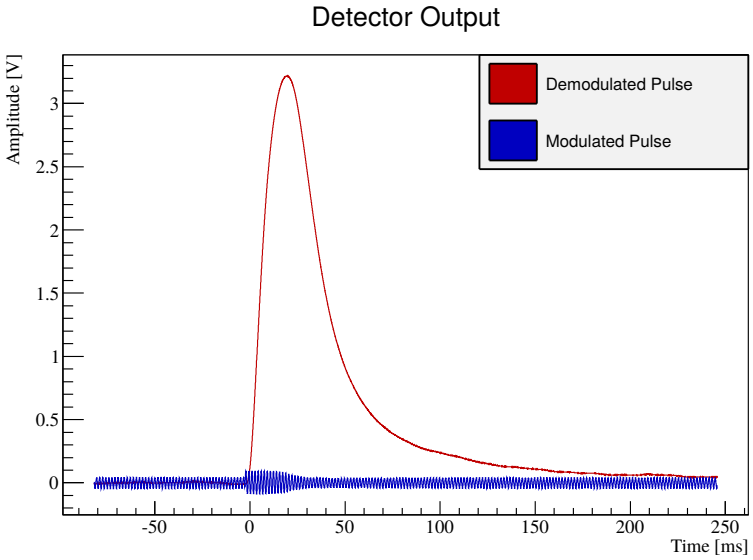

Figure 5.12: Detector's output (blue) and pulse reconstructed by the Lock-in amplifier (red). The demodulated signal was amplified by a factor of 10 compared to the bare output. The pulse in the picture is induced by an X-ray from the ^{55}Fe source and its height is roughly 3V at the output of the electronics chain, making the x10 amplification the maximum allowed to match source-induced events to the DAQ input range. The rise-time of the pulse is around a factor of 10 slower that the one acquired with the conventional DC biasing (see Figure 5.2a). The onset of the pulse results deformed as well (the rise at the onset is not sharp). The cause is the averaging time of 1.25ms that acts as a low-pass filter, distorting the signal.

presence of a significant count rate[2]. Secondly, the effect of the modulation on the spectral features of the signals is an upward shift in frequency. Higher frequencies have in general a reduced noise contribution compared to lower ones (mainly 1/f noise, see Figure 4.15a in Chapter 4).

[2]In the CRESST experiment, control pulses largely outnumber particle interaction induced pulses and this guarantees the stability of the operation. Temperature control in presence of a high count-rate is less effective because of the necessarily reduced number of delivered control pulses.

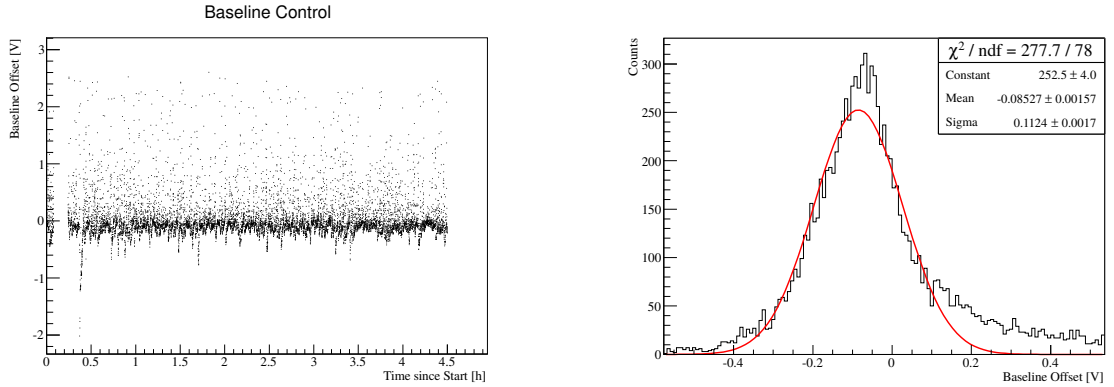

(a) (b)

Figure 5.13: (a) Particle Event Baselines vs. Time and (b) corresponding Baseline distribution. The peak resolution is evaluated with a gaussian fit. For this measurement control pulses in the interval [-0.2V - 0.1V] had been considered stable.

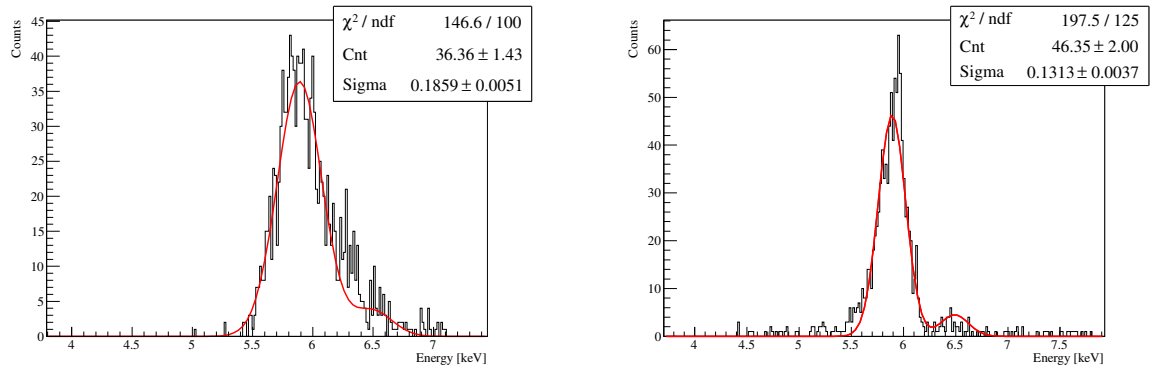

(a) (b)

Figure 5.14: Comparison of the energy spectra acquired with the two different operation modes. The peaks had been fitted with two gaussians having the same resolutions and the relative amplitude fixed to the one expected from the K_α and K_β decay rates of the ^{55}Fe source. (a) ^{55}Fe energy spectrum, acquired while the detector was operated with the new modulated read-out. (b) ^{55}Fe energy spectrum, while the detector was operated with the normal DC bias.

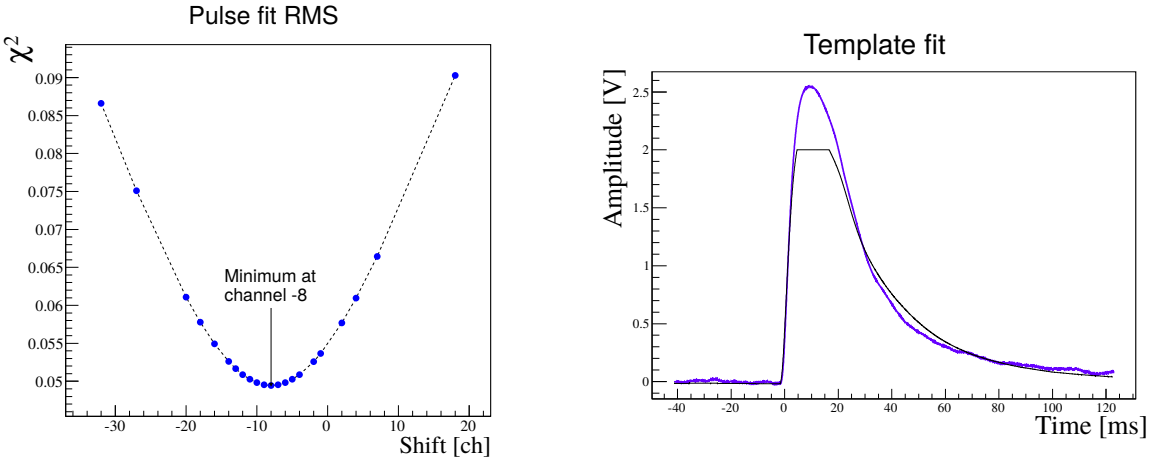

(a) (b)

Figure 5.15: Fit of an X-ray from ^{55}Fe source, detector operated with the new read-out. (a) χ^2 minimum determination in fitting one particle event. Despite the saturation region of the pulse height, the χ^2 around its minimum shift is very regular and smooth. (b) Template pulse fitting particle event. Template pulse in black, real pulse in blue. Notice how the top part of the pulse, in saturated region, appears smeared. Fast signal components are smoothened away because of limited modulating frequency. In both pictures there is no clear sign of the saturation, as a consequence of the low modulating frequency.

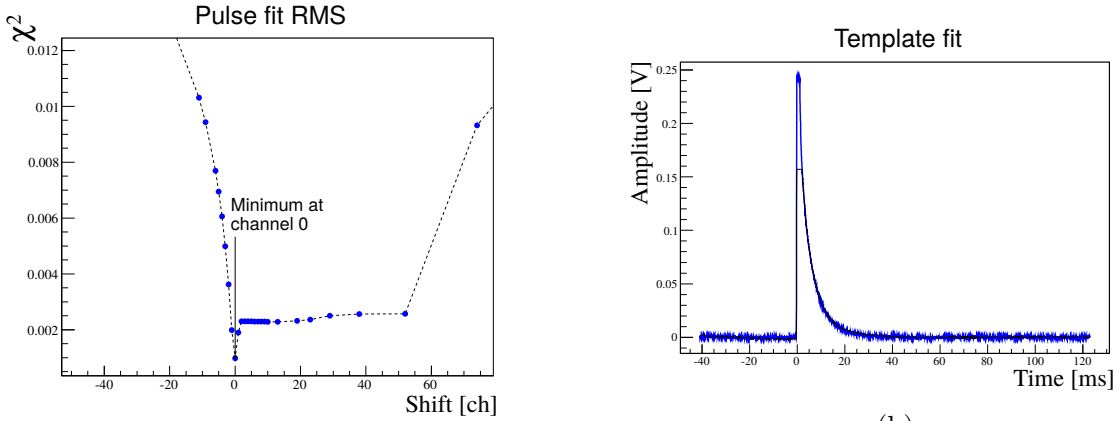

(a) (b)

Figure 5.16: Fit of an X-ray pulse from ^{55}Fe source, detector operated using DC bias. (a) χ^2 minimum determination in fitting one particle event. The peculiar shape of the minimum is due to the saturation of the pulse. (b) Template pulse fitting particle event. Colorcoded in black is the template pulse, in blue the real pulse. Compared to Figure 5.15b the saturation is apparent. In addition, the width of the χ^2 minimum is more accurate and more sensitive to the saturation (notice the asymmetry of the χ^2 around the minimum).

Appendix A

Data representation

Data processing is one of the most important aspects at the base of this thesis work. In this appendix an overview of the actual storage and CRESST data representation is given.

Notes and glossary

A short glossary for the most used technical terms is reported hereunder.

Sample

Single data recorded from one channel. The sampling rate in CRESST-III is 25kHz so that each sample represents the sensor's output averaged over 40μs, with a dynamic range of [-10,+10]V and 16-bit resolution.

Datastream

Sequence of all recorded samples from one channel. The recorded samples usually represents the sensor's output of a couple of days.

Data window

Contiguous, time-ordered subset of the datastream. Being the full datastream extremely large, a data window is used to investigate the sensor's response at a specific time. In CRESST-III a data window is chosen to contain 16384 samples or, equivalently, it represents 655.36ms.

Pulse

Transient sensor's response to a discrete energy deposition in the active volume of the detector. The pulse duration is what rules the size of a data window, chosen such that it can fully contain pulses of interest.

Heater pulse

Artificially induced pulse, by means of joule heating of a resistor directly deposited on the detector.

Template pulse/Standard pulse

Ideal sensor's response. It is the sensor's output to an energy deposition subtracted the noise. Since any recorded data from the sensor is affected by random noise fluctuation, a

template pulse is obtained by averaging a large set of data windows containing time-aligned pulses of the same type.

Baseline

Sensor's output during detector's operation, in absence of any pulse. When attributed to an event, it refers to the region in the data window before the pulse's onset (pretrigger region).

Empty baseline/empty trace

Data window randomly taken from the datastream. Because of the low background environment, an empty baseline is most likely not to contain any pulse, this is not guaranteed though.

Event

It is the full detector module's output to a discrete energy deposition. Given the CRESST-III detector module description in section 3.3 an event consists of three simultaneous data windows for the three active channels of each module: phonon channel, light channel, holding sticks.

Standard Acquisition

It is the hardware trigger-based acquisition described described in Chapter 3. The CRESST experiment relied on the Standard Acquisition only until the CRESST-III stage, when the continuous acquisition flanked the standard one in order to allow for the data processing described in Chapter 4.

Record structure

The basic object for the data analysis is an event. Events are a collection of pulses recorded from the three channels of each detector. Event tagging is carried out by the trigger scanning the phonon channel data for pulses above threshold. In the case of the Optimum Filter-based trigger the offline procedure is described in Chapter 4. The standard acquisition outputs events during detectors operation whenever the hardware trigger fires a signal.

Pulses are organised in records. Each record has an header followed by the vector representing the individual pulse. The structure of one record is reported below.

Integers:
- Channel number
- Number of coincident pulses
- Trigger counts
- Trigger delay
- Computer time [s]
- Computer time [μs]
- Channel delay to test pulses

Unsigned integers:
- 10MHz timestamp high word
- 10MHz timestamp low word

```
        - Number of muon veto events until this event
Single precision (float) numbers:
        - Measuring time [h]
        - Accumulated dead time [h]
        - Test pulse amplitude
        - DC heater output
Unsigned 16-bit integer:
        -digitised pulse
```

The records are written in a time-ordered sequence, so that events are built grouping together a number of subsequent records equal to the *number of coincident pulses* of the first pulse of each group. The test pulse amplitude is used to tag the type of the pulse. A negative value means that the recorded data is an empty baseline, 0 means that the data is a particle-induced pulse, a positive value means that the pulse was artificially generated using the heater. In this last case the value of the entry is the amplitude of the injected pulse.

The online temperature control writes a separated record for each control pulse delivered. Since control pulses are used for stability purpose only, their vectors are not stored. Instead their on-line reconstructed amplitudes is saved. The records for this pulses follow the more compact structure:

```
Integers:
        - Channel number
        - Time between the firing and the triggering of the pulse
Unsigned integers:
        - 10MHz timestamp high word
        - 10MHz timestamp low word
Single precision (float) numbers:
        - Reconstructed pulse height
        - Accumulated deadtime [s]
```

The data provided by the muon veto is the signal amplitude of all scintillating panels which fired a trigger. Each record has the following structure:

```
Unsigned integers:
        - 10MHz timestamp high word
        - 10MHz timestamp low word
Unsigned short
        - Number of stored values
        - Value 1
        - ...
        - Value N
        - Channel number of Value 1
        - ...
        - Channel number of Value N
```

All recorded data are stamped with the same 10MHz clock in order to allow for the tagging of coincident events.

Appendix B

Band fit parametrisation

The Light Yield vs Energy plot is the common way to display CRESST-data and it is the input for the calculation of the dark matter sensitivity as described in Chapter 3 and 4.

The event-by-event background rejection is possible due to the band structure in which the recorded events cluster depending on their recoil type. Dark matter interaction candidate events are those whose Light Yield is contained below the average Light Yield of the oxygen recoil band and above the 99.5% of the tungsten recoil band. Such definition of the acceptance region requires a description of the recoil bands. In particular, the mean value and the width of each band are the quantities of interest.

Mean of the band

The mean of the light output of e/γ events has the following empirical parametrisation:

$$L^{e/\gamma}(E_R) = (L_0 E_R + L_1 E_R^2)\left[1 - L_2 \exp\left(-\frac{E_R}{L_3}\right)\right] \tag{B.1}$$

Where E_R is the total deposited energy. We consider the scintillation as linear at first approximation, encoding this assumption in the leading term $L_0 E_R$. Non-linearities are described by the $L_1 E_R$ term and are usually small in the [0,40]keV energy region. At very low energy the light-output drops with a highly non-linear behaviour. This effect, rather common among inorganic scintillators, is known as the non-proportionality effect[94] and it is accounted for by the second factor in Equation B.1.

The Light Yield of the e/γ band is $L^{e/\gamma}(E_R)/E_R$. Since the calibration is based on γ-lines the linear term is usually $L_0 \approx 1$. In the region of interest, the low energies, the term L_1 can be neglected.

Width of the band

The distribution of e/γ events around their expectation value $L^{e/\gamma}(E_R)$ for the given energy deposition E_R is gaussian and its width is determined by the finite energy resolution of the

detector. Both the light detector and the phonon detector resolutions play a role in the width

We write the resolution of the band, at the detected energy in the light channel $L^{e/\gamma}$, as:

$$\sigma(L^{e/\gamma}) = \sqrt{S_0 + S_1 L^{e/\gamma} + S_2 (L^{e/\gamma})^2} \tag{B.2}$$

The S_0 term is the width at 0 energy deposition. The main contribution is due to the baseline noise of the light detector $\sigma_{l,0}$. Because of the finite resolution of the phonon channel $\sigma_{p,0}$, even the E_R energy suffers from an uncertainty due to the mismatch between the true deposited energy and the reconstructed energy. Accounting for both aspects we write:

$$S_0 = \sigma_{l,0}^2 + \left(\frac{dL^{e/\gamma}}{dE_R} \sigma_{p,0} \right)^2 \approx \sigma_{l,0}^2 + \sigma_{p,0}^2 \tag{B.3}$$

where the last equivalence is due to the dominating L_0 term in Equation B.1. The energy-scaling term $S_1 L^{e/\gamma}$ accounts for the poissonian nature of the scintillation. The number of created photons fluctuates proportionally to the total emitted energy. At last a term for considering additional, energy-depended contributions to the resolution S_2 is introduced.

Nuclear recoil bands

The parametrisation of the nuclear recoil bands naturally follows the one of the e/γ band. The non-proportionality effect is by experimental observation non-visible for these bands, so that the mean of the band, accounting for the specific quenching factor $QF_x(E_R)$ of the nuclear species x, takes the easier form:

$$L^x(E_R) = QF_x(E_R)(L_0 E_R + L_1 E_R^2) \tag{B.4}$$

The width of the quenched bands is determined using the S_0, S_1 and S_2 parameters describing the e/γ band. Only S_0, being explicitly dependent on dL^x/dE_R needs caution. Making the assumption $dL^x/dE_R \approx QF_x$, S_0 reads:

$$S_0 = \sigma_{l,0}^2 + [QF_x(0)\sigma_{p,0}] \tag{B.5}$$

In Equation B.5 we assume the constant values at zero energy for the phonon energy resolution and the quenching factors. This approximation is justified because the low-energy region is the only relevant one for the dark matter analysis.

Having a parametrisation for mean values and the widths of four bands, we can finally determine the relevant parameters via likelihood fit. To do so we make use of data recorded during a neutron calibration, so that all the recoil bands are populated with events.

The fitted bands and the data used for Detector A are shown in Figure B.1. The fit parameters are reported in Table B.1.

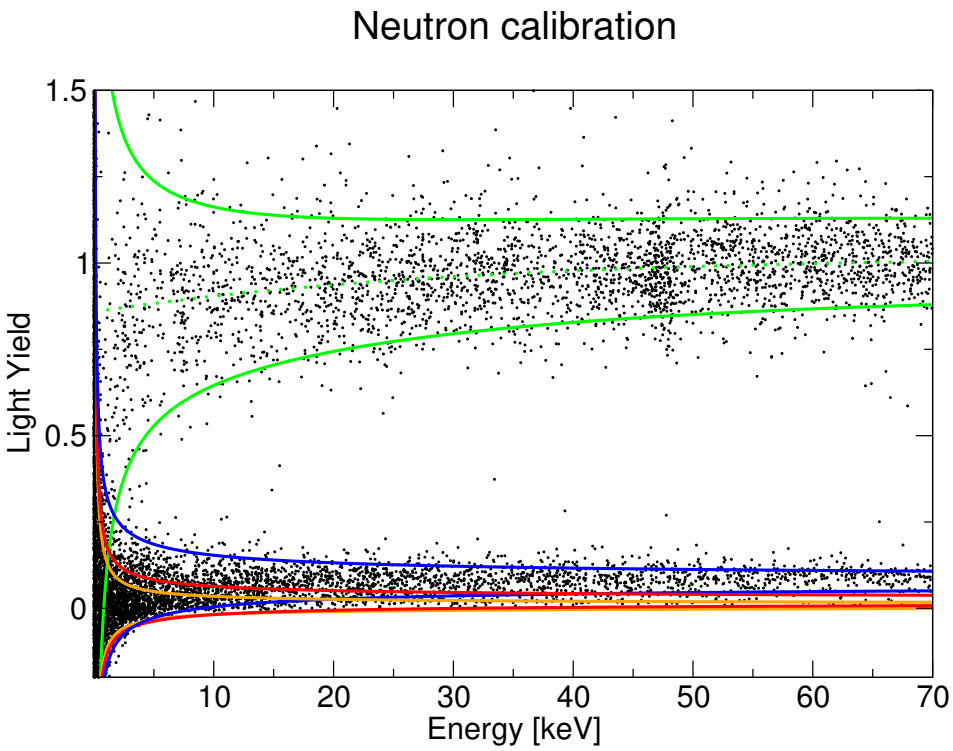

Figure B.1: Light Yield plot of detector A exposed to an AmBe neutron source. Both γs and neutrons are emitted, to that all bands result populated. The contours define the 90% upper and lower bounds of each recoil type. Green corresponds to electron recoils, blue to oxygen recoils, red to calcium recoils and orange to tungsten recoils. The parameters defining the bands are obtained fitting the parametrisation to the neutron calibration data and are listed in Table B.1.

Parameter	Best fit	Error
L_0	1.0132	0.01
L_1* [keV^{-1}]	0	0
L_2	0.147	1.510^{-3}
L_3 [keV]	25.8	0.2
S_0 [keV$^2_{ee}$]	$0.7{\cdot}10^{-2}$	$7{\cdot}10^{-5}$
S_1 [keV$_{ee}$]	0.25	$2.5{\cdot}10^{-3}$
S_2	$0.78{\cdot}10^{-2}$	$8{\cdot}10^{-5}$
QF_{Ca}	27.16	0.27
QF_O	10.76	0.1
QF_W	45	0.45

Table B.1: Parameters defining the bands in the Light Yield vs Energy plot of Detector A, determined by fitting the bands parametrisation to the neutron calibration data. The sign * marks the fixed parameters in the fit.

Bibliography

[1] F. Zwicky, "Die Rotverschiebung von extragalaktischen Nebeln," *Helvetica Physica Acta*, vol. 6, pp. 110–127, 1933.

[2] N. Aghanim *et al.*, "Planck 2018 results. VI. Cosmological parameters," 2018.

[3] E. Hubble, "A relation between distance and radial velocity among extra-galactic nebulae," *Proceedings of the National Academy of Sciences*, vol. 15, no. 3, pp. 168–173, 1929.

[4] G. Lemaître, "Republication of: A homogeneous universe of constant mass and increasing radius accounting for the radial velocity of extra-galactic nebulae," *General Relativity and Gravitation*, vol. 45, pp. 1635–1646, Aug 2013.

[5] E. Komatsu *et al.*, "Five-Year Wilkinson Microwave Anisotropy Probe (WMAP) Observations: Cosmological Interpretation," *Astrophys. J. Suppl.*, vol. 180, pp. 330–376, 2009.

[6] P. de Bernardis *et al.*, "A Flat universe from high resolution maps of the cosmic microwave background radiation," *Nature*, vol. 404, pp. 955–959, 2000.

[7] A. A. Penzias and R. W. Wilson, "A Measurement of excess antenna temperature at 4080-Mc/s," *Astrophys. J.*, vol. 142, pp. 419–421, 1965.

[8] R. H. Dicke, P. J. E. Peebles, P. G. Roll, and D. T. Wilkinson, "Cosmic Black-Body Radiation," *Astrophys. J.*, vol. 142, pp. 414–419, 1965.

[9] D. J. Fixsen, E. S. Cheng, J. M. Gales, J. C. Mather, R. A. ShaFer, and E. L. Wright, "The cosmic microwave background spectrum from the full cobe firas data set," *The Astrophysical Journal*, vol. 473, no. 2, p. 576, 1996.

[10] Y. Akrami *et al.*, "Planck 2018 results. I. Overview and the cosmological legacy of Planck," 2018.

[11] R. K. Sachs and A. M. Wolfe, "Perturbations of a cosmological model and angular variations of the microwave background," *Astrophys. J.*, vol. 147, pp. 73–90, 1967. [Gen. Rel. Grav.39,1929(2007)].

[12] J. Dunkley, E. Komatsu, M. R. Nolta, D. N. Spergel, D. Larson, G. Hinshaw, L. Page, C. L. Bennett, B. Gold, N. Jarosik, J. L. Weiland, M. Halpern, R. S. Hill, A. Kogut, M. Limon, S. S. Meyer, G. S. Tucker, E. Wollack, and E. L. Wright, "Five-year wilkinson microwave anisotropy probe observations: Likelihoods and parameters from the wmap data," *The Astrophysical Journal Supplement Series*, vol. 180, no. 2, p. 306, 2009.

[13] M. R. Nolta, J. Dunkley, R. S. Hill, G. Hinshaw, E. Komatsu, D. Larson, L. Page, D. N. Spergel, C. L. Bennett, B. Gold, N. Jarosik, N. Odegard, J. L. Weiland, E. Wollack, M. Halpern, A. Kogut, M. Limon, S. S. Meyer, G. S. Tucker, and E. L. Wright, "Five-year wilkinson microwave anisotropy probe observations: Angular power spectra," *The Astrophysical Journal Supplement Series*, vol. 180, no. 2, p. 296, 2009.

[14] G. Steigman, "Primordial Nucleosynthesis in the Precision Cosmology Era," *Ann. Rev. Nucl. Part. Sci.*, vol. 57, pp. 463–491, 2007.

[15] W. Tucker, H. Tananbaum, and R. A. Remillard, "A search for "failed clusters" of galaxies," vol. 444, pp. 532–547, 05 1995.

[16] D. Clowe, M. Brada, A. H. Gonzalez, M. Markevitch, S. W. Randall, C. Jones, and D. Zaritsky, "A direct empirical proof of the existence of dark matter," *The Astrophysical Journal Letters*, vol. 648, no. 2, p. L109, 2006.

[17] J. O. Bennett, D. M. O., N. Schneider, and M. Voit, eds., *The Essential Cosmic Perspective*, pp. 1–608. Pearson Higher Ed USA, 03/01/2017.

[18] E. Corbelli and P. Salucci, "The Extended Rotation Curve and the Dark Matter Halo of M33," *Mon. Not. Roy. Astron. Soc.*, vol. 311, pp. 441–447, 2000.

[19] C. A. Baker *et al.*, "An Improved experimental limit on the electric dipole moment of the neutron," *Phys. Rev. Lett.*, vol. 97, p. 131801, 2006.

[20] R. Peccei and H. Quinn, "CP conservation in the presence of pseudoparticles," vol. 38, pp. 1440–1443, 06 1977.

[21] A. Ringwald, "Axions and Axion-Like Particles," in *Proceedings, 49th Rencontres de Moriond on Electroweak Interactions and Unified Theories: La Thuile, Italy, March 15-22, 2014*, pp. 223–230, 2014.

[22] J. E. Kim and G. Carosi, "Axions and the Strong CP Problem," *Rev. Mod. Phys.*, vol. 82, pp. 557–602, 2010.

[23] E. Arik *et al.*, "Probing eV-scale axions with CAST," *JCAP*, vol. 0902, p. 008, 2009.

[24] S. J. Asztalos, G. Carosi, C. Hagmann, D. Kinion, K. van Bibber, M. Hotz, L. J. Rosenberg, G. Rybka, J. Hoskins, J. Hwang, P. Sikivie, D. B. Tanner, R. Bradley, and J. Clarke, "Squid-based microwave cavity search for dark-matter axions," *Phys. Rev. Lett.*, vol. 104, p. 041301, Jan 2010.

[25] B. W. Lee and S. Weinberg, "Cosmological lower bound on heavy-neutrino masses," *Phys. Rev. Lett.*, vol. 39, pp. 165–168, Jul 1977.

[26] G. Jungman, M. Kamionkowski, and K. Griest, "Supersymmetric dark matter," *Phys. Rept.*, vol. 267, pp. 195–373, 1996.

[27] K. Petraki and R. R. Volkas, "Review of asymmetric dark matter," *Int. J. Mod. Phys.*, vol. A28, p. 1330028, 2013.

[28] L. Canetti, M. Drewes, and M. Shaposhnikov, "Matter and Antimatter in the Universe," *New J. Phys.*, vol. 14, p. 095012, 2012.

[29] K. M. Zurek, "Asymmetric Dark Matter: Theories, Signatures, and Constraints," *Phys. Rept.*, vol. 537, pp. 91–121, 2014.

[30] J. Abdallah *et al.*, "Simplified Models for Dark Matter and Missing Energy Searches at the LHC," 2014. arXiv:1409.2893.

[31] B. Penning, "The pursuit of dark matter at collidersan overview," *J. Phys.*, vol. G45, no. 6, p. 063001, 2018.

[32] V. Khachatryan *et al.*, "Search for dark matter, extra dimensions, and unparticles in monojet events in protonproton collisions at $\sqrt{s} = 8$ TeV," *Eur. Phys. J.*, vol. C75, no. 5, p. 235, 2015.

[33] J. Goodman, M. Ibe, A. Rajaraman, W. Shepherd, T. M. P. Tait, and H.-B. Yu, "Constraints on Dark Matter from Colliders," *Phys. Rev.*, vol. D82, p. 116010, 2010.

[34] M. Klasen, M. Pohl, and G. Sigl, "Indirect and direct search for dark matter," *Prog. Part. Nucl. Phys.*, vol. 85, pp. 1–32, 2015.

[35] T. Bringmann, X. Huang, A. Ibarra, S. Vogl, and C. Weniger, "Fermi LAT Search for Internal Bremsstrahlung Signatures from Dark Matter Annihilation," *JCAP*, vol. 1207, p. 054, 2012.

[36] K. Frankiewicz, "Searching for Dark Matter Annihilation into Neutrinos with Super-Kamiokande," in *Proceedings, Meeting of the APS Division of Particles and Fields (DPF 2015): Ann Arbor, Michigan, USA, 4-8 Aug 2015*, 2015.

[37] M. G. Aartsen *et al.*, "Search for annihilating dark matter in the Sun with 3 years of IceCube data," *Eur. Phys. J.*, vol. C77, no. 3, p. 146, 2017.

[38] J. D. Lewin and P. F. Smith, "Review of mathematics, numerical factors, and corrections for dark matter experiments based on elastic nuclear recoil," *Astropart. Phys.*, vol. 6, pp. 87–112, 1996.

[39] L. Baudis, G. Kessler, P. Klos, R. F. Lang, J. Menndez, S. Reichard, and A. Schwenk, "Signatures of Dark Matter Scattering Inelastically Off Nuclei," *Phys. Rev.*, vol. D88, no. 11, p. 115014, 2013.

[40] G. Bertone, D. Hooper, and J. Silk, "Particle dark matter: Evidence, candidates and constraints," *Phys. Rept.*, vol. 405, pp. 279–390, 2005.

[41] R. H. Helm, "Inelastic and Elastic Scattering of 187-MeV Electrons from Selected Even-Even Nuclei," *Phys. Rev.*, vol. 104, pp. 1466–1475, 1956.

[42] F. Donato, N. Fornengo, and S. Scopel, "Effects of galactic dark halo rotation on WIMP direct detection," *Astropart. Phys.*, vol. 9, pp. 247–260, 1998.

[43] M. C. Smith *et al.*, "The RAVE Survey: Constraining the Local Galactic Escape Speed," *Mon. Not. Roy. Astron. Soc.*, vol. 379, pp. 755–772, 2007.

[44] D. Lynden-Bell, "Statistical mechanics of violent relaxation in stellar systems," *Monthly Notices of the Royal Astronomical Society*, vol. 136, no. 1, pp. 101–121, 1967.

[45] T. Marrodn Undagoitia and L. Rauch, "Dark matter direct-detection experiments," *J. Phys.*, vol. G43, no. 1, p. 013001, 2016.

[46] K. Abe *et al.*, "A direct dark matter search in XMASS-I," 2018.

[47] E. Aprile *et al.*, "First Dark Matter Search Results from the XENON1T Experiment," *Phys. Rev. Lett.*, vol. 119, no. 18, p. 181301, 2017.

[48] P. Agnes *et al.*, "DarkSide-50 532-day Dark Matter Search with Low-Radioactivity Argon," 2018.

[49] E. Aprile *et al.*, "The XENON1T Dark Matter Experiment," *Eur. Phys. J.*, vol. C77, no. 12, p. 881, 2017.

[50] E. Armengaud *et al.*, "Performance of the EDELWEISS-III experiment for direct dark matter searches," *JINST*, vol. 12, no. 08, p. P08010, 2017.

[51] V. Sanglard, "The EDELWEISS experiment and dark matter direct detection," 2003.

[52] R. Bernabei *et al.*, "DAMA/LIBRA results and perspectives," *Bled Workshops Phys.*, vol. 17, no. 2, pp. 1–7, 2016. [EPJ Web Conf.136,05001(2017)].

[53] J. R. T. de Mello Neto *et al.*, "The DAMIC dark matter experiment," *PoS*, vol. ICRC2015, p. 1221, 2016.

[54] Q. Arnaud, A. Brossard, A. Dastgheibi-Fard, G. Gerbier, I. Giomataris, I. Katsioulas, P. Knights, K. Nikolopoulos, I. Savvidis, and N.-G. collaboration (news-g.org [http://news-g.org]), "Spherical proportional counter: A review of recent developments," *Journal of Physics: Conference Series*, vol. 1029, no. 1, p. 012006, 2018.

[55] Q. Arnaud, D. Asner, J.-P. Bard, A. Brossard, B. Cai, M. Chapellier, M. Clark, E. Corcoran, T. Dandl, A. Dastgheibi-Fard, K. Dering, P. D. Stefano, D. Durnford, G. Gerbier, I. Giomataris, P. Gorel, M. Gros, O. Guillaudin, E. Hoppe, A. Kamaha, I. Katsioulas, D. Kelly, R. Martin, J. McDonald, J.-F. Muraz, J.-P. Mols, X.-F. Navick, T. Papaevangelou, F. Piquemal, S. Roth, D. Santos, I. Savvidis, A. Ulrich, F. V. de Sola Fernandez, and M. Zampaolo, "First results from the NEWS-G direct dark matter search experiment at the LSM," *Astroparticle Physics*, vol. 97, pp. 54 – 62, 2018.

[56] R. Strauss, G. Angloher, A. Bento, C. Bucci, L. Canonica, A. Erb, F. von Feilitzsch, N. Ferreiro, P. Gorla, A. Gütlein, D. Hauff, J. Jochum, M. Kiefer, H. Kluck, H. Kraus, J.-C. Lanfranchi, J. Loebell, A. Münster, F. Petricca, W. Potzel, F. Pröbst, F. Reindl, S. Roth, K. Rottler, C. Sailer, K. Schäffner, J. Schieck, S. Scholl, S. Schönert, W. Seidel, M. von Sivers, M. Stanger, L. Stodolsky, C. Strandhagen, A. Tanzke, M. Uffinger, A. Ulrich, I. Usherov, S. Wawoczny, M. Willers, M. Wüstrich, and A. Zöller, "A detector module with highly efficient surface-alpha event rejection operated in CRESST-II Phase 2," *The European Physical Journal C*, vol. 75, p. 352, Jul 2015.

[57] R. Strauss *et al.*, "Beta/gamma and alpha backgrounds in CRESST-II Phase 2," *JCAP*, vol. 1506, no. 06, p. 030, 2015.

[58] G. Angloher *et al.*, "Results on light dark matter particles with a low-threshold CRESST-II detector," *Eur. Phys. J.*, vol. C76, no. 1, p. 25, 2016.

[59] G. Angloher *et al.*, "Results on low mass WIMPs using an upgraded CRESST-II detector," *Eur. Phys. J.*, vol. C74, no. 12, p. 3184, 2014.

[60] A. Brown, S. Henry, H. Kraus, and C. McCabe, "Extending the CRESST-II commissioning run limits to lower masses," *Phys. Rev.*, vol. D85, p. 021301, 2012.

[61] G. Angloher, M. Bauer, I. Bavykina, A. Bento, C. Bucci, C. Ciemniak, G. Deuter, F. von Feilitzsch, D. Hauff, P. Huff, C. Isaila, J. Jochum, M. Kiefer, M. Kimmerle, J.-C. Lanfranchi, F. Petricca, S. Pfister, W. Potzel, F. Pröbst, F. Reindl, S. Roth, K. Rottler, C. Sailer, K. Schäffner, J. Schmaler, S. Scholl, W. Seidel, M. v. Sivers, L. Stodolsky, C. Strandhagen, R. Strauß, A. Tanzke, I. Usherov, S. Wawoczny, M. Willers, and A. Zöller, "Results from 730 kg days of the CRESST-II Dark Matter search," *The European Physical Journal C*, vol. 72, p. 1971, Apr 2012.

[62] R. Agnese *et al.*, "Silicon Detector Dark Matter Results from the Final Exposure of CDMS II," *Phys. Rev. Lett.*, vol. 111, no. 25, p. 251301, 2013.

[63] C. E. Aalseth *et al.*, "CoGeNT: A Search for Low-Mass Dark Matter using p-type Point Contact Germanium Detectors," *Phys. Rev.*, vol. D88, p. 012002, 2013.

[64] P. Agnes *et al.*, "First Results from the DarkSide-50 Dark Matter Experiment at Laboratori Nazionali del Gran Sasso," *Phys. Lett.*, vol. B743, pp. 456–466, 2015.

[65] D. S. Akerib *et al.*, "First results from the LUX dark matter experiment at the Sanford Underground Research Facility," *Phys. Rev. Lett.*, vol. 112, p. 091303, 2014.

[66] E. Aprile *et al.*, "Dark Matter Results from 225 Live Days of XENON100 Data," *Phys. Rev. Lett.*, vol. 109, p. 181301, 2012.

[67] R. Agnese *et al.*, "New Results from the Search for Low-Mass Weakly Interacting Massive Particles with the CDMS Low Ionization Threshold Experiment," *Phys. Rev. Lett.*, vol. 116, no. 7, p. 071301, 2016.

[68] R. Agnese *et al.*, "Search for Low-Mass Weakly Interacting Massive Particles with SuperCDMS," *Phys. Rev. Lett.*, vol. 112, no. 24, p. 241302, 2014.

[69] E. Armengaud *et al.*, "A search for low-mass WIMPs with EDELWEISS-II heat-and-ionization detectors," *Phys. Rev.*, vol. D86, p. 051701, 2012.

[70] Q. Yue *et al.*, "Limits on light WIMPs from the CDEX-1 experiment with a p-type point-contact germanium detector at the China Jingping Underground Laboratory," *Phys. Rev.*, vol. D90, p. 091701, 2014.

[71] J. Barreto *et al.*, "Direct Search for Low Mass Dark Matter Particles with CCDs," *Phys. Lett.*, vol. B711, pp. 264–269, 2012.

[72] G. Bellini *et al.*, "Cosmic-muon flux and annual modulation in Borexino at 3800 m water-equivalent depth," *JCAP*, vol. 1205, p. 015, 2012.

[73] V. E. Guiseppe, S. R. Elliott, A. Hime, K. Rielage, and S. Westerdale, "A Radon Progeny Deposition Model," *AIP Conf. Proc.*, vol. 1338, pp. 95–100, 2011.

[74] C. Arpesella, "Background measurements at GRAN SASSO laboratory," in *TAUP 91. Proceedings, 2nd International Workshop on Theoretical and Phenomenological Aspects of Underground Physics, Toledo, Spain, September 9-13, 1991*, pp. 0420–424, 1992.

[75] M. Haffke, L. Baudis, T. Bruch, A. Ferella, T. M. Undagoitia, M. Schumann, Y.-F. Te, and A. van der Schaaf, "Background measurements in the gran sasso underground laboratory," *Nuclear Instruments and Methods in Physics Research Section A: Accelerators, Spectrometers, Detectors and Associated Equipment*, vol. 643, no. 1, pp. 36 – 41, 2011.

[76] P. Belli, R. Bernabei, S. D'Angelo, M. P. De Pascale, L. Paoluzi, R. Santonico, N. Taborgna, N. Iucci, and G. Villoresi, "Deep Underground Neutron Flux Measurement With Large Bf-3 Counters," *Nuovo Cim.*, vol. A101, pp. 959–966, 1989.

[77] A. Senyshyn, H. Kraus, V. B. Mikhailik, and V. Yakovyna, "Lattice dynamics and thermal properties of $CaWO_4$," *Phys. Rev. B*, vol. 70, p. 214306, Dec 2004.

[78] R. Viswanathan, "Heat capacity of sapphire between 2 and 10 k by ac technique," *Journal of Applied Physics*, vol. 46, no. 9, pp. 4086–4087, 1975.

[79] O. Madelung, U. Rössler, and M. Schulz, eds., *Silicon (Si), Debye temperature, heat capacity, density, hardness, melting point*, pp. 1–16. Berlin, Heidelberg: Springer Berlin Heidelberg, 2002.

[80] F. Pröbst, M. Frank, S. Cooper, P. Colling, D. Dummer, P. Ferger, G. Forster, A. Nucciotti, W. Seidel, and L. Stodolsky, "Model for cryogenic particle detectors with superconducting phase transition thermometers," *Journal of Low Temperature Physics*, vol. 100, pp. 69–104, Jul 1995.

[81] M. Pyle, E. Feliciano-Figueroa, and B. Sadoulet, "Optimized Designs for Very Low Temperature Massive Calorimeters," 2015.

[82] G. Angloher, P. Bauer, N. Ferreiro, D. Hauff, A. Tanzke, R. Strauss, M. Kiefer, F. Petricia, F. Reindl, W. Seidel, F. Pröbst, and M. Wüstrich, "Quasiparticle diffusion in CRESST Light Detectors," *Journal of Low Temperature Physics*, vol. 184, pp. 323–329, Jul 2016.

[83] I. Bavykina, *Investigation of $ZnWO_4$ and $CaMoO_4$ as target materials for the CRESST-II dark matter search.* PhD thesis, Ludwig-Maximilians-Universität München, 2009.

[84] R. Strauss *et al.*, "Energy-dependent light quenching in $CaWO_4$ crystals at mK temperatures," *Eur. Phys. J.*, vol. C74, no. 7, p. 2957, 2014.

[85] F. Petricca *et al.*, "First results on low-mass dark matter from the CRESST-III experiment," in *15th International Conference on Topics in Astroparticle and Underground Physics (TAUP 2017) Sudbury, Ontario, Canada, July 24-28, 2017*, 2017.

[86] M. Tinkham, *Introduction to superconductivity.* New York: McGraw-Hill, 1975.

[87] F. Reindl, *Exploring Light Dark Matter With CRESST-II Low-Threshold Detectors.* PhD thesis, Technische Universität München, 2016.

[88] P. Bauer, "Analysis of CRESST-III dark matter data." PhD thesis in preparation.

[89] S. Yellin, "Finding an upper limit in the presence of an unknown background," *Phys. Rev. D*, vol. 66, p. 032005, Aug 2002.

[90] INCAA Computers BV, "vd80 transient digitizer." http://www.incaacomputers.com/products/by-function/transient-recorder/vd80/, 2018. [Online; accessed 15-March-2018].

[91] W. H. Press, S. A. Teukolsky, W. T. Vetterling, and B. P. Flannery, "Numerical recipes in c: The art of scientific computing. second edition," 1992.

[92] E. Gatti and P. F. Manfredi, "Processing the Signals From Solid State Detectors in Elementary Particle Physics," *Riv. Nuovo Cim.*, vol. 9N1, pp. 1–146, 1986.

[93] E. Gatti, M. Sampietro, and P. Manfredi, "Optimum filters for detector charge measurements in presence of 1f noise," *Nuclear Instruments and Methods in Physics Research Section A: Accelerators, Spectrometers, Detectors and Associated Equipment*, vol. 287, no. 3, pp. 513 – 520, 1990.

[94] R. F. Lang *et al.*, "Scintillator Non-Proportionality and Gamma Quenching in CaWO4," 2009.

Acknowledgments

During my time as Ph.D. student I had the privilege to work in contact with exceptional scientists. Thank to them I could develop my ideas in a stimulating and rich environment. The realisation of this thesis would not have been possible without their precious support.

I thank Prof. Dr. Otmar Biebel for having me as Ph.D. student and his comments that improved the quality of this manuscript.

I'm grateful to Dr. Franz Pröbst for having accepted me to work in his group at MPI and for the freedom he granted me. His knowledge of every detail of the experiment and vast expertise were very valuable for this work and my time at the Institute.

Thanks to Dr. Federica Petricca, without her constant support during the time of writing this work was not to see the light. Thanks for all the time dedicated to the reading and for your always positive attitude.

To Prof. Antonio Bento I thank the proof-read of this thesis, I know it was quite an effort. Thanks for the numerous, endless discussions about life and science. Whether it was on a ski slope, on the coast in Portugal or just sitting in a pub, I have only good memories.

I thank Dieter Hauff for all the support that I had in the laboratory. Working with you by side was always a reason of relief!

The deployment of the detectors and their operation in Run34 owe much to Dr. Raimund Strauß's energies and enthusiasm, so do I for the experience I gained during the preparation of the Run.

Working with Dr. Michele Mancuso was molto divertente. I'm glad for the time I've got to spend with you in the various labs, you're certainly one of the best cryogenists on the market!

I thank my colleague Philipp Bauer and the efforts he dedicated to make the data produced in this work usable.

Sempre grato a mia nonna, per avermi supportato incondizionatamente.